Controlling Self-assembled Surface Features in Thin Films by Surface Tension and Elasticity

by

Zhouzhou Zhao

A dissertation submitted in partial fulfillment
of the requirements for the degree of
Doctor of Philosophy
(Mechanical Engineering)
in The University of Michigan
2013

Doctoral Committee:

Associate Professor Wei Lu, Chair
Assistant Professor Anastasios John Hart
Assistant Professor Pramod Sangi Reddy
Assistant Professor Anish Tuteja

ACKNOWLEDGEMENTS

First, I would like to express my most sincere appreciation and respect to my advisor, Prof. Wei Lu, who has given me great support, encouragement and guidance throughout the past five years. His outstanding vision and knowledge in multiple disciplines helped me overcome many difficulties and move forward in the right direction. From him, I have learned the dedication to the research and the passion about the job.

I would like to express my special thanks to Prof. John Hart and his group for the fruitful collaborations and the interesting research topics. Prof. John Hart has helped me a great with insightful discussions and valuable inputs to my paper drafts. Many thanks to his students Dr. Sameh Tawfick, Dr. Eric Meshot, and Sei Jin Park for providing the fascinating carbon nanotube experiment results. Without their tremendous assistance, this work would not have been possible.

I am very grateful to Prof. Anish Tuteja and Prof. Pramod Reddy for being in my dissertation committee, giving advice and support.

I also would like to thanks my colleagues Dr. Jonghyun Park, Dr. Seungjun Lee and Haicheng Guo for the countless discussions and helps in my study and life.

Last but most importantly, I would like to thank my parents, and my fiancée, Cheng Zhu, for their years of unconditional support.

TABLE OF CONTENTS

LIST OF FIGURES

ABSTRACT

Self-assembled micro and nanostructures in thin films have many potential applications in microelectronics, photonics, coatings and solar cells. Precise control over the self-assembled surface features, such as pattern, order and feature size, is crucial to the device performance. However, most current self-assembly methods have inadequate control over defects. Motivated by this challenge, this work aims to investigate and propose mechanisms for efficient and robust fabrication of well-defined micro and nanostructures by self-assembly. Specifically, the coupling of surface tension and elasticity is the focus of this work.

First, I proposed two mechanisms to improve the long-range order in self-assembled nanostructures in a continuum binary thin film. The first mechanism is called sequential activation of self-assembly, in which the self-assembly was initiated in a small mobile region to form a seed pattern, and then the mobile region was shifted gradually. This process led to a long-rang ordered superlattice regardless of whether the seed was perfect or not. Further exploration led to the second mechanism which we call the spontaneous propagation of self-assembly. This mechanism utilizes the ordered pattern in the growth front to trigger self-assembly in the propagation front zone. It enables the delivery of local order information to distance by spontaneous propagation. Both mechanisms may apply to other self-assembled systems.

Next, I studied the formation of self-assembled nanoparticles during dewetting of templated thin films. Recent experiments showed that anodic aluminum oxide (AAO) membranes, which have uniform nanoscale pore size and spacing, can influence the dewetting of iron thin films into organized arrays of nanoparticles, such as for growth of ordered carbon nanotubes (CNTs). Our simulations captured the dynamic dewetting processes from early expansion of pores, rupture of liquid network to final formation of discrete nanoparticles. It is shown that the AAO pore position variations and the initial film thicknesses have strong influence on the order of nanoparticles, while AAO pore size variations have relatively weak effect on the order. Two coarsening mechanisms are further identified to explain the changes in particle order parameter and size distribution.

Last, I investigated the mechanisms of elastocapillary densification of pre-patterned vertically aligned CNT forests. Recent experiments showed controllable bent, twisted, re-entrant and other complex 3D microstructures can be fabricated via this capillary forming method. The bending mechanism in bilaterally symmetric structures is revealed by considering competition between axial forces and lateral forces. The shape change in cross-section of relatively short CNT forests is explained as a substrate effect. In addition, the nonlinear lateral mechanical behavior of CNT forests is captured by finite element modeling of a contact problem between a pair of curved beams.

Chapter 1

Introduction and outline

1.1 Introduction

1.1.1 Self-assembly: from nature to nanoscience

Nature has been a blueprint for human discoveries and innovations throughout the history. Birds conquer the sky long before the Wright Brothers, dolphins have their own long-range sonar under the water, and the plant burrs surface feature inspires the design of Velcro hook-and-loop fasteners. These inventions and mechanisms inspired by nature are used in our daily life and familiar to us. However, there is one salient characteristic in nature that people sometimes may overlook, which is the extreme high-degree of order existed in natural materials or organisms. For example, water molecules can form regular hexagonal shaped snowflakes when condensed under certain temperatures [1] (see Figure

1.1), clouds can form distinctive patterns at different altitudes [2], leaves can take thousands of regular shapes based on the species of the plants, and the most amazingly, about 10-100 billion neural cells organize in a way that forms an adult human brain [3]. More strikingly, one may notice that the constituents of these highly ordered entities consist of completely random and disordered atoms, molecules or cells. In fact, processes in which systems spontaneously develop from disordered to ordered states are ubiquitous in nature. To emphasize the spontaneity of these processes which occurs without human intervention, we usually call them self-assembly or self-organization phenomenon (I will use self-assembly in this thesis; please refer to [4] for subtle differences between the two). Indeed the physics underlying the self-assembly processes have been intriguing researchers for long and have attracted increasing attentions especially in the recent decade with the emergence of nanoscience[5].

Why nano-scientists chose self-assembly? First, the limit of traditional photolithographic method has created opportunities for novel approaches to further miniaturizing microelectronic components to sub 10nm level [6]. Self-assembly is considered as one of the most efficient and preferred methods in this innovation. Second, self-assembly creates a new pathway to synthesize novel materials with nano-scale building blocks other than atoms. These self-assembled materials possess unique properties compared to traditional crystalline materials [7]. Third, self-assembly is a parallel process in essence, unlike some serial techniques such as optical tweezers[8] or atomic traps [9]. Therefore the bulk nanofabrication based on self-assembly will have relative low cost and high throughput over other approaches.

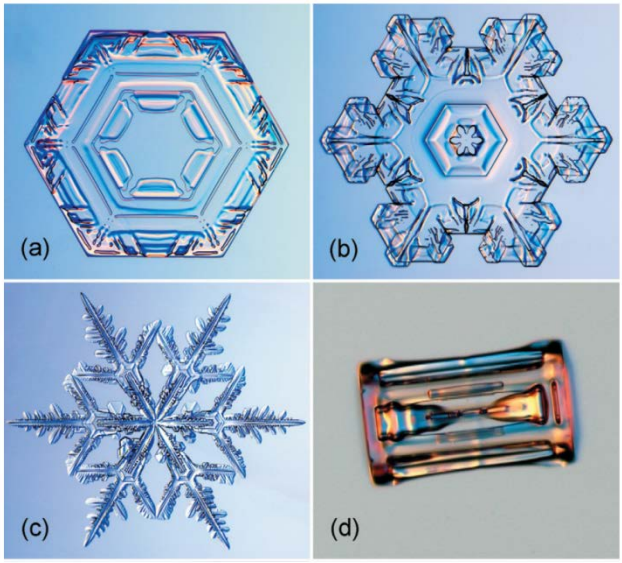

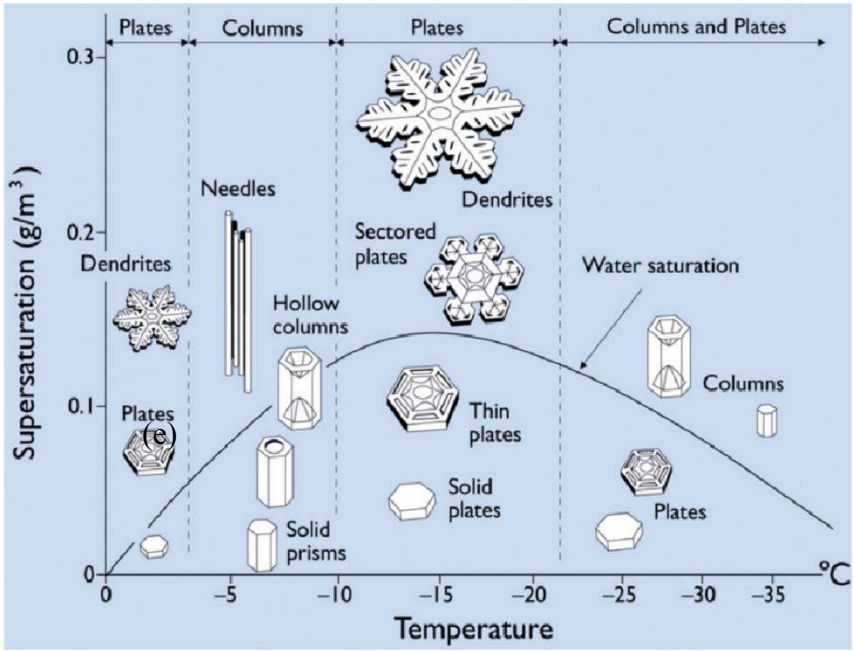

Figure 1.1 (a)-(d) Snowflakes morphologies (e) the morphology phase diagram of snowflakes in terms of temperature and supersaturation [1]

The ability to design and apply self-assembly into nanofabrication requires full understanding of the mechanism how self-assembly works in a system. Self-assembly is a spontaneous physical or chemical process, therefore the associated free energy change

during the process must be negative according to thermodynamics. Considering a system at a constant temperature and pressure, the associated Gibbs free energy G has the mathematical definition as following, $G = H - TS$, where H and S stands for enthalpy and entropy respectively. The change of free energy gives $\Delta G = \Delta H - T\Delta S$. When the change of entropy $\Delta S < 0$ during the self-assembly, it increases the Gibbs free energy which means the process must be enthalpy-driven so that $\Delta H < T\Delta S$. When $\Delta S > 0$, entropy itself favors the self-assembly to occur. In this case the change of enthalpy can be negative or positive as long as $\Delta H < T\Delta S$. Note that although self-assembly is a spontaneous process that transform the system from disorder into order, it does not indicate that the always decreases. The actual change depends on the real system [10-12]. Similar arguments also apply when we consider Helmholtz free energy.

Building blocks and the interactions between them are the two essential elements of self-assembly. Just as its name implies, the building blocks such as nanoparticles and nanotubes serves as the bricks; the interactions such as van der Waal force, electrostatic force and magnetic force, being attractive or repulsive, serve as the cement. After over two decades of intense research on nano-materials, the focus of self-assembly is shifting from synthesis of individual building blocks to their larger scale assembly of micro-, nanostructures. Hundreds and thousands of well-defined nano-components have been synthesized in terms of sizes, shapes and materials [10]. However, as the other important element of self-assembly, the interactions between nano-components are yet well controlled. Most self-assembly processes are still suffering from the defects and inadequate control of repeatability. At nanoscale, the properties of the self-assembled materials highly depend on the size of building blocks, the spacing and the order of the

lattice or structure, which are crucial to any application targeted nano-fabrications. Therefore, the challenge that is facing nano-fabrications nowadays is to develop efficient and robust ways of assembling the existing nano-components into well-defined micro and nanostructures. Motivated by the challenge, this work aims to investigate and propose the potential mechanisms to achieve better defect control over the self-assembly process and thus improve the quality of self-assembled micro and nanostructures in thin films.

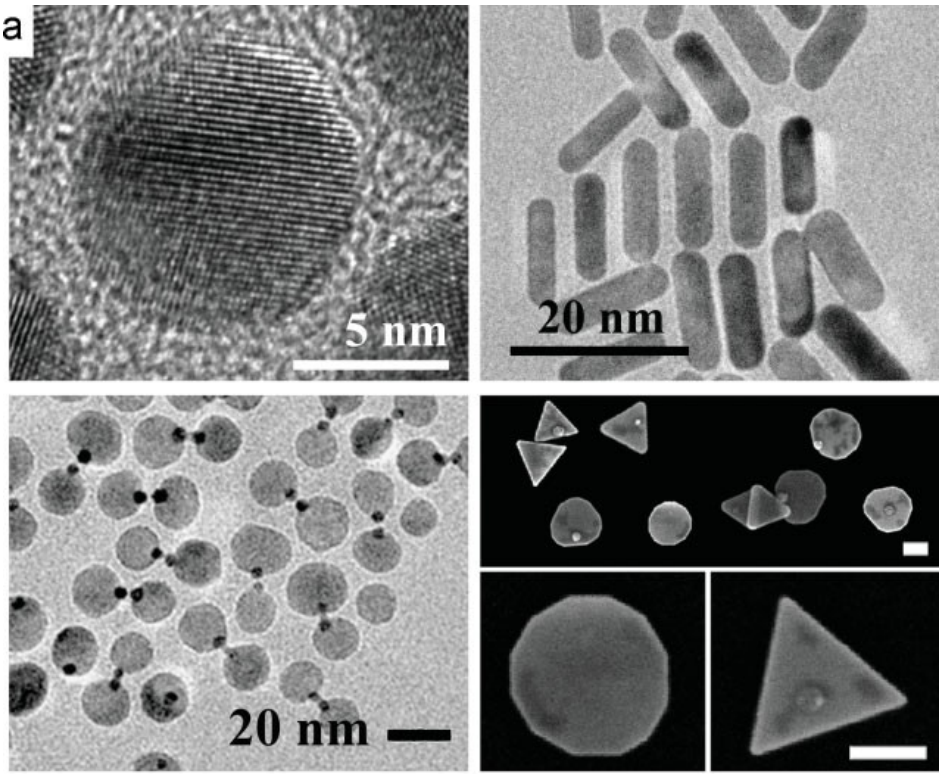

Figure 1.2 Nanoscale building blocks with different shapes [10]

1.1.2 Self-assembled nanostructures in thin film self-assembly

Self-assembly usually occurs in a liquid phase or on a solid substrate due to the mobility requirement on the building blocks. In a liquid phase, the building blocks are governed by Brownian motion and corresponding long-range interactions such as van de Waal interaction, electrostatic [13, 14], magnetic interactions [15, 16]. They usually form crystal-like superlattices [17-19]. This thesis will focus on the case which self-assemblies occur on a solid substrate. In this situation, due to the size of the nanoscale building blocks, the initial or the final configurations of the systems are often in the form of thin films.

A thin film is a layer of materials with thickness much less than the extent of the film. In nanoscience, the subjects of interest range from monolayers (one layer of molecules or atoms) to films with thickness of a few micrometers. Thin films have been widely used in semiconductor devices [20], material coatings [21], batteries [22], solar cells [23] and etc. Their uniformity in thickness and compositions is of great importance to the device performance. The traditional thin film preparation methods include chemical deposition[24] and physical deposition[25]. In the context of self-assembly, thin films are usually used in two situations. (1) The films are in liquid phase and act as the environment of discrete building blocks such as molecules, cells, nanoparticles and nanotubes. These building blocks are usually suspending or floating in the thin films. Under the actions of surface tension and associated interactions, the building blocks aggregate with [26-28] or without the evaporation of the liquid phase [29]. Assemblies of these building blocks with certain ordered arrangement become the functional materials of our interest while the liquid phase can be often removed. (2) In the other case, the

films are in liquid or solid phases and there are no explicit building blocks initially; the building blocks form simultaneously from phase separation or composition modulation during self-assembly [30]. Therefore, the systems often consist of mixtures of different species or phases. For examples, diblock copolymers thin film forms hexagonal or striped patterns when heated above its glass transition temperature [31, 32]. Binary monolayers can form ordered hexagonal patterns on a solid substrate [33]. In these systems, the outcome of the self-assembly is the newly developed building blocks which are made out of the thin film itself.

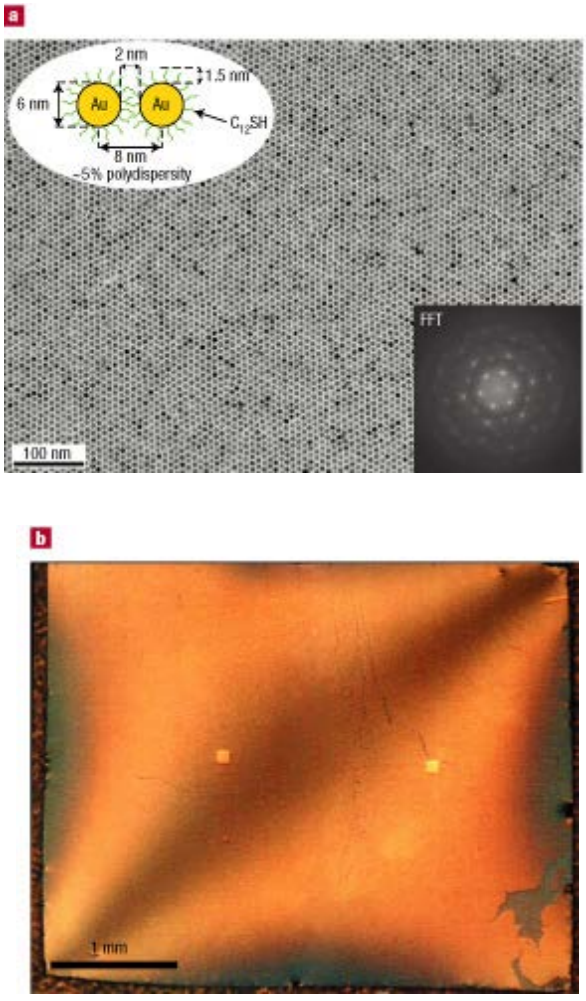

Figure 1.3 Self-assembled gold monolayer produced by drop-casting a liquid film onto a solid substrate. [28]

1.1.3 Role of surface tension and elasticity in thin film self-assembly

From energy perspective, the change of free energy determines the driving forces of the self-assembly. For a typical thin film self-assembly system, the dominant free energy components often come from surface tension, interactions among building blocks and interactions with substrates.

Surface tension is caused by the energy state imbalance between the molecules on the surface and those inside the body. It has a unit of force per unit length or we sometimes use surface energy in unit of energy per unit area according to the emphasis. When the length scale decreases to micro- or nano-domain, the surface tension becomes overwhelming. It is because gravitational force scales with dimension cubed, while surface tension only scales linearly with dimension. We usually use the capillary length $\kappa^{-1} = \sqrt{\gamma / \rho g}$ to determine whether gravity is important in the system or not, where γ is the surface tension, ρ is the density of the liquid and g is the gravitational acceleration. When the size of interested system is less than κ^{-1}, the gravity is negligible and vice versa. The typical order of the capillary length is about a few millimeters for water. This length renders the surface tension an excellent candidate for driving force of mico and nano-scale self-assembly [34].

Surface tension always tends to minimize the surface area. This tendency plays slightly different roles in different thin film self-assembly systems. For example, in a system with nanoparticles or molecules floating on the liquid-air interface, surface tension provides an attractive interaction between these building blocks. In a system without pre-fabricated building blocks such as those in type (2) discussed earlier, surface

tension tends to stabilize any fluctuations on the thin film surface. The details will be discussed later in the following chapters via different systems.

On the other hand, the interactions among building blocks and the interactions between films and substrates usually provide certain competing actions to the surface tension. For example, there will be electrostatic repulsion [35] if particles are charged. Van de Waal interaction could cause the disjoining pressure [36] between two interfaces that are less than 100nm apart. This thesis will focus on those interactions that arise from elasticity. This includes both elastic interaction with the substrate and elasticity of the building block itself. For example, quantum dots formation by Stranski–Krastanov growth [37] is induced by excess strain energy. The self-assembled binary monolayer on a solid substrate [30] is driven by the competition between elastic energy due to lattice misfit and interfacial energy. Buckling of thin film on compliant substrate is caused by the modulus difference [38]. The elastocapillary densification of CNT forests [39] is driven by capillary forces. Due to elasticity of wavy CNTs, the process may terminate before reaching the ideal close-packed state. As a traditional theory, elasticity coupled with surface tension opens up many new topics in the nanoscience era.

1.2 Thesis outline

The thesis is organized into chapters as follows:

Chapter 2 presents two mechanisms to improve the long-range order in self-assembled nanostructures in a continuum binary monolayer. Previous experiments showed that self-assembled domains with different orientations may induce many defects. We first proposed a mechanism called sequential activation of self-assembly. Further exploration led to an intriguing finding which we call the spontaneous propagation of self-assembly.

Chapter 3 investigates the formations of self-assembled nanoparticles during dewetting of pre-patterned thin films. Our simulations captured the dynamic dewetting processes from pore expanding, rupture of liquid networks to formation of discrete nanoparticles. The effects of initial pore position variations, size variations and film thicknesses were studied.

Chapter 4 investigates the mechanisms of elastocapillary densification of pre-patterned vertically aligned carbon nanotube (CNT) thin films. First, an analytical model was developed to predict the bending angles by considering two competing actions. Next, a mechanism was proposed to explain the shape change of cross-section of CNT microstructures. At last, a finite element model was developed to capture the nonlinear lateral mechanical behavior of CNT forests.

Chapter 5 summarizes the contributions of this thesis and provides an outlook for future work.

1.3 References

1. Kenneth, G.L., *The physics of snow crystals.* Reports on Progress in Physics, 2005. **68**(4): p. 855.

2. Peter, T., et al., *Ultrathin Tropical Tropopause Clouds (UTTCs): I. Cloud morphology and occurrence.* Atmos. Chem. Phys., 2003. **3**(4): p. 1083-1091.

3. Drachman, D.A., *Do we have brain to spare?* Neurology, 2005. **64**(12): p. 2004-2005.

4. Bensaude-Vincent, B., *Self-Assembly, Self-Organization - A Philosophical Perspective on Converging Technologies.* 2006: p. 1-23.

5. Whitesides, G.M. and B. Grzybowski, *Self-Assembly at All Scales.* Science, 2002. **295**(5564): p. 2418-2421.

6. Harriott, L.R., *Limits of lithography.* Proceedings of the IEEE, 2001. **89**(3): p. 366-374.

7. Alivisatos, A.P., *Semiconductor Clusters, Nanocrystals, and Quantum Dots.* Science, 1996. **271**(5251): p. 933-937.

8. Curtis, J.E., B.A. Koss, and D.G. Grier, *Dynamic holographic optical tweezers.* Optics Communications, 2002. **207**(1–6): p. 169-175.

9. Letokhov, V.S., *Electromagnetic trapping of cold atoms: An overview*. Trapped Particles and Fundamental Physics, ed. S.N. Atutov, R. Calabrese, and L. Moi. Vol. 51. 2002, Dordrecht: Springer. 11-38.

10. Bishop, K.J.M., et al., *Nanoscale Forces and Their Uses in Self-Assembly.* Small, 2009. **5**(14): p. 1600-1630.

11. Barry, E. and Z. Dogic, *Entropy driven self-assembly of nonamphiphilic colloidal membranes.* Proceedings of the National Academy of Sciences, 2010. **107**(23): p. 10348-10353.

12. Nakamura, I. and A.-C. Shi, *Study of entropy-driven self-assembly of rigid macromolecules.* Physical Review E, 2009. **80**(2): p. 021112.

13. Park, J. and W. Lu, *Self-assembly of functionally gradient nanoparticle structures.* Applied Physics Letters, 2008. **93**(24): p. 243109.

14. Kalsin, A.M., et al., *Electrostatic Self-Assembly of Binary Nanoparticle Crystals with a Diamond-Like Lattice.* Science, 2006. **312**(5772): p. 420-424.

15. Kim, B.Y., et al., *Magnetic self-assembly of gold nanoparticle chains using dipolar core-shell colloids.* Chemical Communications, 2011. **47**(3): p. 890-892.

16. Chen, J., et al., *Collective Dipolar Interactions in Self-Assembled Magnetic Binary Nanocrystal Superlattice Membranes.* Nano Letters, 2010. **10**(12): p. 5103-5108.

17. Ghadimi, A., et al., *Plasma within Templates: Molding Flexible Nanocrystal Solids into Multifunctional Architectures.* Nano Letters, 2007. **7**(12): p. 3864-3868.

18. Urban, J.J., et al., *Synergism in binary nanocrystal superlattices leads to enhanced p-type conductivity in self-assembled PbTe/Ag2Te thin films.* Nat Mater, 2007. **6**(2): p. 115-121.

19. Shevchenko, E.V., et al., *Structural diversity in binary nanoparticle superlattices.* Nature, 2006. **439**(7072): p. 55-59.

20. Garnier, F., et al., *An all-organic "soft" thin film transistor with very high carrier mobility.* Advanced Materials, 1990. **2**(12): p. 592-594.

21. Lee, L.L., C.D. Schaper, and W.K. Ho, *Real-time predictive control of photoresist film thickness uniformity.* Ieee Transactions on Semiconductor Manufacturing, 2002. **15**(1): p. 51-59.

22. Dudney, N.J., *Solid-state thin-film rechargeable batteries.* Materials Science and Engineering: B, 2005. **116**(3): p. 245-249.

23. Aberle, A.G., *Thin-film solar cells.* Thin Solid Films, 2009. **517**(17): p. 4706-4710.

24. Minegishi, K., et al., *Growth of p-type zinc oxide films by chemical vapor deposition.* Japanese Journal of Applied Physics Part 2-Letters, 1997. **36**(11A): p. L1453-L1455.

25. Helmersson, U., et al., *Ionized physical vapor deposition (IPVD): A review of technology and applications.* Thin Solid Films, 2006. **513**(1-2): p. 1-24.

26. Brinker, C.J., et al., *Evaporation-Induced Self-Assembly: Nanostructures Made Easy.* Advanced Materials, 1999. **11**(7): p. 579-585.

27. Shastry, T.A., et al., *Large-Area, Electronically Monodisperse, Aligned Single-Walled Carbon Nanotube Thin Films Fabricated by Evaporation-Driven Self-Assembly.* Small, 2012: p. n/a-n/a.

28. Bigioni, T.P., et al., *Kinetically driven self assembly of highly ordered nanoparticle monolayers.* Nat Mater, 2006. **5**(4): p. 265-270.

29. Zhang, S., et al., *Ordering in a Droplet of an Aqueous Suspension of Single-Wall Carbon Nanotubes on a Solid Substrate.* Langmuir, 2009. **26**(3): p. 2107-2112.

30. Plass, R., et al., *Nanostructures - Self-assembled Domain Patterns.* Nature, 2001. **412**(6850): p. 875-875.

31. Fasolka, M.J. and A.M. Mayes, *Block Copolymer Thin Films: Physics and Applications.* Annual Review of Materials Research, 2001. **31**: p. 323-355.

32. Hawker, C.J. and T.P. Russell, *Block Copolymer Lithography: Merging "Bottom-Up" with "Top-Down" Processes.* MRS Bull., 2005. **30**(12): p. 952-966.

33. Suo, Z. and W. Lu, *Composition Modulation and Nanophase Separation in a Binary Epilayer.* Journal of the Mechanics and Physics of Solids, 2000. **48**(2): p. 211-232.

34. Syms, R.R.A., et al., *Surface tension-powered self-assembly of microstructures - the state-of-the-art.* Microelectromechanical Systems, Journal of, 2003. **12**(4): p. 387-417.

35. Tomba, G., et al., *Supramolecular Self-Assembly Driven by Electrostatic Repulsion: The 1D Aggregation of Rubrene Pentagons on Au(111).* ACS Nano, 2010. **4**(12): p. 7545-7551.

36. Kim, H.I., et al., *How Disjoining Pressure Drives the Dewetting of a Polymer Film on a Silicon Surface.* Physical Review Letters, 1999. **82**(17): p. 3496-3499.

37. Ledentsov, N.N., et al., *Direct formation of vertically coupled quantum dots in Stranski-Krastanow growth.* Physical Review B, 1996. **54**(12): p. 8743-8750.

38. Jiang, H., et al., *Finite deformation mechanics in buckled thin films on compliant supports.* Proceedings of the National Academy of Sciences, 2007. **104**(40): p. 15607-15612.

39. De Volder, M., et al., *Diverse 3D Microarchitectures Made by Capillary Forming of Carbon Nanotubes.* Advanced Materials, 2010. **22**(39): p. 4384-4389.

Chapter 2

Growing long-range ordered superlattice from a continuum medium by sequential activation and spontaneous propagation of self-assembly

2.1 Motivation

The self-assembly of nanostructures enables a wide range of applications from nanoelectronic devices [1], ultrasensitive biosensors [2], carriers for drug delivery [3], to advanced materials with unique mechanical [4], electrical [5] or photonic [6] properties.

The lack of long-range order has been a major challenge for self-assembled nanostructures since high regularity is crucial to many applications [7, 8]. Various

defects are known as the killer of the long-range order, including grain boundaries, triple junctions and dislocations. In order to keep the defects in minimum, the integration of self-assembly with the traditional "top-down" approach has been exploited to improve the long-range order. This approach uses templates to help a self-assembly process by modulating the energy profile. For instance, geometric templates have been used to guide the self-assembly of block copolymers [9], quantum dots [10, 11], and nanocrystals [12]. The templating approach typically requires lithography to fabricate a pre-patterned substrate or mask as a template. The wavelength of the template has to be small enough to provide effective guidance and the overall pattern is limited by the size of the template. People have yet to find a general and intrinsic approach to effectively control the appearance of defects in the formed structures. Motivated by these limitations, we proposed two potential template-free approaches to grow self-assembled superlattices over a large area.

2.2 Self-assembly in a continuum medium

Depending on the type of building blocks, self-assembled systems can be classified into two categories: discrete and continuum. A discrete system uses pre-fabricated building blocks with fixed sizes and shapes. Examples include the self-assembly of nanoparticles [5, 13, 14], nanorods [15, 16] and nanoplates [17, 18]. In contrast, a continuum system exploits the spontaneous formation of nanoscale domains. Examples include self-assembled domain patterns in binary monolayers [19], block copolymers [20] and organic molecular adsorbates on metal surfaces [21]. A continuum system offers several unique features. For instance, domains and their patterns self-assemble simultaneously, so that there is no need to pre-synthesize the building blocks; a significant degree of process flexibility and control can be achieved; and the approach may be applied to diverse systems.

Epitaxial monolayers on solid substrates can form various two dimensional pattern. For example, Pohl et al. observed that when a monolayer of Ag and S mixture is deposited on a Ru surface, a hexagonal patterned superlattice is formed with featured domain size about 3 nm [22]. Plass et al. reported several self-assembled domain patterns at different concentration fractions for Pb/Cu monolayer system [19] (Figure 2.1). Umezawa et al. showed that arrays of triangular domains when a Ag monolayer of ractional coverage 0.8 is deposited on Cu substrate [23].

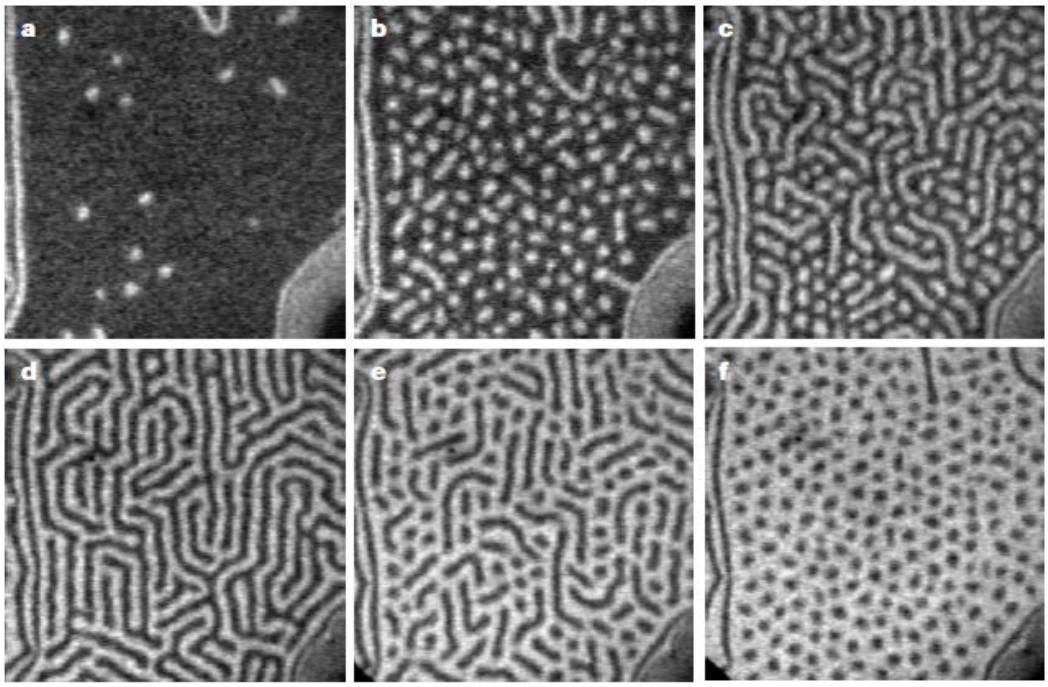

Figure 2.1 Self-assembled domain patterns formed at different concentration fractions on Pb/Cu monolayers. [19]

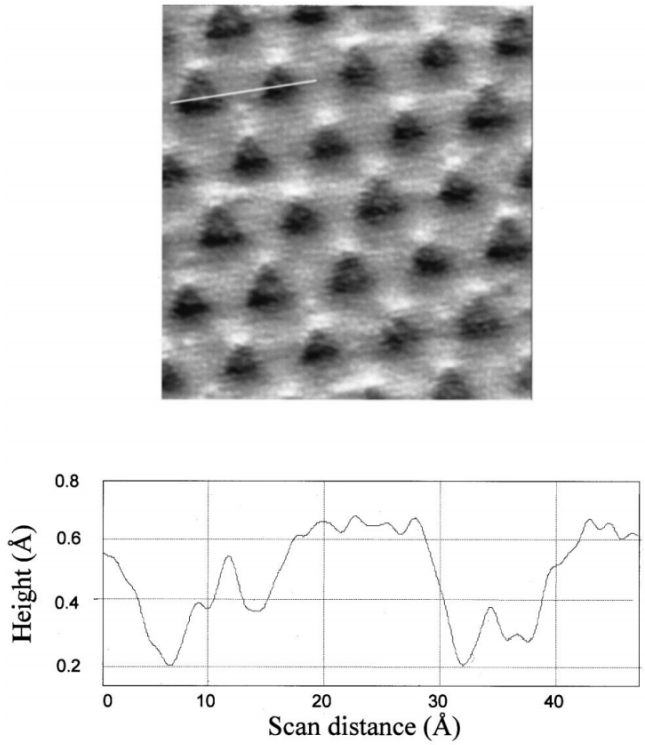

Figure 2.2 STM image after deposition of 0.8 monolayer of Ag on the Cu substrate revealing a network of triangles. [23]

2.3 Phase field model

A wide variety of continuum self-assembled systems demonstrate similar domain patterns, suggesting a possible universal framework to capture the essential mechanism. Here we use a phase field model to describe the formation of these patterns [24]. To explain this idea, we consider a two dimensional epilayer of two atomic species A and B (Figure 2.3), which occupies the $x_1 - x_2$ plane and forms a coherent lattice with the substrate. Experiments have shown that the composition often modulates in the plane of the layer, and the layer may separate into two phases, forming periodic dots or other regular domain patterns [19, 25]. The domain size may be in the range of 1-100nm, and stable against coarsening. Define C as the concentration fraction of B, where C=0 represents pure A, and C=1 represents pure B. The phase separation leads to A-rich and B-rich domains. The pattern is expressed by a spatial function $C(x_1, x_2)$, or $C(\mathbf{x})$. The free energy of the system is determined by the short-range atomic/molecular interaction and the long-range interaction between domains [26], which is given by

$$G = \int_A g(C)dA + h\int_A |\nabla C|^2 \, dA - \frac{1}{2}\int_A \left(\sigma_{31}u_1 + \sigma_{32}u_2\right) dA \qquad (2.1)$$

The first term represents the chemical energy of the epilayer per unit area, which drives phase separation. The second term represents the phase boundary energy, where h is a positive material constant. This term prefers a larger domain size. The third term captures the long-range interaction, which prefers a smaller domain size. These two competing actions lead to the formation of a periodic pattern of alternating A-rich and B-rich domains, and the domain size is determined by their relative strength. Here σ_{31}, σ_{32} are

the traction forces per unit area on the substrate, and u_1, u_2 are the corresponding displacements. The integration extends over the epilayer.

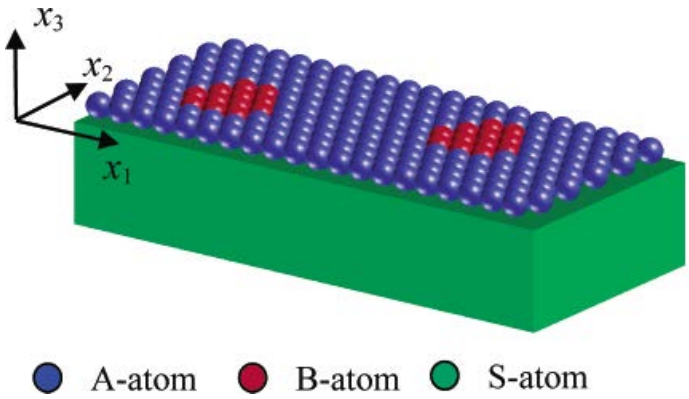

Figure 2.3 Schematic of self-organized nanoscale patterns on a substrate surface. [27]

The form of the long-range interaction in Eq (2.1) is representative. The elastic interaction is dipole type, where the energy has $1/r^3$ dependence (r is the distance between to interacting points). Such an interaction is quite common in nature. To account for a layer of polar molecules with electric dipoles, one can simply replace the third term with $1/2\int_A p_3 E_3 dA$. Here p_3 is the electric dipole moment per area, and E_3 is the corresponding electric field associated with the dipole distribution. While different in the physical origin, the interaction term shows a similar mathematical structure. Thus the discussion below applies to a wide range of systems.

Domain patterns emerge by a diffusion process to reduce the free energy. The diffusion flux, **J**, is proportional to the gradient of chemical potential, $\mu = \delta G/\delta C$, namely $\mathbf{J} = -M(\mathbf{x})\nabla\mu$. To consider regionally activated self-assembly, we allow the mobility $M(\mathbf{x})$ to be position-dependent. We take $M(\mathbf{x}) = M_0$ in the activated region,

where M_0 is the mobility for diffusion, and $M(\mathbf{x}) = 0$ in other regions. Substituting the diffusion flux into the mass conservation equation, $\Lambda \partial C / \partial t + \nabla \cdot \mathbf{J} = 0$, where Λ is the number of atomic sites per unit area, gives a diffusion equation [24],

$$\frac{\partial C}{\partial t} = \frac{1}{\Lambda^2} \nabla \left(M \nabla \left(\frac{\partial g}{\partial C} - 2h \nabla^2 C + \phi \varepsilon_{\beta\beta} \right) \right). \tag{2.2}$$

Here ϕ is the surface stress difference of the two species, and $\varepsilon_{\beta\beta} = -\left(1-\nu^2\right)\phi R / \pi E$ is the surface strain with E being the Young's modulus and ν the Poisson's ratio. R is an area integration characterizing the long range interaction, which is given by

$$R = \iint \frac{\left(x_1 - \xi_1\right)\dfrac{\partial C}{\partial \xi_1} + \left(x_2 - \xi_2\right)\dfrac{\partial C}{\partial \xi_2}}{\left[\left(x_1 - \xi_1\right)^2 + \left(x_2 - \xi_2\right)^2\right]^{3/2}} d\xi_1 d\xi_2 \tag{2.3}$$

To describe phase separation, one can take any double well function for $g(C)$. We take a regular solution, $g(C) = g_{\mathrm{A}}(1-C) + g_{\mathrm{B}} C + \Lambda k_B T \left[C \ln C + (1-C)\ln(1-C) + \Omega C (1-C) \right]$, where g_{A} or g_{B} is the chemical energy of pure A or pure B. The first two terms in the bracket result from the entropy of mixing, and the third term from the energy of mixing. The dimensionless number Ω measures the exchange energy relative to the thermal energy $k_B T$, where k_B is the Boltzmann constant and T is temperature.

Equation 2.2 can be written in a dimensionless form by scaling the coordinates with $\sqrt{h / \Lambda k_B T}$ and the time with $h / M_0 \left(k_B T\right)^2$, which gives

$$\frac{\partial C}{\partial t} = \nabla \cdot \left(M \nabla \left[P(C) - 2\nabla^2 C - \frac{Q}{\pi} R \right] \right). \tag{2.4}$$

Here M is a normalized mobility taking values of 0 or 1,

$P(C) = \ln[C/(1-C)] + \Omega(1-2C)$, and $Q = l/b$ is the ratio of characteristic scale of domain width, $b = \sqrt{h/\Lambda k_B T}$, and size, $l = Eh/\left(1-\nu^2\right)\phi^2$.

The diffusion equation has a simple form in Fourier space,

$$\frac{\partial \hat{C}}{\partial t} = i\mathbf{k} \cdot \{M(\mathbf{x})(i\mathbf{k}\hat{\mu})_r\}_k, \tag{2.5}$$

where the hat and subscript 'k' denote Fourier transform, 'r' denotes inverse Fourier transform, and $\mathbf{k}$ is the wave number vector. The chemical potential, $\mu = P(C) - 2\nabla^2 C - QR/\pi$, has a Fourier transform of $\hat{\mu} = \hat{P} + 2(k^2 - kQ)\hat{C}$. P is a nonlinear function of C, so $\hat{P}$ is calculated by numerical Fourier transform. We adopted a semi-implicit method [28] for the time integration for enhanced computational stability.

2.4 Grow long-range ordered superlattice by sequential activation of self-assembly

2.4.1 Sequential activation of self-assembly

The essence of our approach is sequential activation of self-assembly. The idea is illustrated in Figure 2.4. A binary monolayer is used as an example, which may separate into two phases and self-assemble into domain patterns such as a hexagonal lattice of dots. Typically multiple grains of dots will form due to simultaneous self-assembly at different locations, producing a pattern lack of long-range order. Here we propose to first activate self-assembly in a finite mobile region, where atoms are allowed to diffuse and form domain patterns. This initial mobile region will serve as a "seed". The seed does not need to have a perfect lattice. We then shift the mobile region like scanning. The self-assembly in the newly activated region will be influenced by the pattern already formed in the seed. In experiments, we envision that this process can be achieved by laser or ion beam scanning to control the local temperature, so that diffusion is activated sequentially at each spot along the scanning path. We show that this sequential activation will lead to a large long-range ordered domain pattern even if we start with an imperfect seed. The pattern quickly improves and converges to a perfect superlattice along with the sequential activation. More interestingly, the self-activation of self-assembly can be achieved under certain conditions. In other words, the self-assembly in a small region may induce a domino effect and produce a perfect lattice expanding spontaneously without the need of explicit sequential activation such as laser scanning. Note that sequential activation of self-assembly is fundamentally different from crystal growth. The former expands by the

simultaneous formation and ordering of domains, while the latter grows by the attachment of atoms with a fixed size and interatomic distance.

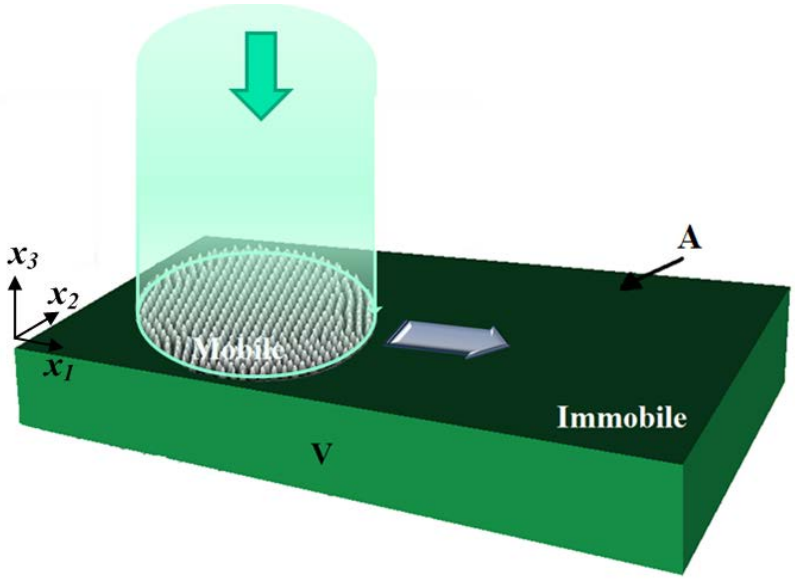

Figure 2.4 A schematic of sequential activation of self-assembly. Self-assembly is first activated in a finite mobile region, where atoms are allowed to diffuse and form domain patterns. This initial mobile region serves as a "seed".

2.4.2 Simulation results

Simulations were carried out with Ω=1.6, Q=1.6, and a calculation cell size of 512×512 grids with a grid spacing of 1. Periodic boundary condition was applied to extend the cell to the entire plane. Initial conditions were random, i.e. the initial concentration had an average of C_0 with a random fluctuation within 0.001.

We first demonstrate the growth of long-range ordered superlattices from a seed by sequential activation of self-assembly. Representative results are shown in Figure 2.5

Rather than placing a perfect lattice directly, we grew the seed on site. Take Fig. 2.5(a) as an example. The initial concentration was $C_0 = 0.37$ everywhere. We assigned mobility to be 1 in the square mobile region. We evolved the entire calculation cell to $t = 10^5$. The constraint of kinetics led to a square seed composed of white B-rich phase in the matrix of black A-rich phase. We found that smaller seeds had fewer defects. Here we took a square seed with a size of 192×192, which was larger than the size of a typical single grain. Therefore defects such as misalignment and multiple grains appeared in this seed. Next we shifted the mobile region to the right, which we called scanning. The shift distance in each step was much smaller compared to the seed size, which created a continuous scanning effect. The scanning velocity was chosen to ensure ample time for new domains to develop. In simulations we shifted the mobile region by one grid spacing, allowed it to evolve for a time duration of 10^4, and then shifted it further. This process gave an effective scanning velocity of 10^{-4}. Figure 2.5(b) shows the structure after we scanned over the width of the calculation cell, which formed a band of nicely ordered hexagonal superlattice. Noticeably, the lattice improved to perfection along with the scanning, demonstrating the tolerance of defects in the seeds. Figures 2.5(c) and 2.5(d) show a circular seed and its growth pattern. Unlike straight boundaries in the square seed, the circular boundary does not have any fixed relevance to the grain orientation in the seed. We still obtained a nicely-ordered superlattice consistent with the prevalent orientation in the seed. These results suggest that the scanning approach is not affected by the shape of the seed. This behavior is in contrast to the geometrical templating, which relies on the boundary shape to guide self-assembly.

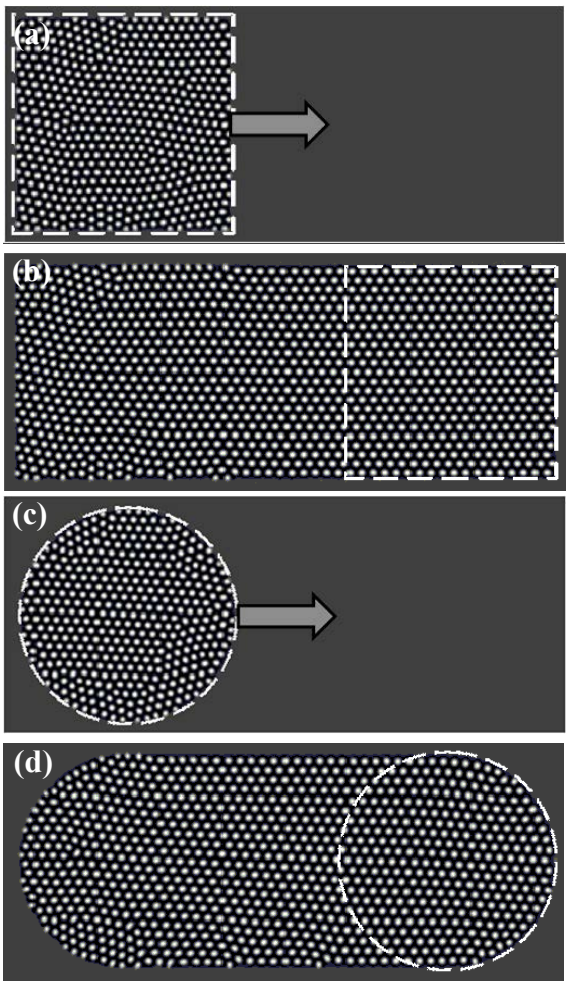

Figure 2.5 Growth of superlattice from seeds. $C_0 = 0.37$. (a) A square seed. (b) A band of nicely ordered hexagonal superlattice formed after scanning over the width. The lattice improved to perfect along with the scanning, demonstrating tolerance of defects in the seeds. (c) A circular seed. (d) Superlattice formed after scanning. The circular boundary does not have any fixed relevance to the grain orientation in the seed, suggesting that the scanning approach is not affected by the shape of the seed.

2.4.3 Discussions

The seeding effect can be better understood by looking into the third term in Eq. (2.4), which reflects the long-range interaction through *R*. The field induced by the seed is key to the interaction between the modulated phases in the seed and its homogeneous neighbor where the concentration is still uniform. To quantify the field, we calculated the

R distribution as shown in Figure 2.6 (b), which corresponds to the domain pattern in Figure 2.6 (a). The highs and lows of the *R* field and the domain pattern are consistent. Outside the seed, the *R* field promotes phase separation so that B-rich dots emerge at the locations of high *R*. This preference causes the dots to form at the right spots. The *R* field decays quickly away from the seed. Below we refer the mobile region just ahead of the seed as growth front, which experiences a significant *R* effect.

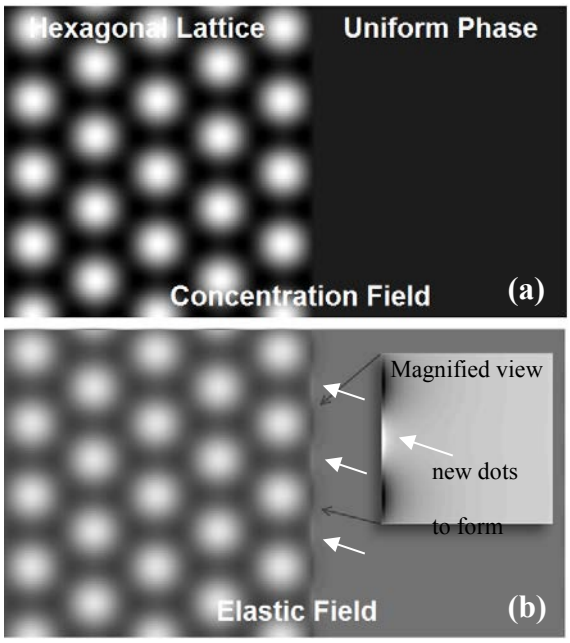

Figure 2.6 How a seed affects self-assembly by the *R* field. (a) A seed region and its homogenous neighbor. (b) The corresponding *R* distribution in grey scale, brighter for higher *R*. This field promotes phase separation so that B-rich dots emerge at locations of high *R*. This preference causes the dots to form at the right lattice spots.

We identified two scenarios that the long-range field of a seed may direct the location of new domains (dots). 1) New domains emerge at the right lattice spots during the stage of phase separation. 2) New domains emerge at locally preferred locations and then migrate to the right spots under the influence of the seed. Our simulations suggest that if the seed has a close to perfect lattice, scenario 1 dominates the process. However,

when the seed contains major defects such as significant misalignment, the pattern formation process shows complicated dynamics and scenario 2 dominates. In this situation the seed can experience significant self-adjustment, since part of the seeds is mobile before the mobile region shifts completely outside of the seed region. When the portion of seed next to the growth front lacks any prevailing grain orientation, it is difficult to form a single grain lattice in the growth front to match the poly grain boundary of the seed. As a result, new domains emerge at locally preferred locations. This disordered region, including the growth front and the portion of seed next to it, demonstrates realignment and local rotation to negotiate a common lattice orientation. After the lattice improves, scenario 1 dominates the following scanning.

We found the scanning velocity can control the domain pattern when the system is in a bistable state. This state refers to a window of average concentration, where both hexagonal lattice of dots and striped arrays can stabilize. Stability analysis shows that this window is $0.41<C_0<0.47$ for Ω=1.6, Q=1.6 [29]. The hexagonal pattern is stable for $0.34 < C_0 < 0.41$, the striped array pattern is stable for $C_0 > 0.47$ and the bistable state lies between the two regimes. A homogenous epilayer has lower energy for $C_0 < 0.34$, when no domain pattern forms. We took C_0 to be 0.42 which is within the window of the bistable state. Figure 2.7 (a) shows the pattern in the seed grown in the same way as that in Figure 2.5. The seed consists of ordered dots with few very short stripes. However, when we scanned with the same velocity of 10^{-4} as before, a band of parallel stripes formed. The slow scanning velocity allowed the pattern to evolve close to equilibrium in each scanning step. Note that these stripes did not take over the dots in the seed, suggesting that they can coexist. In Figure 2.7 (c), we increased the scanning velocity to

0.5. Surprisingly, a band of hexagonal lattice of dots formed. This phenomenon reflects a non-equilibrium growth mode, where new domains do not have much time to relax before the mobile region shifts. This observation suggests a new growth mechanism controlled by scanning velocity, which manipulates the competition between domain coarsening and growth. At low velocity, new domains have sufficient time to coarsen into parallel stripes, which have lower energy. Here the regular spacing of dots in the seed has provided an important guidance, since a pattern of parallel stripes is difficult to form spontaneously. At high velocity, new domains do not have much time to coarsen so that they form a lattice of dots. Figure 2.7 (d) shows a "phase diagram" of patterns in terms of the scanning velocity and average concentration. This diagram was obtained by calculating a series of combination of the scanning velocity and average concentration. The unique effect of kinetic guidance divides the patterns into two regimes, stripes and dots, with a transition region of mixed patterns in between.

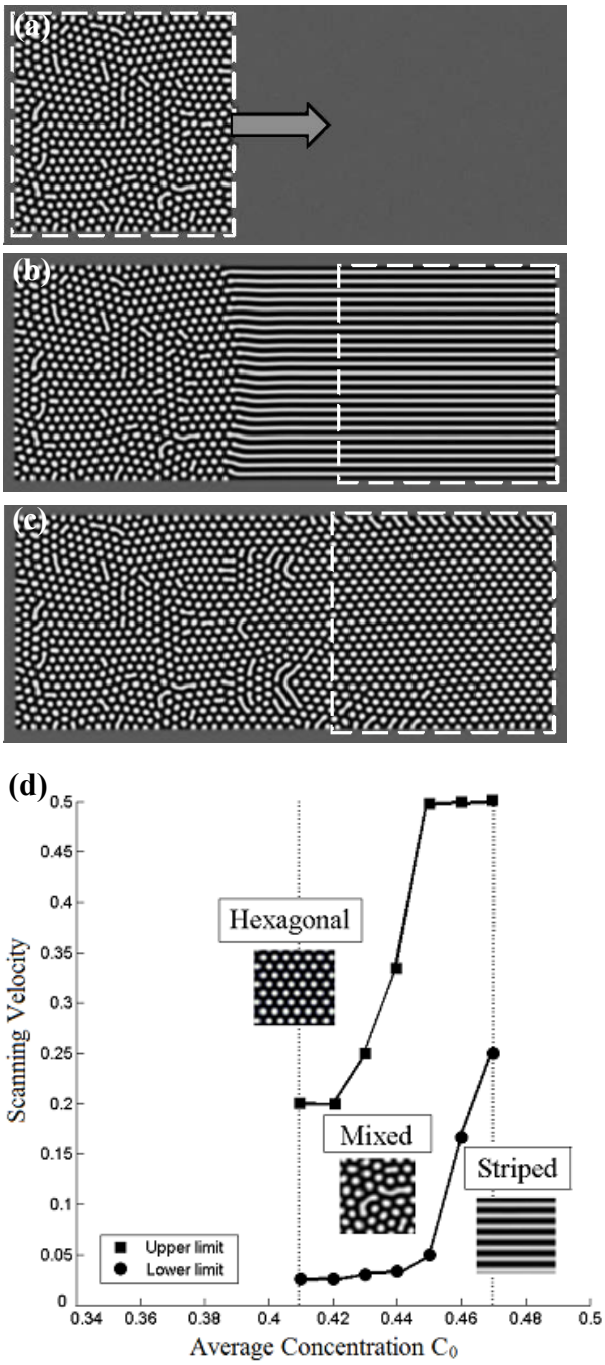

Figure 2.7 Scanning velocity can control the domain pattern when the system is in a bistable state, $C_0 = 0.42$. (a) A square seed. (b) A band of parallel stripes formed at scanning velocity of 10^{-4}. (c) A band of hexagonal lattice of dots formed at scanning velocity of 0.5. (d) A pattern diagram in terms of scanning velocity and average concentration.

High output is essential to nanostructure applications. We propose two schemes to facilitate large-scale fabrication. 1) As shown in Figure 2.8 (a), we alternated the scanning directions between left-right scanning and up-down scanning, using the superlattice created in each previous step as a large seed. This scheme allowed the growth rate (area of lattice created per unit time) to increase exponentially with time, greatly accelerating large area fabrication. 2) As shown in Figure 2.8 (b), we increased the size of the mobile area in two dimensions, rather than scanning along one direction. This scheme allowed the growth rate to be quadratic of the scanning velocity.

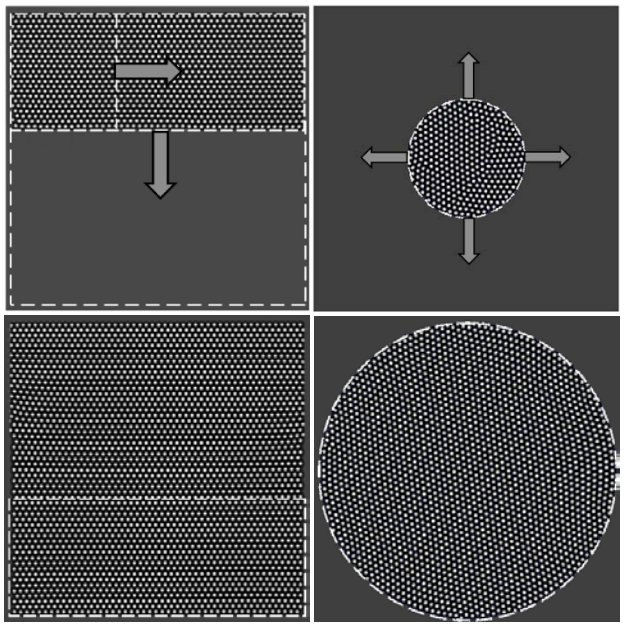

Figure 2.8 Two schemes for scaling-up growth. (a) Alternate the scanning directions, using the superlattice created in previous step as a large seed. (b) Increase the size of the mobile in two dimension.

2.5 Spontaneous propagation of self-assembly in a continuum medium

2.5.1 Propagation and self-assembly

Propagation phenomena are widely observed in nature and human activities. Examples include solidification[30], tumor growth[31], frontal polymerization of actin[32], chemical chain reaction[33], to population dynamics[34]. These phenomena can usually be described by the general diffusion-reaction model[35] with corresponding reaction terms. Moreover, these processes usually begin with a stage small in extent and then propagate over a large area. In contrast, self-assembled patterns are usually formed large in extent with no propagation.

The question we aim to address is: can self-assembly propagate? Is it possible for a system to self-assemble locally to form a regular domain pattern, and then replicate this pattern spontaneously to distance? We envision a mechanism as below. Consider a homogeneous system stable against small perturbation so that self-assembly does not occur spontaneously. Upon activation of self-assembly in a local region, the formed ordered pattern may produce sufficient destabilizing effect through long-range interaction to trigger self-assembly in its immediate surrounding areas. The newly formed structures inherit the same order information and further destabilize their neighbors. The chain reaction may propel the propagation of self-assembly into distance and generate an extreme long-range order.

There are few studies on the propagation of self-assembly on its strict definition. Some research has considered self-assembly in the loose sense, which refers to the

aggregation of building blocks without forming any ordered pattern. For example, propagating aggregation waves were demonstrated in an organosilane monolayer system[36]. The organic molecules aggregated when the concentration was higher than a critical value. The propagation was driven by concentration gradient. In another experimental study, the propagation of patterns in Langmuir monolayer at liquid-air interface was shown[37]. A local disturbance was driven by a constant external light excitation and the propagation was maintained via elastic forces. Although propagation phenomenon was reported in these systems, there were no explicit ordered patterns formed. We show that the propagation of self-assembly can carry ordering information and transmit it through intrinsic interaction between domains.

2.5.2 Simulation results

Take the same elastic dipole interaction induced by surface stress as an example, the normalized diffusion equation is [24]

$$\frac{\partial C}{\partial t} = \nabla^2 \left[\frac{df}{dC} - 2\nabla^2 C + QI \right]. \tag{2.6}$$

Here Q is a dimensionless number scales with the ratio of interface width and domain size. I is an area integration over the substrate surface characterizing the long-range interaction, namely

$$I(x,y) = -\frac{1}{\pi} \iint_A \frac{(x-\xi)\frac{\partial C}{\partial \xi} + (y-\eta)\frac{\partial C}{\partial \eta}}{\left[(x-\xi)^2 + (y-\eta)^2 \right]^{3/2}} d\xi d\eta \tag{2.7}$$

The condition of self-assembly can be obtained from linear stability analysis. Assume a regular solution $f(C) = C\ln C + (1-C)\ln(1-C) + \Omega C(1-C)$, where Ω is a dimensionless number measuring the bond strength relative to the thermal energy. The curve $f(C)$ is convex and prefers a homogenous film when $\Omega < 2$. Consider a perturbation $C(x,t) = C_0 + q(t)\sin(kx)$, where C_0 is the average concentration. The solution of Eq. (2.6) is $q = q_0 e^{\alpha t}$, where q_0 is the initial amplitude and $\alpha = k^2[-1/[C_0(1-C_0)] + 2\Omega - 2k^2 + 2Qk]$. With $\alpha \le 0$ for all k, the perturbation amplitude *q* decays with time so that a homogeneous film is stable against small perturbation. This condition corresponds to $C_0 \le C_L$ or a symmetric case of $C_0 \ge C_H$, where $C_L = \left(1-\sqrt{1-s}\right)/2$, $C_H = \left(1+\sqrt{1-s}\right)/2$, and $s = 8/\left(Q^2 + 4\Omega\right)$. Self-assembly occurs for $C_L < C_0 < C_H$. With Ω=1.3 and *Q*=1.8 we have $C_L = 0.386$ and $C_H = 0.614$.

Unlike common study of self-assembly, here we focus on the stable regime $C_0 \le C_L$. Figure 2.9 demonstrates how self-assembly can propagate under such a condition. We performed fully non-linear simulation of Eq. (2.6) in Fourier space. The initial condition was set to fluctuate randomly within 0.001 from an average. We took Ω=1.3 and *Q*=1.8. The film was initially homogeneous with an average concentration of C_0=0.38 (below C_L), which was stable against small perturbation. We introduced a small initiation zone at the left edge by increasing its local concentration to 0.42 (above C_L) for self-assembly to occur. The width of the rectangular initiation zone is roughly the diameter of a self-assembled dot. This ensures that an array of dots is aligned along the y axis. In experiments we envision that this process can be achieved by local mass deposition. The area of the initiation zone may be expanded to the size of one single grain

so that no defects are introduced. Upon pattern formation, the nearby homogeneous region was disturbed and became unstable. Self-assembly propagated and generated a uniform lattice of dots in the entire film without any defects. To eliminate the boundary effect, the presented results were cropped from a larger calculation cell of 2048×48. Periodic boundary condition was applied to extend the cell to the entire plane. We placed the initiation zone in the middle of the stripe so that self-assembly actually propagated symmetrically toward two sides. The right 512×48 was shown in Figure 2.9. The intriguing propagation poses interesting questions. Why does self-assembly propagate and what determines the rate? How can we control the propagation process?

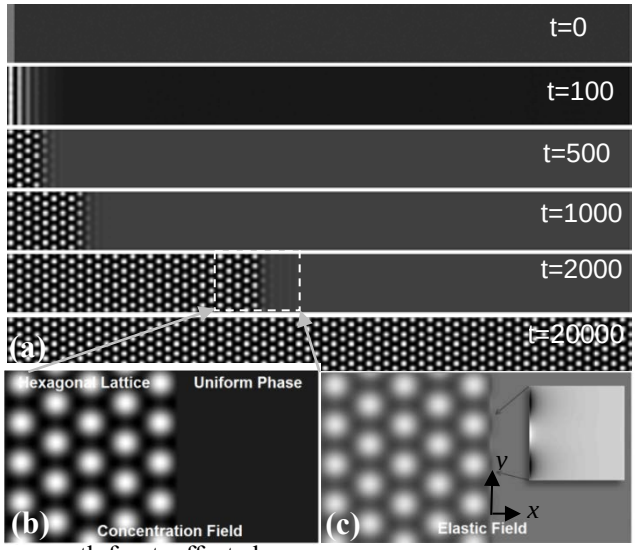

Figure 2.9 Spontaneous propagation of self-assembly in a homogenous film. (a) The propagation was initiated by a local deposition at the left edge. The locally self-assembled structure as a precursor destabilized its initially stable surrounding areas through a dipole-type interaction. The newly formed structures inherited the same order information from the precursor and further activated the self-assembly of their neighbors. This process caused spatial extension of self-assembly and replication of the order, producing a long-range ordered superlattice without defects. (b) Magnified concentration field. (c) The corresponding *I* field is in phase with the pattern. Q=1.8, Ω=1.3.

While we started self-assembly in a small initiation zone by giving it a concentration higher than C_L , this amount had negligible effect on the average concentration of the entire film. Thus the propagation was not due to the long-range diffusion of higher concentration. We believe that the self-sustained propagation relies on the interaction between the ordered structure in the propagation front and the homogenous region immediately ahead of it, which we call affected zone. Equation (2.6) shows that the *I* term is negligible when the film is homogeneous with small random noise. In contrast, the self-assembled pattern in the propagation front induces a dipole-type *I* field that is in phase with the pattern and extends into the affected zone, as shown in Fig. 2.9. How this field triggers self-assembly propagation is related to the free energy. For a hexagonal pattern of dots lining up along the *y* direction with a lattice space of *d*, as shown in the inset of Fig. 2.10 (a), the concentration field can be represented by

$$C(x,y) = C_0 + \sum_m q_{m0}\cos\left(m\frac{2\pi x}{\sqrt{3}d}\right) + \sum_n q_{0n}\cos\left(n\frac{2\pi y}{d}\right) + \sum_{m,n} q_{mn}\cos\left(m\frac{2\pi x}{\sqrt{3}d}\right)\cos\left(n\frac{2\pi y}{d}\right) \tag{2.8}$$

The summations run from 1 to ∞. Minimization of the free energy in terms of *d* gives the equilibrium size, $d = 4\pi S / QH$ and free energy per area, $g = L - Q^2H^2 / 8S$. Here $S = \sum_m m^2 q_{m0}^2 / 3 + \sum_n n^2 q_{0n}^2 + 1/2\sum_{m,n}(m^2/3 + n^2)q_{mn}^2$ and $H = \sum_m m q_{m0}^2 / \sqrt{3} + \sum_n n q_{0n}^2 + 1/2\sum_{m,n} q_{mn}^2\sqrt{m^2/3 + n^2}$ depend only on the geometry, and not the scale, of the patterns, while $L = \int_{-1/2}^{1/2}\int_{-1/2}^{1/2}[C\ln C + (1-C)\ln(1-C) + \Omega C(1-C)]d\xi_1 d\xi_2$, $\xi_1 = x/\sqrt{3}d$, $\xi_2 = y/d$. We

further minimize g with respect to q_{m0}, q_{0n}, and q_{mn} by the conjugate-gradient method to obtain the free energy per area of a hexagonal lattice of dots, as shown in Fig. 2.10 (a). For a homogenous film the free energy density is simply L evaluated at C_0. The hexagonal pattern has lower energy than a homogenous film when the concentration is higher than a critical value, C_D. The range between C_D and C_L creates a special bistable state, where a homogenous film is stable against small perturbation yet the hexagonal pattern has lower energy. The concentration C_0 in Fig. 2.9 falls in this bistable state. As illustrated in Fig. 2.10 (b), self-assembly from a homogenous film (H) to the dot pattern (D) will reduce the free energy by Δg_{H-D}, but it needs help to first overcome an energy battier, Δg_b.

The ordered pattern in the growth front helps to eliminate the energy battier in the affected zone by the I field, which modulates in y and decays quickly in x. We approximate the field by $I_a(x,y) = \sum_l a_l \cos(2\pi l y/d + \theta) e^{-kx}$, where a_l is amplitude, θ is the phase angle relative to the perturbation to be examined in the affected zone and k is a decay parameter. Due to its proximity to an ordered pattern, a homogenous film perturbed in the affected zone by the form of Eq. (2.8) has an additional free energy per area,

$$\Delta g_a = -\frac{(1-e^{-\sqrt{3}kd})Q}{2\sqrt{3}kd} \sum_n a_n \cos\theta \left[q_{0n} + \sum_m \frac{q_{mn}}{1+\left(2m\pi/\sqrt{3}kd\right)^2} \right]. \qquad (2.9)$$

The negative Δg_a promotes the destabilization of a homogenous film by more energy reduction. In addition, Δg_a minimizes at $\theta = 0$, suggesting that any emerging pattern will

prefer to be in phase with I_a or the existing pattern in the growth front. This effect explains why the subsequent dot pattern follows the same orientation and extremely long-range ordered lattice can form. The term Δg_a is also proportional to the perturbation amplitudes q_{0n} and q_{mn}, suggesting more energy reduction as the pattern grows. Self-assembly in the affected zone occurs when Δg_a removes the energy barrier. Then the following propagation appears like an autocatalytic process transitioning from a homogenous film to a dot pattern, or $H \xrightarrow{D} D$.

2.5.3 Discussions

Effect of long-range diffusion. The propagation process may be accompanied by a significant gradient-driven long-range diffusion if the average concentration of the dot pattern, C_p, is quite different from C_0. This situation may happen since a dot pattern can reach lower free energy if it raises its average concentration above C_0, as shown by the monotonic curve in Fig. 2.10 (a). To maintain an overall C_0, the homogenous film ahead of the growth front has to reduce its average concentration, which increase its free energy. After a balance is reached, a region with an average concentration C_a ($C_a < C_0$) is formed ahead of the growth front, as illustrated in the inset of Fig. 2.10 (b). Then the concentration gradient drives long-range diffusion from the remote area in the homogenous film to the affected zone by a diffusion distance *d*. The lower C_a in the affected zone makes it more stable since it is further from C_L.

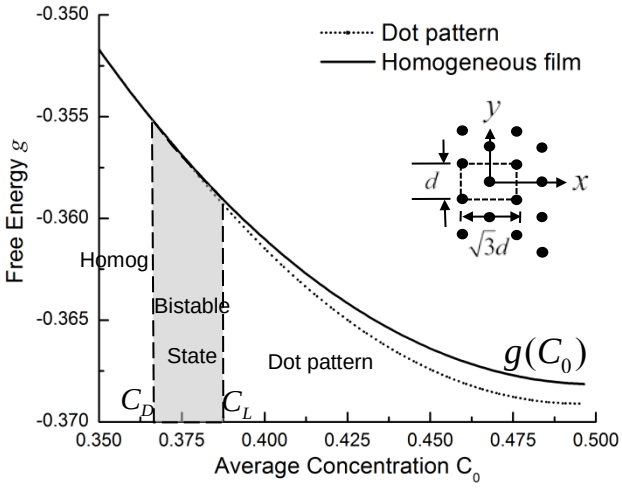

(a)

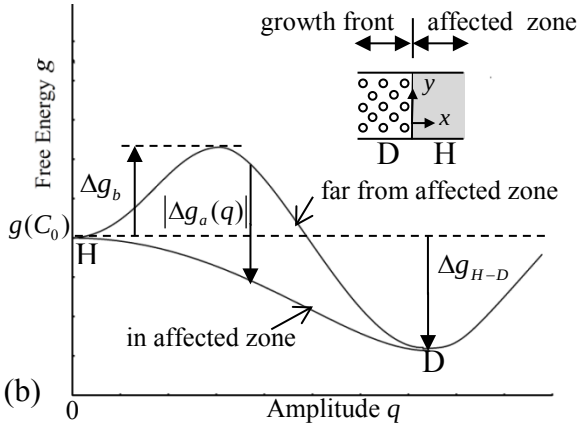

(b)

Figure 2.10 (a) Free energy of homogenous film and dot pattern. The hexagonal dot pattern has lower energy when its average concentration is higher than a critical value, C_D . The range between C_D and C_L is a bistable state, where a homogenous film is stable against small perturbation although the dot pattern has lower energy. (b) Illustration of free energy change during perturbation growth. The ordered pattern in the growth front removes the energy barrier, Δg_b, in the affected zone, causing a homogenous film (H) to self-assemble into a dot pattern (D). Q=1.8, Ω=1.3.

The long-range diffusion is necessary to sustain the pattern growth when it maintains an average concentration higher than C_0. The accumulated concentration relocation to the dot pattern increases at it expands. Thus the diffusion distance or the front width, *d*, increases with the propagation of self-assembly. The diffusion rate reduces as a result of the decreasing concentration gradient, $(C_0 - C_a)/d$, which slows down the propagation of self-assembly. This trend can be clearly observed through the decreasing slope of the *Q*=1.7 curve in Fig. 2.11. We have found an effective approach to control the propagation rate by tuning how much it is limited by long-range diffusion. The triggering *I* field from the growth front affects how fast self-assembly emerges in the affected zone, while the long-range diffusion affects how fast the mass transport is. Thus the propagation would be faster for a larger triggering field and minimal requirement of long-range diffusion, which translate to larger *Q* and smaller Ω. The $f(C)$ curve is more steep for smaller Ω, thus makes it more energetically unfavorable for a uniform film to decrease its concentration for a higher average concentration of the dot pattern. Therefore the dot pattern would maintain an average concentration close to C_0 and does not need much long-range diffusion during propagation. As shown in Fig. 2.11, the propagation slows down significantly with *Q*=1.7, Ω =1.4, while keeps an almost constant rate with *Q*=1.8, Ω =1.3. Generally speaking, we can classify the propagation of self-assembly into two modes: long range diffusion-limited and activation-limited. The former situation is similar to many frontal propagations [32, 36, 38], when the fronts move forward at the cost of background concentration. For actin polymerization, the propagation stops automatically when the surrounding concentration decreases to a critical value. To prevent the cease of propagation, one could manually keep the background concentration

invariant by constantly adding reactive materials [36]. The latter involves little or no long-range diffusion, and is determined only by the local transport for concentration modulation. Without the requirement of the mass replenishment, this scenario is unique and preferred for potential large-scale nanofabrication.

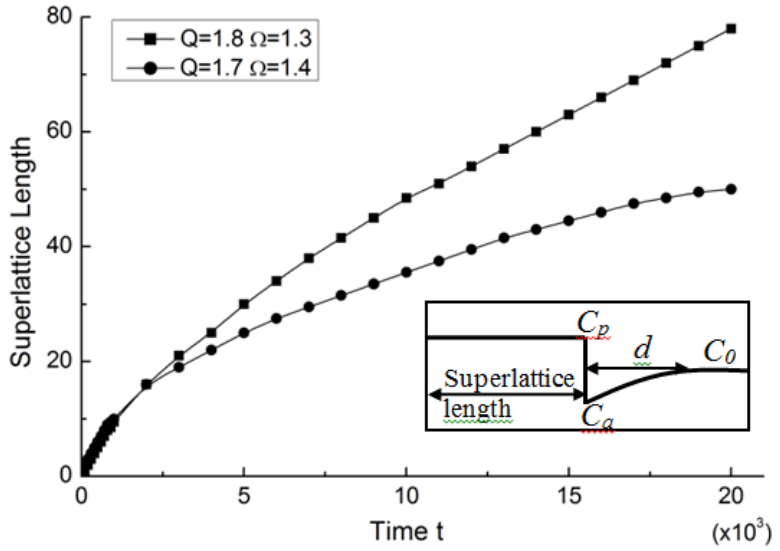

Figure 2.11 Growth of dot superlattice by propagation of self-assembly (superlattice length normalized by the diameter of a dot). The upper curve shows activation-limited propagation. Q=1.8, Ω=1.3. The lower curve shows long range diffusion-limited propagation. Q=1.7, Ω=1.4. The inset illustrates propagation accompanied by long-range diffusion. The average concentration of the dot pattern, C_p, is higher than C_0, while the average concentration in the affected zone, C_a, is less than C_0. The concentration gradient drives long-range diffusion from the remote area in the homogenous film to the affected zone by a diffusion distance d.

Propagation can also happen in two-dimensions, as demonstrated in Fig. 2.12. Starting with a circular initiation zone, the hexagonal pattern quickly expands to the entire area. Defect-free patterns are produced in a high output manner.

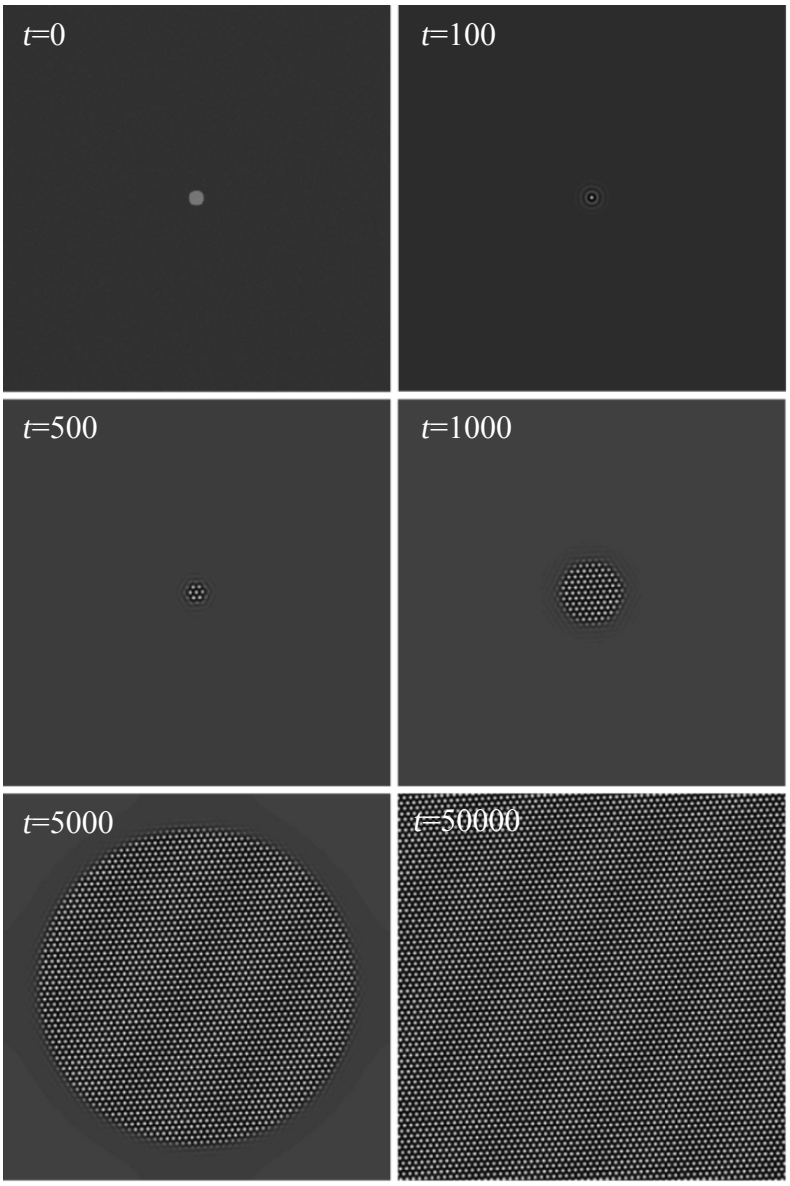

Figure 2.12 Propagation of self-assembly in two-dimensions. Q=1.8, Ω=1.3.

Effect of thermal fluctuations. In real systems, temperature and fluctuation can affect the propagation. With increasing temperature, a higher propagation rate is generally expected due to higher mobility. Thermal fluctuation usually causes the broadening of the front width in a typical propagating system[39]. To consider the

fluctuation effect, a random "white noise" term $\varepsilon(\mathbf{x},t)$ can be added to the right hand side of Eq. (1). This random term obeys the fluctuation dissipation theorem so that $\langle \varepsilon(\mathbf{x},t)\varepsilon(\mathbf{x}',t') \rangle$ scales with $k_b T \delta(\mathbf{x}-\mathbf{x}')\delta(t-t')$, where k_b is Boltzmann's constant, and T is the absolute temperature [40]. The fluctuation is small compared to the average concentration, and therefore has minimum effect on the equilibrium size of the domains, as can be seen from the derived dispersion relation $\alpha(k)$. In our system the dipole interaction dominates at the propagation front, thus the fluctuation would not significantly affect the growth front width.

2.6 Connections to representative systems

Equations (2.4) and (2.5) are dimensionless, so that the simulation results are representative of a wide range of materials systems having different pattern size scales. A particularly interesting system is substrate-mediated spinodal decomposition of a binary epitaxial monolayer or thin film separating into A-rich and B-rich domains [19, 25]. This system can also be a submonolayer of adsorbates on a substrate, where one phase is the adsorbate and the other phase is simply the bare substrate surface. Using magnitudes h~10^{-19}J, Λ~5×10^{19} m^{-2} and k_BT ~5×10^{-21} J (corresponding to T =400K), we have b~0.6nm. In simulations a grid spacing of 1 corresponds to a physical spacing of b. Assuming that the Young's modulus of the substrate is E~10^{11} N/m^2 , the Poisson's ratio is ν ~0.3, the surface stress difference of two domains is on the order of ϕ ~1─4N/m [41], we have a characteristic size scale l~0.6─10nm. The domain size is roughly $4\pi l$. A larger surface stress difference, and a smaller interfacial tension and substrate stiffness lead to smaller domain sizes.

The value of h can be related to the interfacial tension, γ, between A-rich and B-rich domains by an integration across the interface, namely $\gamma = h\int_{-\infty}^{\infty}\left(\partial C/\partial x\right)^2 dx$. Experimentally the gradient in the interfacial region can be approximated by $\Delta C/\delta$, where ΔC is the concentration difference of the two phases, and δ is the interfacial thickness. This approximation gives $h = \gamma\delta/(\Delta C)^2$.

For a system with quite different magnitudes of b and l, it is computational intensive to resolve both the interface and multiple domains. In most cases we are interested in the domain size and patterning, when it is not necessary to resolve

accurately the interfacial transition. In such situations one may treat *b* as a spatial resolution to be resolved in the simulation, whose value is given by l/Q. Here l is calculated from material parameters and determines the physical size scale. The parameter Q controls the spatial resolution and the number of domains to appear in a calculation cell.

Equation (2.4) may also be connected to other systems where the long-range interaction is electric dipole [42, 43] instead of elasticity. Examples include Langmuir films and adsorbates of dipole molecules. The former has a typical domain size of 1—10μm [44] while the latter has a typical size of 1-100nm. These sizes can be converted to the characteristic size scale by the relation of $4\pi l$. Domain patterns are also encountered in polymeric assemblies during microphase separation [45, 46]. The connectivity of molecular blocks precludes composition modulation over large length scale, leading to an effective long rang interaction similar to dipole interactions. In analogy to $l \sim Eh/\phi^2$ for epitaxial layers, from dimensional analysis we have a characteristic scale $l \sim \varepsilon h/\eta^2$ for systems involving dipole interaction, where ε is the permittivity of the media and η is the dipole density (electric dipole moments per unit area) difference of A-rich and B-rich domains. Thus a larger dipole density difference and a smaller interfacial tension reduce the domain sizes.

2.7 References

1. Parviz, B.A., D. Ryan, and G.M. Whitesides, *Using Self-Assembly for the Fabrication of Nano-Scale Electronic and Photonic Devices.* Ieee Transactions on Advanced Packaging, 2003. **26**(3): p. 233-241.

2. Nam, J.M., C.S. Thaxton, and C.A. Mirkin, *Nanoparticle-Based Bio-Bar Codes for the Ultrasensitive Detection of Proteins.* Science, 2003. **301**(5641): p. 1884-1886.

3. Xia, Y.N., *Nanomaterials at Work in Biomedical Research.* Nature Materials, 2008. **7**(10): p. 758-760.

4. Klajn, R., et al., *Plastic and Moldable Metals by Self-Assembly of Sticky Nanoparticle Aggregates.* Science, 2007. **316**(5822): p. 261-264.

5. Shevchenko, E.V., et al., *Structural Diversity in Binary Nanoparticle Superlattices.* Nature, 2006. **439**(7072): p. 55-59.

6. Paquet, C. and E. Kumacheva, *Nanostructured Polymers for Photonics.* Materials Today, 2008. **11**(4): p. 48-56.

7. Hodes, G., *When Small Is Different: Some Recent Advances in Concepts and Applications of Nanoscale Phenomena.* Advanced Materials, 2007. **19**(5): p. 639-655.

8. Murray, W.A. and W.L. Barnes, *Plasmonic Materials.* Advanced Materials, 2007. **19**(22): p. 3771-3782.

9. Xu, J., et al., *Directed Self-Assembly of Block Copolymers on Two-Dimensional Chemical Patterns Fabricated by Electro-Oxidation Nano lithography.* Advanced Materials, 2010. **22**(20): p. 2268-2272.

10. Mei, X., et al., *Molecular-beam Epitaxial Growth of GaAs and InGaAs/GaAs Nanodot Arrays Using Anodic Al_2O_3 Nanohole Array Template Masks.* Applied Physics Letters, 2002. **81**(2): p. 361-363.

11. Strom, N.W., et al., *Self-Assembled InAs Quantum Dot Formation on GaAs Ring-Like Nanostructure Templates.* Nanoscale Research Letters, 2007. **2**(2): p. 112-117.

12. Ghadimi, A., et al., *Plasma within Templates: Molding Flexible Nanocrystal Solids into Multifunctional Architectures.* Nano Letters, 2007. **7**(12): p. 3864-3868.

13. Nykypanchuk, D., et al., *DNA-Guided Crystallization of Colloidal Nanoparticles.* Nature, 2008. **451**(7178): p. 549-552.

14. Bigioni, T.P., et al., *Kinetically Driven Self Assembly of Highly Ordered Nanoparticle Monolayers.* Nature Materials, 2006. **5**(4): p. 265-270.

15. Chik, H., et al., *Periodic Array of Uniform ZnO Nanorods by Second-Order Self-Assembly.* Applied Physics Letters, 2004. **84**(17): p. 3376-3378.

16. Pierrat, S., et al., *Self-Assembly of Small Gold Colloids with Functionalized Gold Nanorods.* Nano Letters, 2007. **7**(2): p. 259-263.

17. Chen, S.H., Z.Y. Fan, and D.L. Carroll, *Silver Nanodisks: Synthesis, Characterization, and Self-Assembly.* Journal of Physical Chemistry B, 2002. **106**(42): p. 10777-10781.

18. Zhang, H.T., G. Wu, and X.H. Chen, *Large-scale Synthesis and Self-assembly of Monodisperse Hexagon Cu2S Nanoplates.* Langmuir, 2005. **21**(10): p. 4281-4282.

19. Plass, R., et al., *Nanostructures - Self-assembled Domain Patterns.* Nature, 2001. **412**(6850): p. 875-875.

20. Fasolka, M.J. and A.M. Mayes, *Block Copolymer Thin Films: Physics and Applications.* Annual Review of Materials Research, 2001. **31**: p. 323-355.

21. Love, J.C., et al., *Self-Assembled Monolayers of Thiolates on Metals as a Form of Nanotechnology.* Chemical Reviews, 2005. **105**(4): p. 1103-1169.

22. Pohl, K., et al., *Identifying the Forces Responsible for Self-Organization of Nanostructures at Crystal Surfaces.* Nature, 1999. **397**(6716): p. 238-241.

23. Umezawa, K., et al., *Ag/Cu(111) surface structure and metal epitaxy by impact-collision ion-scattering spectroscopy and scanning tunneling microscopy.* Physical Review B, 2000. **63**(3): p. 035402.

24. Lu, W. and Z. Suo, *Dynamics of Nanoscale Pattern Formation of an Epitaxial Monolayer.* Journal Of The Mechanics And Physics Of Solids, 2001. **49**(9): p. 1937-1950.

25. Kern, K., et al., *Long-Range Spatial Self-Organization in the Adsorbate-Induced Restructuring of Surfaces - Cu(110)-(2x1)O.* Physical Review Letters, 1991. **67**(7): p. 855-858.

26. Suo, Z. and W. Lu, *Composition Modulation and Nanophase Separation in a Binary Epilayer.* Journal of the Mechanics and Physics of Solids, 2000. **48**(2): p. 211-232.

27. Lu, W. and D. Kim, *Patterning Nanoscale Structures by Surface Chemistry.* Nano Letters, 2004. **4**(2): p. 313-316.

28. Zhu, J.Z., et al., *Coarsening Kinetics from a Variable-Mobility Cahn-Hilliard Equation: Application of a Semi-Implicit Fourier Spectral Method.* Physical Review E, 1999. **60**(4): p. 3564-3572.

29. Hu, S., et al., *On Stability of Self-Assembled Nanoscale Patterns.* Journal Of The Mechanics And Physics Of Solids, 2007. **55**(7): p. 1357-1384.

30. Langer, J.S., *DENDRITES, VISCOUS FINGERS, AND THE THEORY OF PATTERN-FORMATION.* Science, 1989. **243**(4895): p. 1150-1156.

31. Garner, A.L., et al., *Implications of a simple mathematical model to cancer cell population dynamics.* Cell Proliferation, 2006. **39**(1): p. 15-28.

32. Vicker, M.G., *Eukaryotic Cell Locomotion Depends on the Propagation of Self-Organized Reaction-diffusion Waves and Oscillations of Actin Filament Assembly.* Experimental Cell Research, 2002. **275**(1): p. 54-66.

33. Hordijk, W. and M. Steel, *Detecting autocatalytic, self-sustaining sets in chemical reaction systems.* Journal of Theoretical Biology, 2004. **227**(4): p. 451-461.

34. Billingham, J., *Dynamics of a strongly nonlocal reaction-diffusion population model.* Nonlinearity, 2004. **17**(1): p. 313-346.

35. Cross, M.C. and P.C. Hohenberg, *Pattern formation outside of equilibrium.* Reviews of Modern Physics, 1993. **65**(3): p. 851.

36. Douglas, J.F., et al., *Propagating waves of self-assembly in organosilane monolayers.* Proceedings of the National Academy of Sciences, 2007. **104**(25): p. 10324-10329.

37. Claret, J., et al., *Self-organized propagation patterns from dynamic self-assembly in monolayers.* Physical Review E, 2006. **73**(2): p. 026225.

38. Warren, C.P., et al., *Fluctuation effects in an epidemic model.* Physical Review E, 2001. **63**(5): p. 056103.

39. Riordan, J., C.R. Doering, and D. ben-Avraham, *Fluctuations and Stability of Fisher Waves.* Physical Review Letters, 1995. **75**(3): p. 565-568.

40. Cook, H., *Brownian motion in spinodal decomposition.* Acta Metallurgica, 1970. **18**(3): p. 297-306.

41. Ibach, H., *The Role of Surface Stress in Reconstruction, Epitaxial Growth and Stabilization of Mesoscopic Structures.* Surf. Sci. Rep., 1997. **29**: p. 193-263.

42. Lu, W. and D. Salac, *Patterning Multilayers of Molecules via Self-Organization.* Physical Review Letters, 2005. **94**(14): p. 146103.

43. Suo, Z. and W. Hong, *Programmable Motion and Patterning of Molecules on Solid Surfaces.* Proceedings of the National Academy of Sciences of the United States of America, 2004. **101**(21): p. 7874-7879.

44. Möhwald, H., *Phospholipid and Phospholipid-Protein Monolayers at the Air/Water Interface.* Annu. Rev. Phys. Chem., 1990. **41**: p. 441-476.

45. Chai, J. and J.M. Buriak, *Using Cylindrical Domains of Block Copolymers to Self-Assemble and Align Metallic Nanowires.* Acs Nano, 2008. **2**(3): p. 489-501.

46. Hawker, C.J. and T.P. Russell, *Block Copolymer Lithography: Merging "Bottom-Up" with "Top-Down" Processes.* MRS Bull., 2005. **30**(12): p. 952-966.

Chapter 3

Controlled Self-assembly of nanoparticles by dewetting of templated nano-scale thin film

3.1 Dewetting of nano-scale thin films

The stability of a liquid-phase film on a solid substrate is fundamental to advanced technologies of lubrication [1], adhesive [2] and coating [3, 4]. For many applications it is desirable to find out the non-dewetting conditions for a thin film to be stable, such as lithographic photoresists [5]. On the other hand, controlled dewetting [6-8] offers a spontaneous route to generate patterned nanoscale structures for various applications. For example, dewetted metallic nanoparticles can serve as the catalyst for

carbon nanotube growth [9]; dewetted patterns made from polymer thin films can be used for masks or nanoelectronic applications [10, 11]. These applications depend on a reliable prediction of the dewetting behavior and require a thorough understanding of the underlying mechanisms and competing actions.

3.1.1 Dewetting mechanisms

For a liquid phase thin film with thickness under 100nm, gravity can usually be neglected compared to surface tension. In addition, van der Waal (VDW) interaction between the liquid film surface and the substrate also becomes comparable to surface tension. Surface tension always prefers a minimum surface area such that it stabilizes any infinitesimal perturbation on the thin film surface. VDW interaction between the liquid and the substrate can be represented by a standard 6-12 Lennard-Jones potential. Upon the volume integration, the interaction potential for a certain film thickness can be expressed as $V(h) = B/h^8 - A/12\pi h^2$, where A is the Hamaker constant and B is a constant accounting for the strength of short-range repulsion. A typical curve is shown in Figure 3.1. The derivative of $V(h)$ with regard to h is so-called disjoining pressure. In this case, certain range of infinitesimal perturbation will be amplified due to the energy reduction associated to $V(h)$. This dewetting mechanism is also called spinodal dewetting [12] because its governing equation resembles the one of spinodal decomposition.

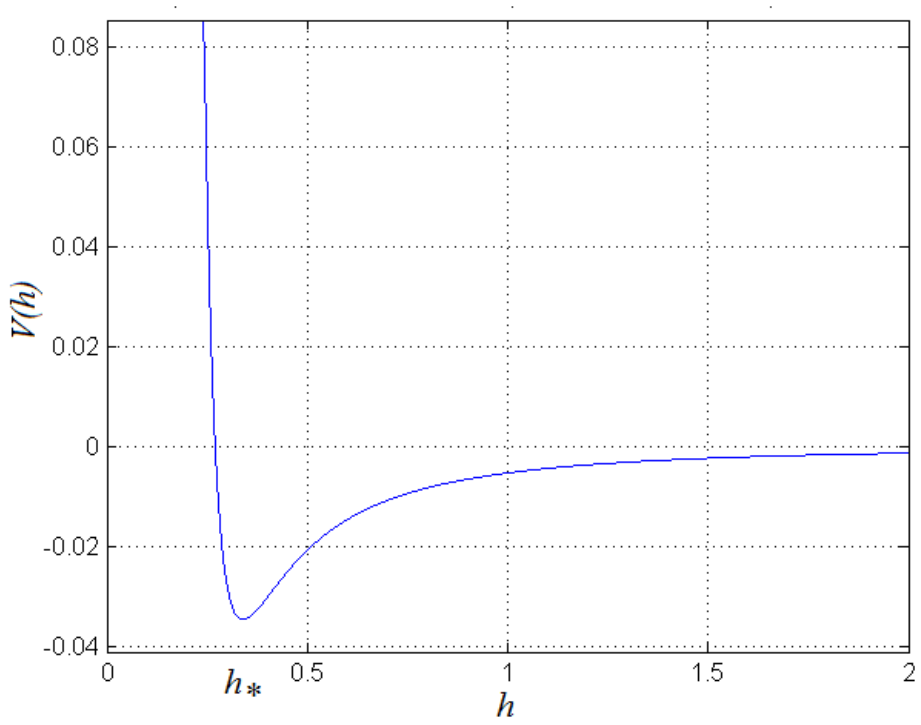

Figure 3.1 Representative potential $V(h)$ accounting for interaction energy per unit area between the thin film and the substrate

Spinodal dewetting allows the surface of thin film perturbs at its most unstable wavelength (also the fastest one). Therefore it features self-assembled nanoparticles with certain characteristic size and spacing. Besides, experiments also showed that thermal fluctuations and defects (i.e. substrate surface roughness or debris) will induce local ruptures of thin films before spinodal dewetting occurs. See Figure 3.2 for the comparisons between spinodal dewetting, thermal nucleation and heterogeneous nucleation dewetting.

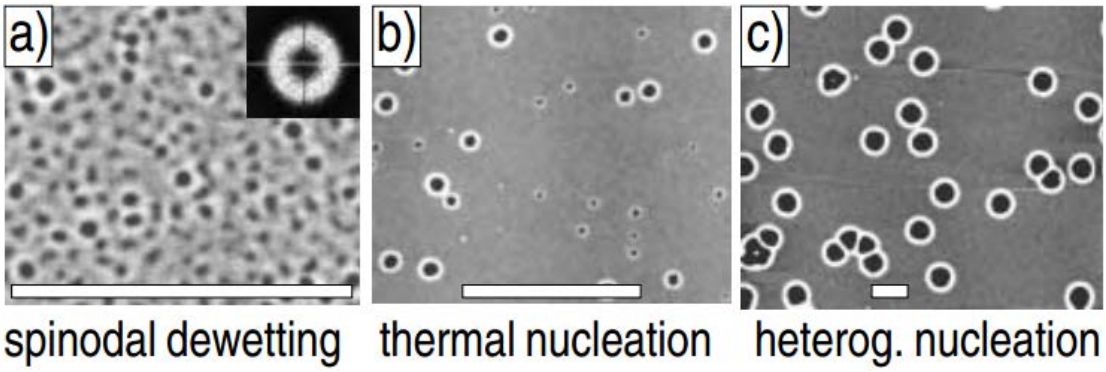

Figure 3.2 Patterns observed in spinodal dewetting, homogeneous thermal nucleation, and heterogeneous nucleation. [13]

3.1.2 Pattern formation by templated dewetting

Dewetting of nanoscale thin film provides an efficient approach to fabricate arrays of nanoparticles with similar size and spacing. However the self-assembled nanoparticles are usually only locally ordered with multiple grains presented in a large area. It is due to lack of intrinsic long-range repulsive interactions in the thin film plane. Many thin film based applications such as organic light-emitting diodes (OLED) [14] and solar cells [4, 15] require arrays of oriented nanoparticles with long-range order. Recent experiments have shown that the dewetting process can be guided by the "top-down" templating methods[6, 8, 16].

Generally speaking, there are two major templated dewetting approaches: (1) heterogeneous substrates and (2) pre-patterned thin film. In heterogeneous substrate method, we modify the physical topology or chemical compositions of the substrates with desired patterns. The initial liquid-air interface is kept flat such that the VDW interaction

has a position dependent potential. Thus the pattern information from the templating substrate can be used to guide the nucleation sites of dewetting [17, 18]. In pre-patterned thin film method, we template the liquid-air interface instead [19]. The surface of thin film is often templated by nano-imprinting or templated deposition/etching. Additional temperature control is needed for solidification and melting processes.

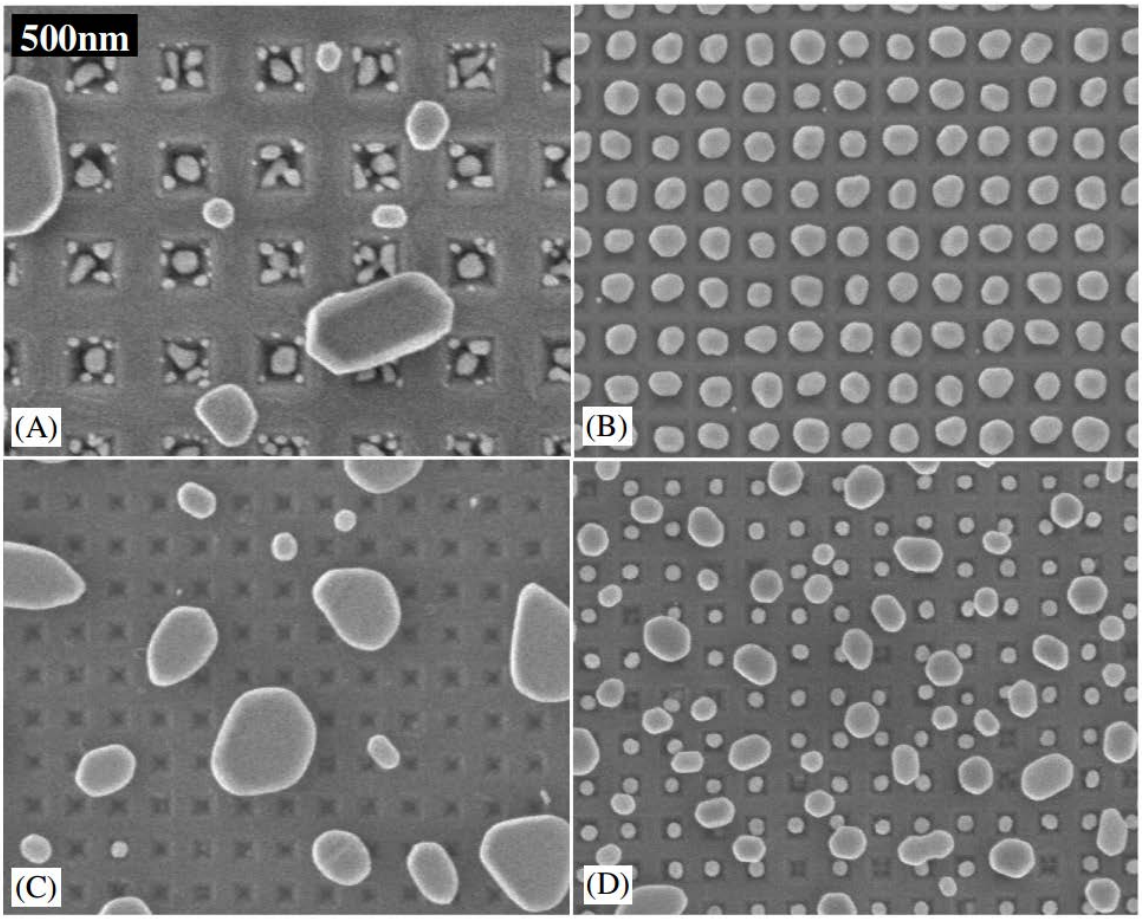

Figure 3.3 Dewetting of metalic thin film on patterned substrates (A) Multiple particles form per pit with no ordering, 377 nm period substrate topography with 16nm thick film. (B) Ordered arrays of one particle per pit with no extraneous particles, 175 nm period narrow-mesa substrate with 21 nm thick film. (C) Film not interacting with topography, 175 nm period wide-mesa substrate with 21 nm thick film. (D) Ordered arrays of one particle per pit with particles on mesas, 175 nm period wide-mesa substrate with 16nm thick film [18]

3.2 Self-assembly of ordered carbon nanotube catalyst by dewetting of Fe thin film on Anodic Aluminum Oxide substrate

3.2.1 Experiment results

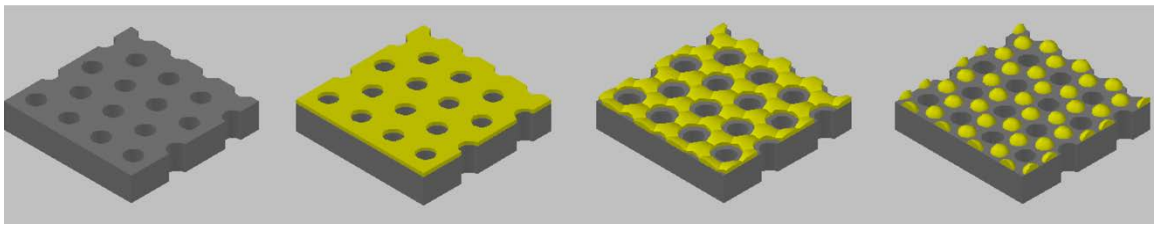

Figure 3.4 Schematic of Fe thin film dewetting on AAO substrate (courtesy of Dr. Eric Meshot)

Carbon nanotube catalysts are commonly nanoparticles of metals such as nickel, cobalt or iron. The nanoparticles can be produced by annealing or plasma etching of a metallic thin film. Recent experiments conducted by Eric Meshot [20] showed that anodic aluminum oxide (AAO) membranes, which have uniform nanoscale pore size and spacing with hexagonal arrangement, can influence the dewetting of iron thin films into organized arrays of nanoparticles. Specifically, as shown in the Figure 3.4, the iron thin films were first sputtered on the commercially purchased AAO membranes (Synkera, Inc.). Then the films were annealed in H_2/He for 10 minutes under 775ºC. Compared to nanoparticles annealed on flat Si surface (Figure 3.5 (e)), the existence of AAO membrane improved short-range order of catalyst nanoparticles (Figure 3.5 (b-d)). The inset FFT images confirmed the 6-fold symmetry in the samples with AAO templates.

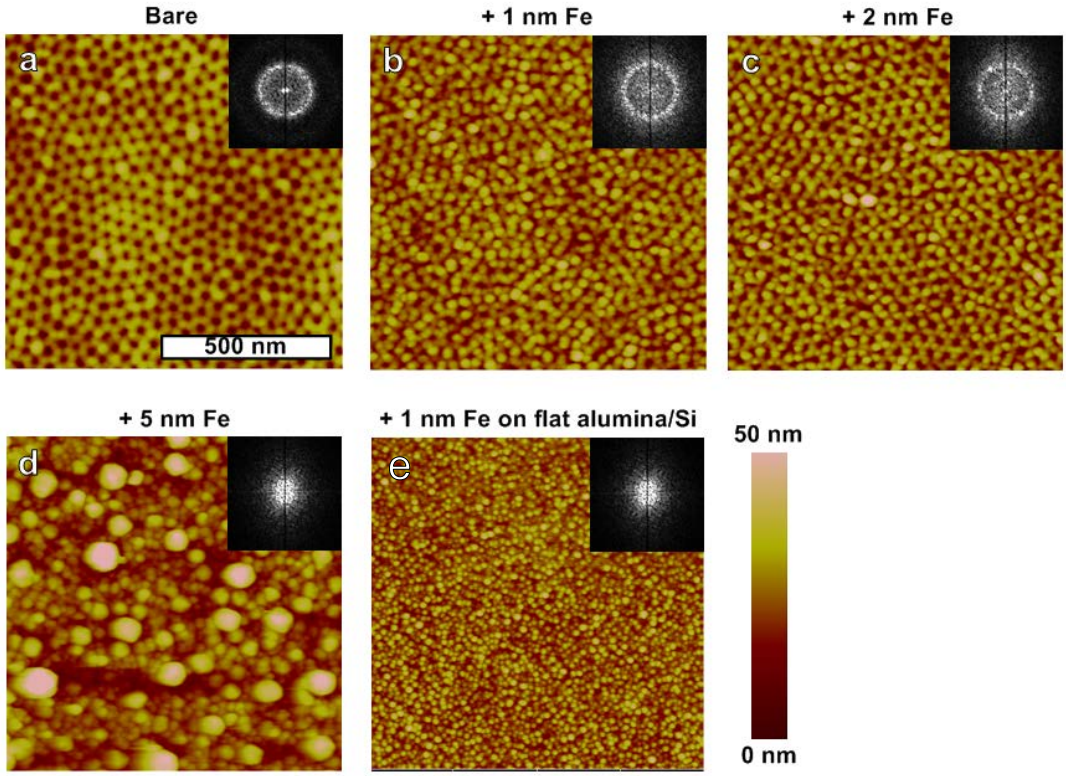

Figure 3.5 AFM images of (a) bare AAO, annealed surface after (b) 1nm Fe deposition (c) 2nm Fe deposition (d) 5nm Fe deposition and (e) 1nm Fe deposition on flat alumina/Si surface; insets are FFT of the AFM images. [20] (courtesy of Dr. Eric Meshot)

3.2.2 Modeling and numerical procedures

We consider a representative dewetting system: a liquid thin film on a substrate surface. The free energy of the system, *G*, involves the surface energy of the film and the van der Waal (VDW) interaction between the liquid film surface and the substrate [21]. The expression is given by

$$G = \iint [\frac{\gamma}{2}(\nabla h)^2 + V(h)]dA \tag{3.1}$$

where *h* denotes the height of the thin film. The area integration extends over the substrate surface. The first term accounts for the surface energy, which is related to the surface tension of the film, γ. This term prefers a flat surface and thus stabilizes the thin film. The second term stands for the VDW interaction, where $V(h) = B/h^8 - A/12\pi h^2$. Here *A* is the Hamaker constant and *B* is a constant accounting for the strength of short-range repulsion. When *A*>0, the free energy decreases if the thin film thickness *h* is reduced. Note that the contact angle α between the thin film and the substrate can be determined from A and γ [22], namely $\alpha = arc\cos(1 - A/16\pi\gamma h_*^2)$. h_* is the equilibrium thickness of the thin film, which essentially represents the substrate surface when $dV(h_*)/dh = 0$. Combining Eq. (3.1) with lubrication approximation of the Navier-Stokes equation [23] gives the governing equation for film thickness evolution, namely $\partial h/\partial t = \nabla \cdot (M(h)\nabla p)/\eta$. Here η is the viscosity, $M(h) = h^3/3$ is the mobility factor and $p = -\gamma\nabla^2 h + dV/dh$. Normalizing the length by initial film thickness h_0 and time by $t_0 = \eta h_0/\gamma$, we have the following normalized equation

$$\partial h / \partial t = \nabla \cdot (m(h) \nabla p) \tag{3.2}$$

where $p = (-\nabla^2 h - 8B_0 / h^9 + A_0 / 6\pi h^3)$, and $B_0 = B / \gamma h_0^8$, $A_0 = A / \gamma h_0^2$ and $m(h) = h^3 / 3h_0^3$

To conduct the numerical simulation, we consider Eq. (3.2) in Fourier space,

$$\partial \hat{h} / \partial t = i\mathbf{k} \cdot \{\hat{m}(i\mathbf{k}\hat{p})_r\}_k \tag{3.3}$$

where the hat and subscript 'k' denote Fourier transform, 'r' denotes inverse Fourier transform, and $\mathbf{k}$ is the wave number vector. $\hat{p} = k^2 + (-8B_0 / h^9 + A_0 / 6\pi h^3)_k$. The second term is a nonlinear function of *h*, so $\hat{p}$ is calculated by numerical Fourier transform. To enhance numerical stability, we applied a semi-implicit method in our simulation for time integration. Specifically, we added a linear term, $\nabla^4 C$, to both sides so that Eq. (3.3) became $\partial \hat{h} / \partial t + k^4 \hat{h} = i\mathbf{k} \cdot \{\hat{m}(i\mathbf{k}\hat{p})_r\}_k + k^4 \hat{h}$. The $k^4 \hat{h}$ tem on the left side is evaluated at time (*n*+1) and the term on the right side is evaluated at time *n*. Denote the time step by Δt and replace $\partial \hat{h} / \partial t$ by $(\hat{h}^{(n+1)} - \hat{h}^{(n)}) / \Delta t$. The algorithm for *n*+1 time is given by $(1 + k^4 \Delta t)\hat{h}^{(n+1)} = (1 + k^4 \Delta t)\hat{h}^{(n)} + \Delta t \; i\mathbf{k} \cdot \{\hat{m}(i\mathbf{k}\hat{p})_r\}_k^{(n)}$. This semi-implicit approach significantly alleviated the time step constraint.

3.2.3 Simulation results and discussions

Dynamic evolution of dewetting process

Based on the model and the numerical schemes discussed in the last section, a series of simulations were conducted to study the dynamics of the template wetting. As shown in Figure 3.6(a), a flat thin film was first deposited on the AAO. The film kept the same pore locations and sizes as its AAO template. Assuming that the pores in AAO are deep and no mass can flow into them, the mobility term $M(h)$ is set to be 0 all the time within the pore regions. Mass can only flow in the rest of the region with the mobility $M(h) = h^3 / 3$, where h is the thickness of the film.

The first stage of dewetting accompanies the pore expanding as shown in Figure 3.6 (b). During this stage, the majority of the energy reduction occurs at the contact line between the film and the substrate. Meanwhile the extra mass due to retraction accumulates at the rims of the pores, forming the so-call capillary ridges. During the second stage, the pores continue to expand while those capillary ridges from neighboring pores start to join together. This stage ends up with a honeycomb-like liquid network. During the third stage, the ridges of the network break up and nanoparticles start to emerge at the junction sites (Figure 3.6 (c)). The fourth stage features the coarsening process. Those emerging nanoparticles which are close to each other and still connected to each other by a thin film may eventually coarsen into one larger particle. These nanoparticles with twice volume of others often sit in half way between the two expected lattice sites, which eventually degrade the order. As shown in Figure 3.6 (d), those coarsened particles are pointed by the red arrows.

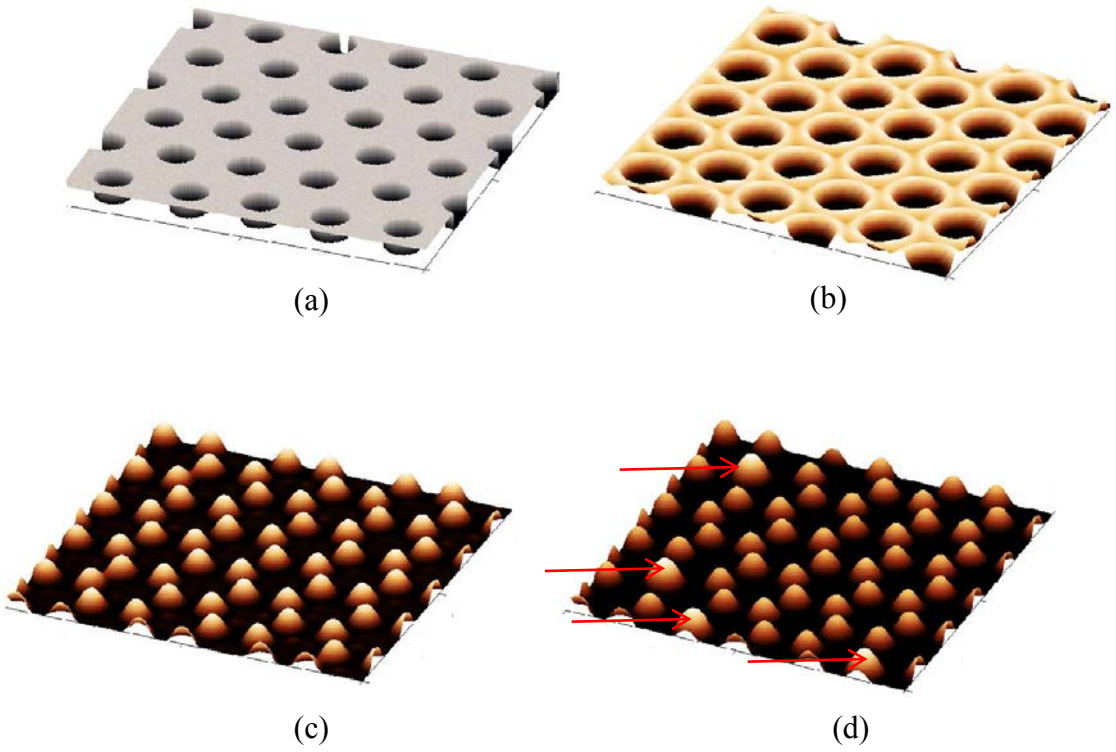

Figure 3.6 Simulation results of the templated dewetting process on AAO at different stages.

Order parameter

As the catalyst of CNT growth, nicely ordered and mono-dispersed nanoparticles are preferred. The size distribution of the nanoparticles is straightforward to present. So we only need to find a proper way to assess the order quality of the generated nanoparticle arrays. Here we adopted an order parameter which is often used in highly ordered atomic surface structures. The expression is,

$$Q = \frac{1}{3N}\sum_{i=1}^{N}[\cos\frac{4\pi x_i}{\sqrt{3}\lambda_0} + \cos\frac{4\pi}{\sqrt{3}\lambda_0}(-\frac{x_i}{2} + \frac{\sqrt{3}y_i}{2}) + \cos\frac{4\pi}{\sqrt{3}\lambda_0}(-\frac{x_i}{2} - \frac{\sqrt{3}y_i}{2})] \quad (3.4)$$

where N is the total number of the particle, λ_0 is the lattice parameter and (x_i, y_i) are the coordinates of each particle.

There are two implicit variables and one explicit variable λ_0 in the Eq. (3.4), which will influence the value of order parameter. Recall that the actual values of any coordinates depend on the choice of the coordinate system. The two implicit variables are the origin (x_0, y_0) and the orientation θ of the coordinate system. Here we are looking for a best fit between the image and an unknown perfect lattice, therefore we are actually looking for a "maximized" order parameter Q_{max} in a space that consists of λ_0, θ and (x_0, y_0). Specifically, we scan θ from 0 to 60^o, λ_0 from $0.5\lambda_a$ to $1.5\lambda_a$ and (x_0, y_0) among all particle locations to find a maximum Q. (λ_a is the average particle spacing extracted from the sample)

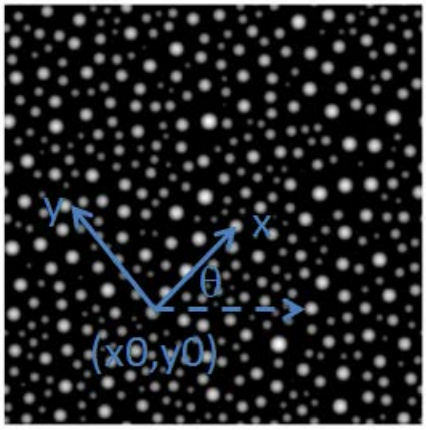

Figure 3.7 Parameters used in order parameter calculation

Effect of initial thickness, pore position variations and size variations

We first evaluated the effects of pore position variations on the order parameter of AAO templates. An AAO membrane with in perfect hexagonal lattice would have the order parameter of 1. It would be worthwhile to assess the order parameter dependence on the position variations from perfect lattice locations. We assume the pore position variations are in normal distribution with different standard deviations. The result in Figure 3.8 shows a roughly linear relation between pore position variation and order parameter which makes the order parameter a good order indicator. The order parameter of a typical AAO sample was evaluated in a 1μm by 1μm region. The low order parameter of about 0.11 is due to the existence of multiple grains in this region. The local order parameter in the lower-right quarter gave us 0.35 which corresponds to ~10% pore position variation. The number is consistent with the AAO sample specification.

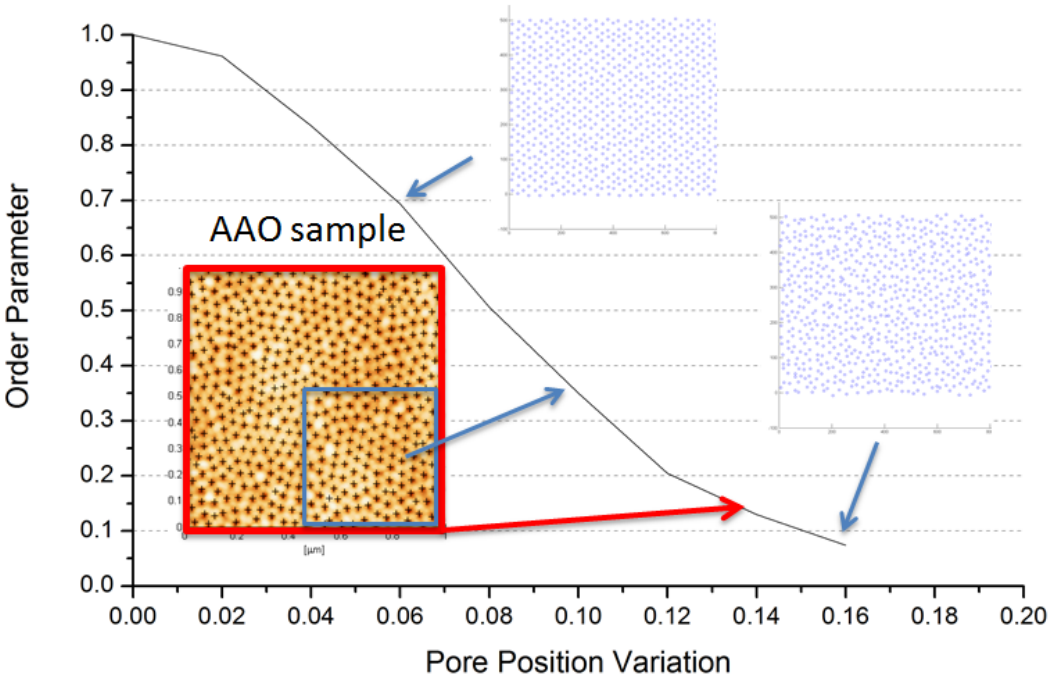

Figure 3.8 Order parameter dependence on the pore position variations.

Then we conducted a series of simulations to evaluate the effects of AAO pore position variations on the order parameter of self-assembled nanoparticles. We designed the following AAO templates for the simulations. Based on a perfect AAO template which has an average pore diameter of 25, and pore spacing of 50, we added position variations which have normal distribution with different standard deviations. The standard deviations increase from 0% of the pore spacing up to 16% with 2% interval. In addition, three different initial thicknesses of thin film were considered. The results are shown in the Figure 3.9.

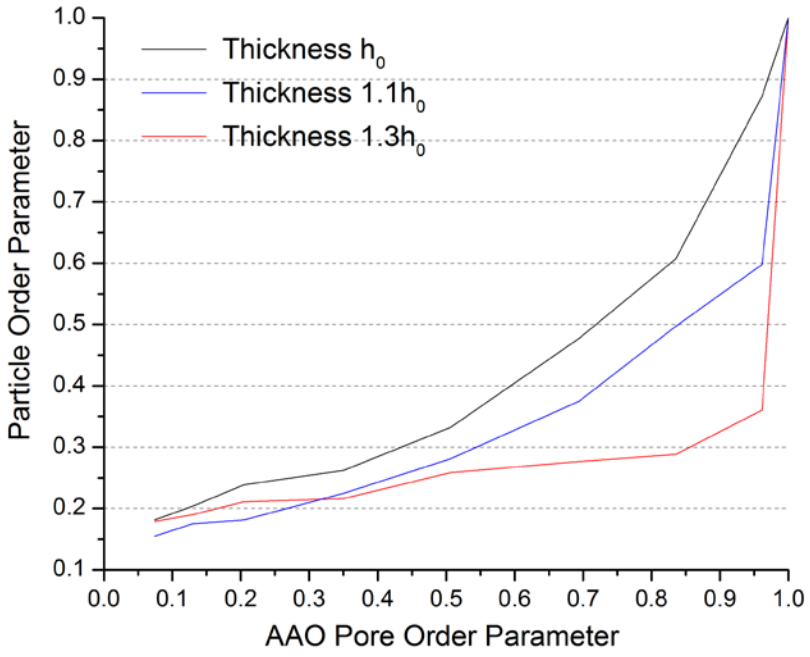

Figure 3.9 Particle order parameter dependence on the AAO pore order parameters.

When the AAO template is perfect, we also obtain the nanoparticles in perfect order. For all three thicknesses, the particle order parameters show similar nonlinear dependence on the AAO pore order parameter. The particle order begins with a sharp drop when the AAO order degrades by 5-10%. Then the drop slows down and all three curves converge around particle order around 0.2.

From the results, we can see that the film with initial thickness h_0 has the best overall order. From a simple linear stability analysis, we can derive the relation between the fastest growth wavelength and the initial film thickness, i.e. $\lambda_f = 2\sqrt{2}\pi / \sqrt{-V''(h_i)}$. $V(h)$ is the VDW interaction between liquid and solid interfaces, which is given in the last section. For thickness from 0.5 to 1.5, the results are shown in Figure 3.10. When h_i is 1.0, 1.1 and 1.3, the corresponding wavelengths are about 20, 22 and 25.

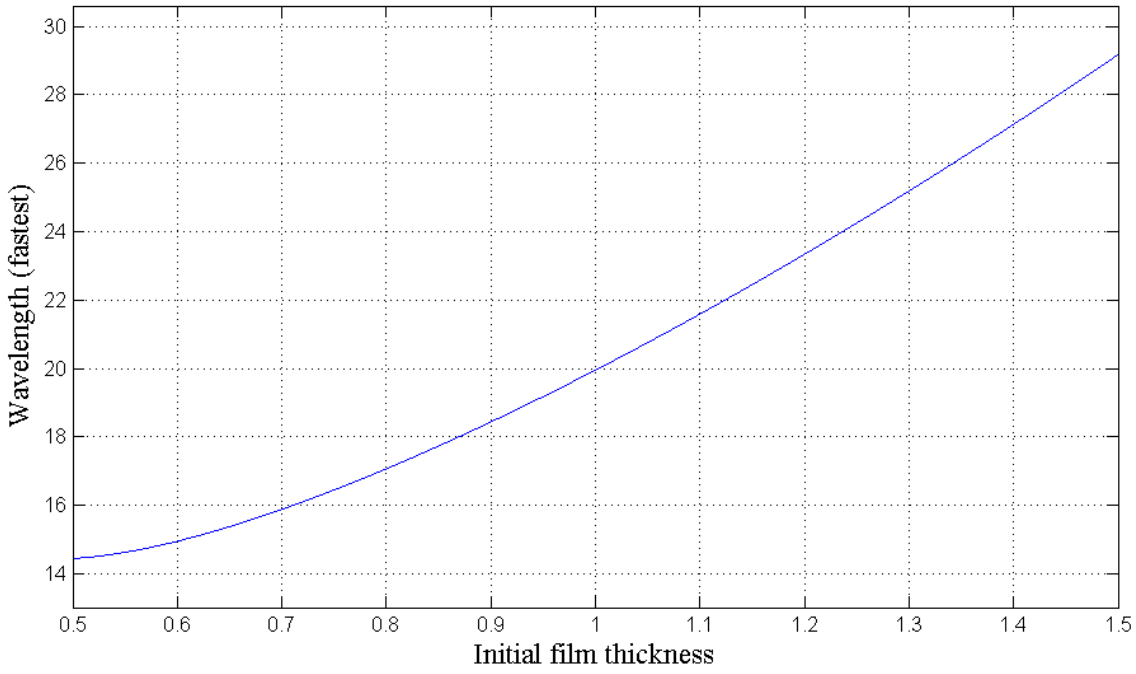

Figure 3.10 Fastest growth wavelength and initial film thickness relation

Given that the average pore spacing is D, we may estimate the particle spacing as which is $D/\sqrt{3}$ (see Figure 3.11). Imagine that the fastest wavelength is greater than $D/\sqrt{3}$, the space between neighboring blue dots cannot hold two particles. Instead, coarsening is likely to occur. Therefore a general guidance for the wavelength (or initial film thickness) would be $\lambda_f < D/\sqrt{3}$. In our case, D=50 and $50/\sqrt{3} \approx 28.9$. For the three thicknesses we have in Figure 3.9, h_i =1.3 has the largest λ_f which is closest to the critical distance 28.9. Therefore it has the highest chance to have coarsening if more and more pore position variations are involved. More coarsening means worse order which is consistent with the simulation results.

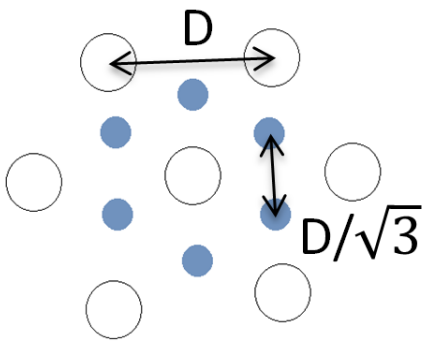

Figure 3.11 The ideal positions for nanoparticles and the spacing relation. (blue dots stand for nanoparticles and the black circles stand for pores)

Next we evaluate the effects of AAO pore size variations on the order parameter of self-assembled nanoparticles. Based on the same perfect AAO template as above, we added size variations which have normal distribution with different standard deviations. The standard deviations increase from 0% of the pore spacing up to 20% with 4% interval and same three thicknesses are considered.

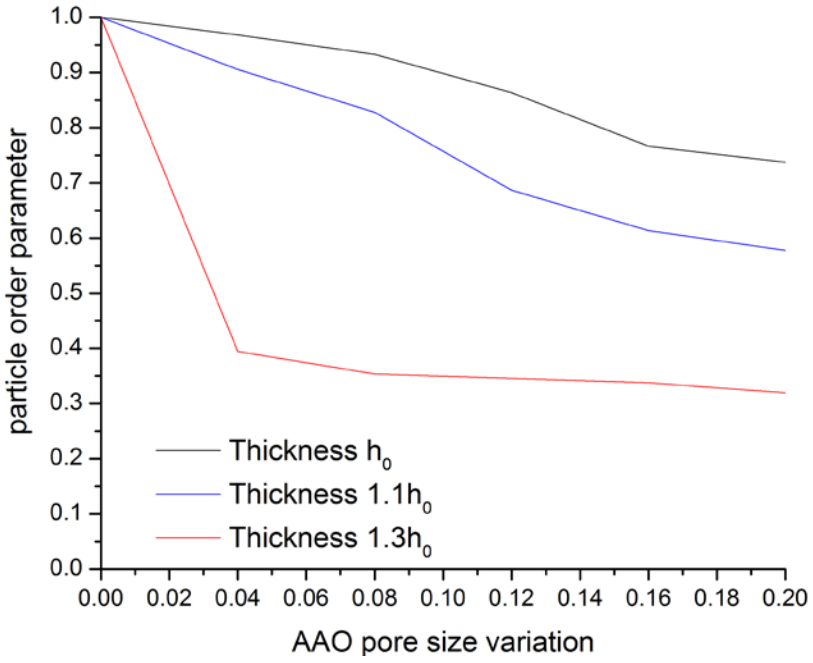

Figure 3.12 Particle order parameter dependence on the AAO pore size variation

The results in Figure 3.12 show that the thickness h=1.0 still has best overall order parameter which is expected. Besides the order parameters also show less dependence on the size variations than position variations. From the simulation results (Figure 3.13), we observed that the pore size distributions vary over the different dewetting stages. For the early stage of dwetting, Brochard-Wyart et al. showed the pore expanding rate as $R \sim t^{2/3}$ [24], which means that the ratio of different pore sizes does not change after a same time period. It is confirmed by the simulations (the 2nd row in the Figure 3.13), where the pore size has similar variation as the initial condition. In this stage, pores expand on their own. However, during the third stage when the networks of liquid ridges are forming, the pore size differences are getting smaller (the 3rd row in the Figure 3.13). It is because that the pore size differences in the honeycomb network cause the surface energy density difference across the surface. The system of the liquid network

seeks minimum energy by reducing the pore size differences. Eventually, this reduction on the pore size differences makes the final order parameter difference less distinguishable.

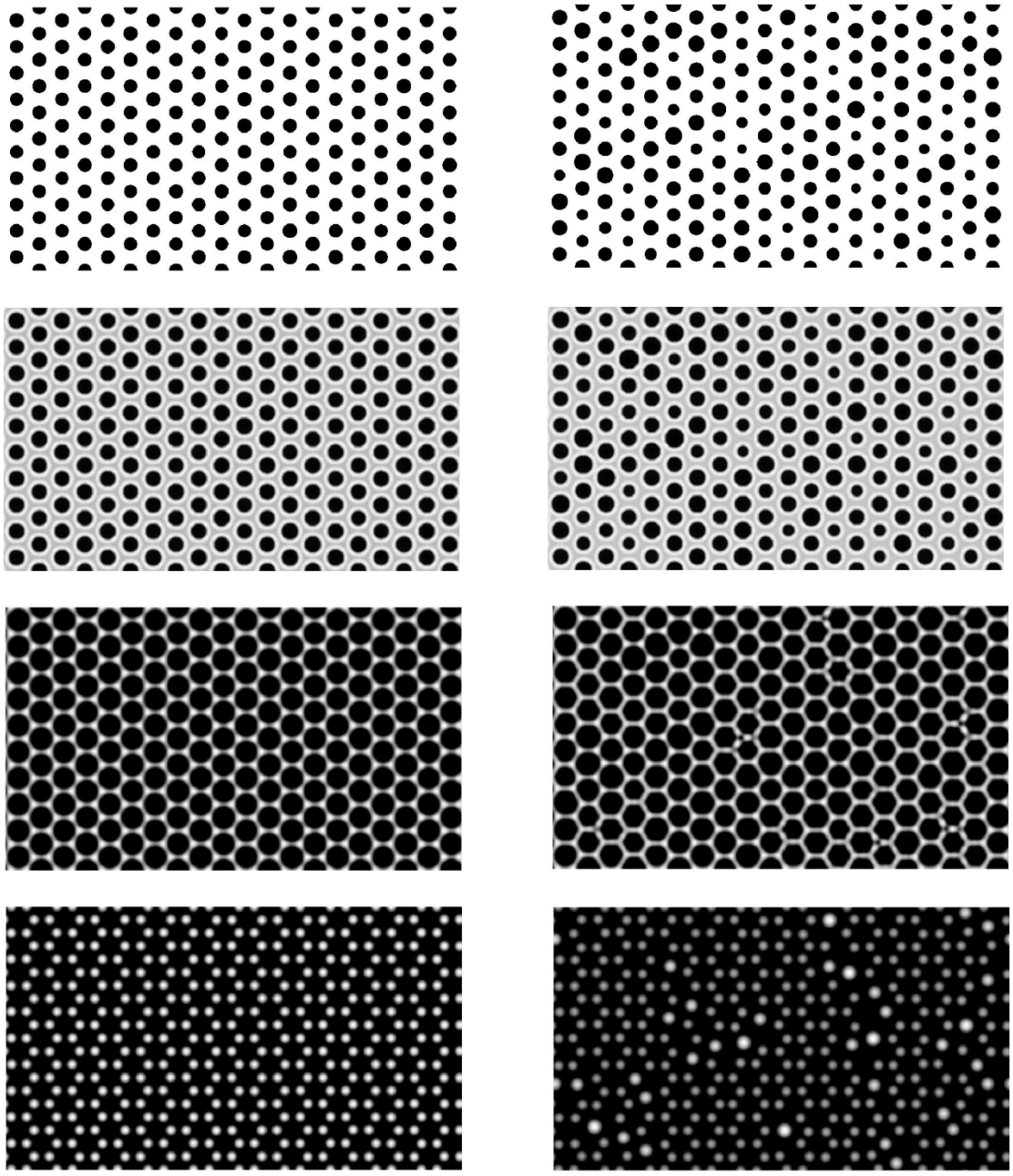

Figure 3.13 Time evolution of templated thin film dewetting on AAO (a) initial pore size variation 4% (b) initial pore size variation 16%

Nanoparticle size distribution and coarsening

Recall that the order parameter does not include the information in particle size distribution. We may also be interested in the size distribution of the self-assembled nanoparticles. And are there any correlations between the nanoparticle order parameters and the corresponding size distributions? The results are shown in the Figure 3.12. The histograms below the simulation result images represent their particle size distribution. For AAO order around 0.95 (Figure 3.12 (b) (d)), we can observe that the center of the particle size distribution shifts from 1.5 to 2 when the thickness increases from 1 to 1.3. Additional peaks are around 2.2-2.5. The shift clearly confirms the coarsening between two or above particles which degrades the order. On the other hand, if we compare the two cases with same thickness (i.e. Figure 3.12 (b) to (a) and (d) to (c)), the size distribution is mostly widened which is different from the size shift from (b) (d). Meanwhile the change in order parameter is relatively less for thickness 1.3. These observations may suggest two different coarsening mechanisms happening during dewetting.

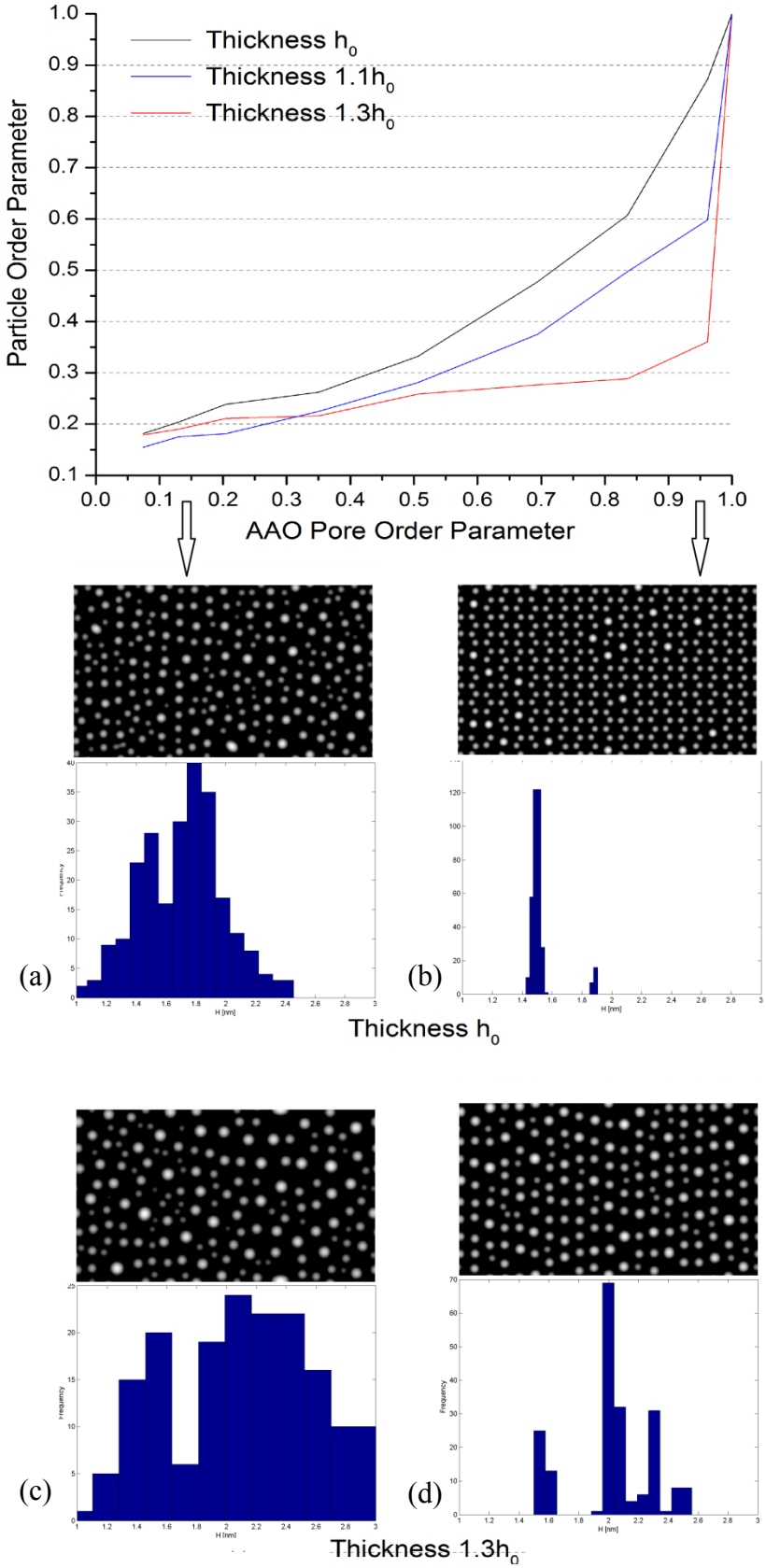

Figure 3.14 Correlation between particle order parameter and size distribution

A closer examination on the particle cross-section profile evolution gives us more insights about the coarsening. A few snapshots are extracted from different stages of dewetting for the case in Figure 3.14 (b). In this coarsening mode, two neighboring particles have the similar size and merges in the middle. Therefore this kind of coarsening doubles the size of the particle and also degrades the order in the meantime.

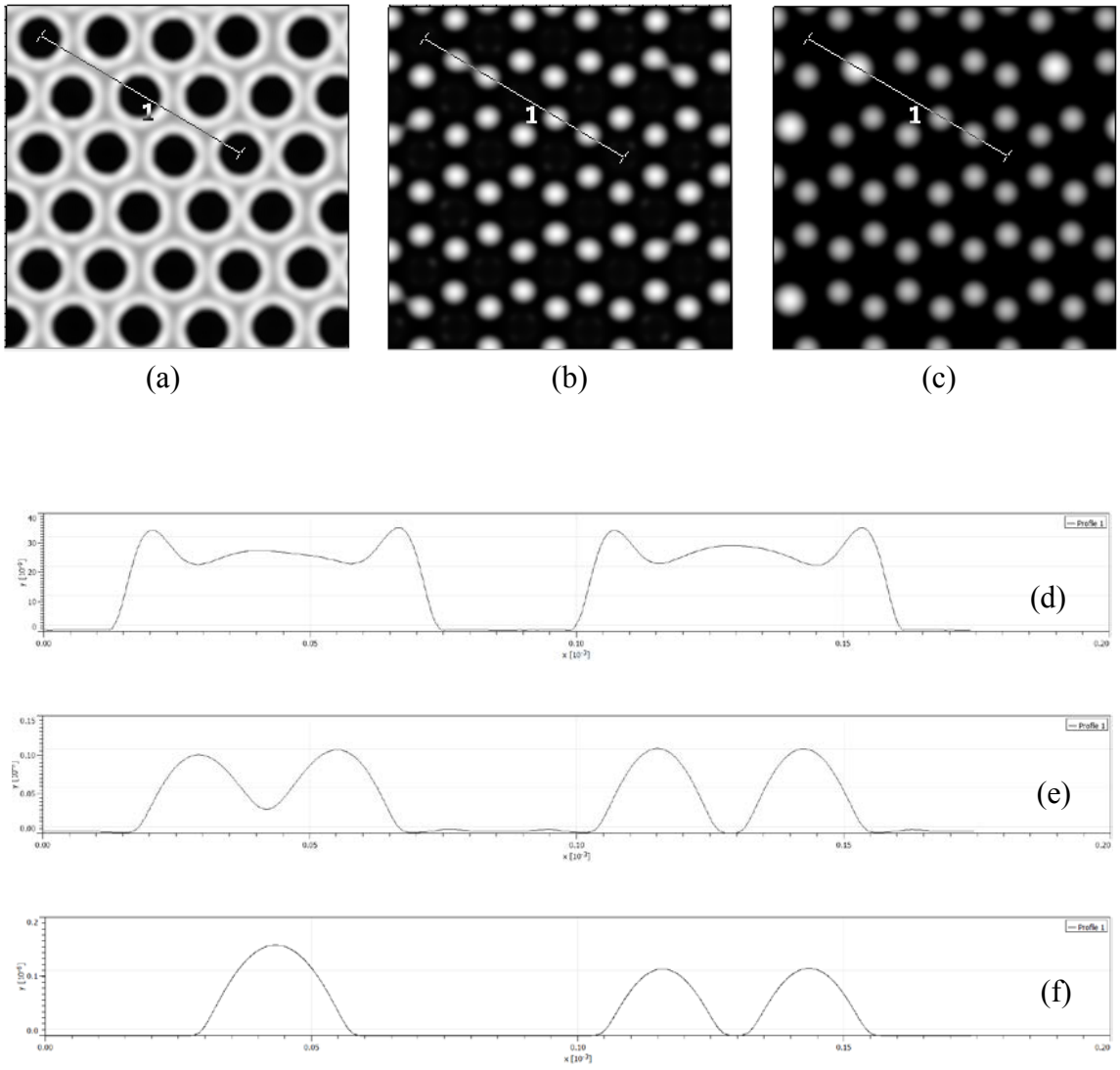

Figure 3.15 Coarsening dynamics of neighboring particles via merging at the middle

We took a few snapshots that are extracted from different stages of dewetting for the case in Figure 3.14 (c). In this case, coarsening occurs when the neighboring particles have different sizes. The bigger one grows at the expense of smaller one, which is known as Ostwald ripening. Therefore this kind of coarsening doubles the size of the particle while not degrades the order. Note that all the snapshots in Figure 3.14 are at the same time stage.

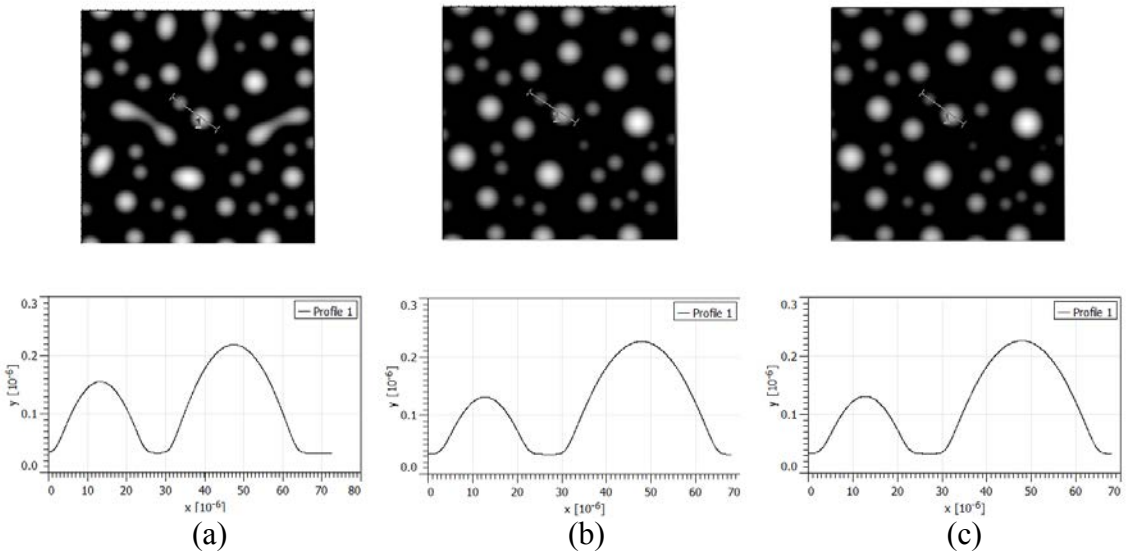

Figure 3.16 Coarsening dynamics of neighboring particles via Ostwald ripening

In conclusion, the merging coarsening mechanism dominates the situation when the AAO template has relatively good order. It degrades the order while keep the particle size relatively monodispersed. In comparison, the Ostwald ripening mechanism dominates the situation when the AAO template has relatively bad order. It widens the particle size distribution while keep the order parameter relatively good.

3.3 References

1. Luo, J., S. Wen, and P. Huang, *Thin film lubrication. Part I. Study on the transition between EHL and thin film lubrication using a relative optical interference intensity technique.* Wear, 1996. **194**(1–2): p. 107-115.

2. Pashley, E.L., et al., *Effects of one versus two applications of an unfilled, all-in-one adhesive on dentine bonding.* Journal of Dentistry, 2002. **30**(2–3): p. 83-90.

3. Niklaus, F., et al., *Adhesive wafer bonding.* Journal of Applied Physics, 2006. **99**(3): p. 031101.

4. Krebs, F.C., *Fabrication and processing of polymer solar cells: A review of printing and coating techniques.* Solar Energy Materials and Solar Cells, 2009. **93**(4): p. 394-412.

5. Lee, L.L., C.D. Schaper, and W.K. Ho, *Real-time predictive control of photoresist film thickness uniformity.* Ieee Transactions on Semiconductor Manufacturing, 2002. **15**(1): p. 51-59.

6. Mukherjee, R., D. Bandyopadhyay, and A. Sharma, *Control of morphology in pattern directed dewetting of thin polymer films.* Soft Matter, 2008. **4**(10): p. 2086-2097.

7. Verma, R., et al., *Electric Field Induced Instability and Pattern Formation in Thin Liquid Films.* Langmuir, 2005. **21**(8): p. 3710-3721.

8. Seemann, R., S. Herminghaus, and K. Jacobs, *Gaining control of pattern formation of dewetting liquid films.* Journal of Physics-Condensed Matter, 2001. **13**(21): p. 4925-4938.

9. Guan, Y.F., et al., *Non-lithographic organization of nickel catalyst for carbon nanofiber synthesis on laser-induced periodic surface structures.* Nanotechnology, 2007. **18**(33): p. 335306.

10. Wang, J.Z., et al., *Polymer field effect transistors fabricated by dewetting.* Synthetic Metals, 2004. **146**(3): p. 287-290.

11. Benor, A., et al., *Microcontact printing and selective surface dewetting for large area electronic applications.* Thin Solid Films, 2007. **515**(19): p. 7679-7682.

12. Xie, R., et al., *Spinodal Dewetting of Thin Polymer Films.* Physical Review Letters, 1998. **81**(6): p. 1251-1254.

13. Seemann, R., S. Herminghaus, and K. Jacobs, *Dewetting Patterns and Molecular Forces: A Reconciliation.* Physical Review Letters, 2001. **86**(24): p. 5534-5537.

14. Fukushi, Y., et al., *Effect of ITO surface state to the aging characteristics of thin film OLED.* Applied Surface Science, 2005. **244**(1–4): p. 537-540.

15. Aberle, A.G., *Thin-film solar cells.* Thin Solid Films, 2009. **517**(17): p. 4706-4710.

16. Kondic, L., et al., *Nanoparticle assembly via the dewetting of patterned thin metal lines: Understanding the instability mechanisms.* Physical Review E, 2009. **79**(2): p. 026302.

17. Kargupta, K., R. Konnur, and A. Sharma, *Spontaneous Dewetting and Ordered Patterns in Evaporating Thin Liquid Films on Homogeneous and Heterogeneous Substrates.* Langmuir, 2001. **17**(4): p. 1294-1305.

18. Giermann, A.L., C.V. Thompson, and H.I. Smith, *Templated formation of ordered metallic nano-particle arrays*, in *Nanoparticles and Nanowire Building Blocks-Synthesis, Processing, Characterization and Theory*, O.J. Glembocki and C.E. Hunt, Editors. 2004, Materials Research Society: Warrendale. p. 37-42.

19. Xue, L. and Y. Han, *Pattern formation by dewetting of polymer thin film.* Progress in Polymer Science, 2011. **36**(2): p. 269-293.

20. Meshot, E., Z.Z. Zhao, W. Lu, A.J. Hart *Controlled ordering of small-diameter metal nanoparticles by dewetting on hexagonal mesh templates.* 2012.

21. Becker, J., et al., *Complex dewetting scenarios captured by thin-film models.* Nat Mater, 2003. **2**(1): p. 59-63.

22. Diez, J.A. and L. Kondic, *On the breakup of fluid films of finite and infinite extent.* Physics of Fluids, 2007. **19**(7): p. 072107.

23. Oron, A., S.H. Davis, and S.G. Bankoff, *Long-scale evolution of thin liquid films.* Reviews of Modern Physics, 1997. **69**(3): p. 931-980.

24. Brochard-Wyart, F., et al., *Wetting and Slippage of Polymer Melts on Semi-ideal Surfaces.* Langmuir, 1994. **10**(5): p. 1566-1572.

Chapter 4

Self-assembled 3-D microstructures by elastocapillary densification of carbon nanotube (CNT) forests

4.1 Introduction

Self-assembly of filaments, ranging from actin to silk [1, 2], is ubiquitous in nature. Biological filaments typically grow and assemble in a liquid environment, where capillary action plays a significant role. The arrangement and coupling of filaments determines their collective mechanical properties, and how forces are communicated through filament assemblies. Further, synthetic mimics of biological filaments, both in shape and chemistry, are widely sought for practical applications including smart surfaces,

microelectronic interconnects, and electrode-cell interfaces [3, 4]. However, while capillary forces have been shown to assemble synthetic nanostructures including nanoparticles [5], nanorods [6], micro pillars [7] and even wet hair [8], the formed structures are generally symmetric or uniform, showing a simple agglomeration of the components.

Carbon nanotubes (CNT) were chosen as an example system due to their outstanding mechanical, electrical, thermal, and chemical properties [9], along with the ability to fabricate patterns of vertically aligned CNTs [10] as starting templates for self-assembly experiments. Chemical vapor deposition growth of CNTs enables efficient production of vertical CNT forest microstructures having straight sidewalls and high aspect ratios, with dimensions ranging from micrometers to millimeters [11]. Despite the exceptional properties of individual CNTs, the bulk properties of CNT forests are typically poor due to the low density of CNT growth, rendering them inadequate for most applications.

Recently an innovative approach, called capillary forming [12], was developed to assemble complex 3D microstructures from aligned CNT forest by Prof. John Hart's group. The method utilizes the attractive capillary interaction between CNTs which are wetted by liquid such as acetone. Specifically, the CNT forest is first patterned by catalyst shape which is created by photolithography. The acetone is supplied from the condensation of acetone vapor onto the silicon substrate, and then drawn into the individual CNT structures by capillary action. Thus, the attractive capillary forces bring the CNT together, leading to the densification of the structures (Figure 4.1). The densification significantly increases the mechanical robustness and bulk properties.

Meanwhile, due to the adhesion of CNTs with the catalyst on the substrate, the movements of lower CNTs are constrained. The individual CNTs bend accordingly to accommodate both the densification and the constraint on the substrate. By designing the catalyst shape, an intriguing bending behavior was observed for semi-circular CNT forests. Furthermore, twisting, re-entrant and many other complex 3D microstructures (Figure 4.2) were also fabricated through the capillary forming method.

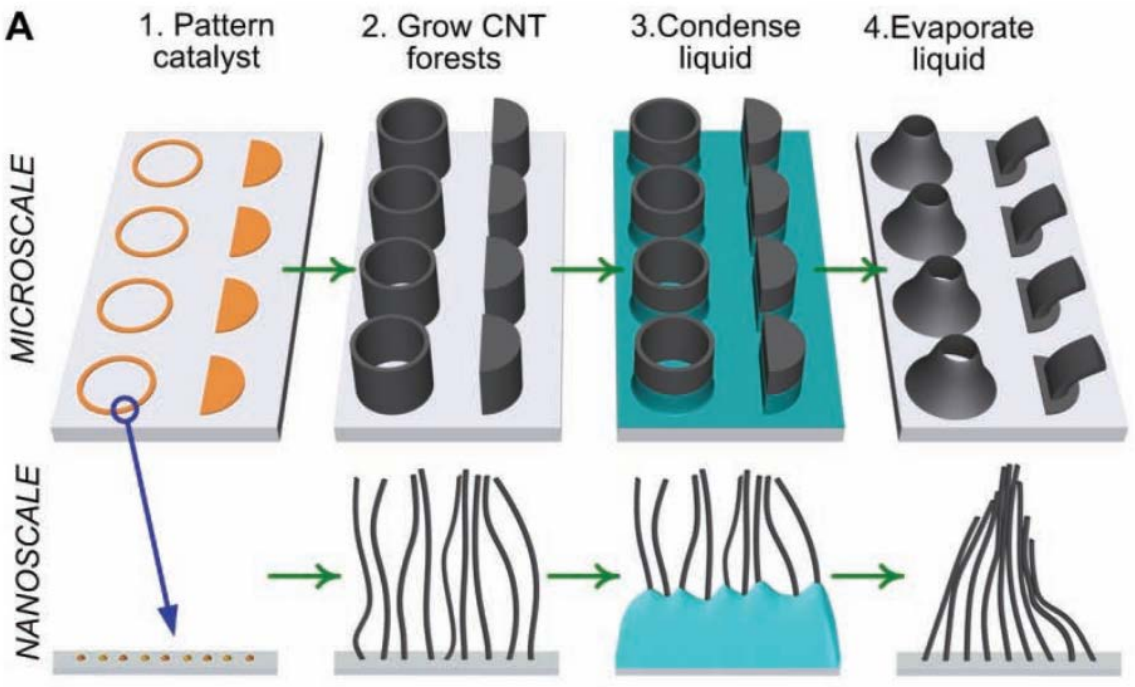

Figure 4.1 Schematic of CNT forest growth and capillary forming sequence [12]

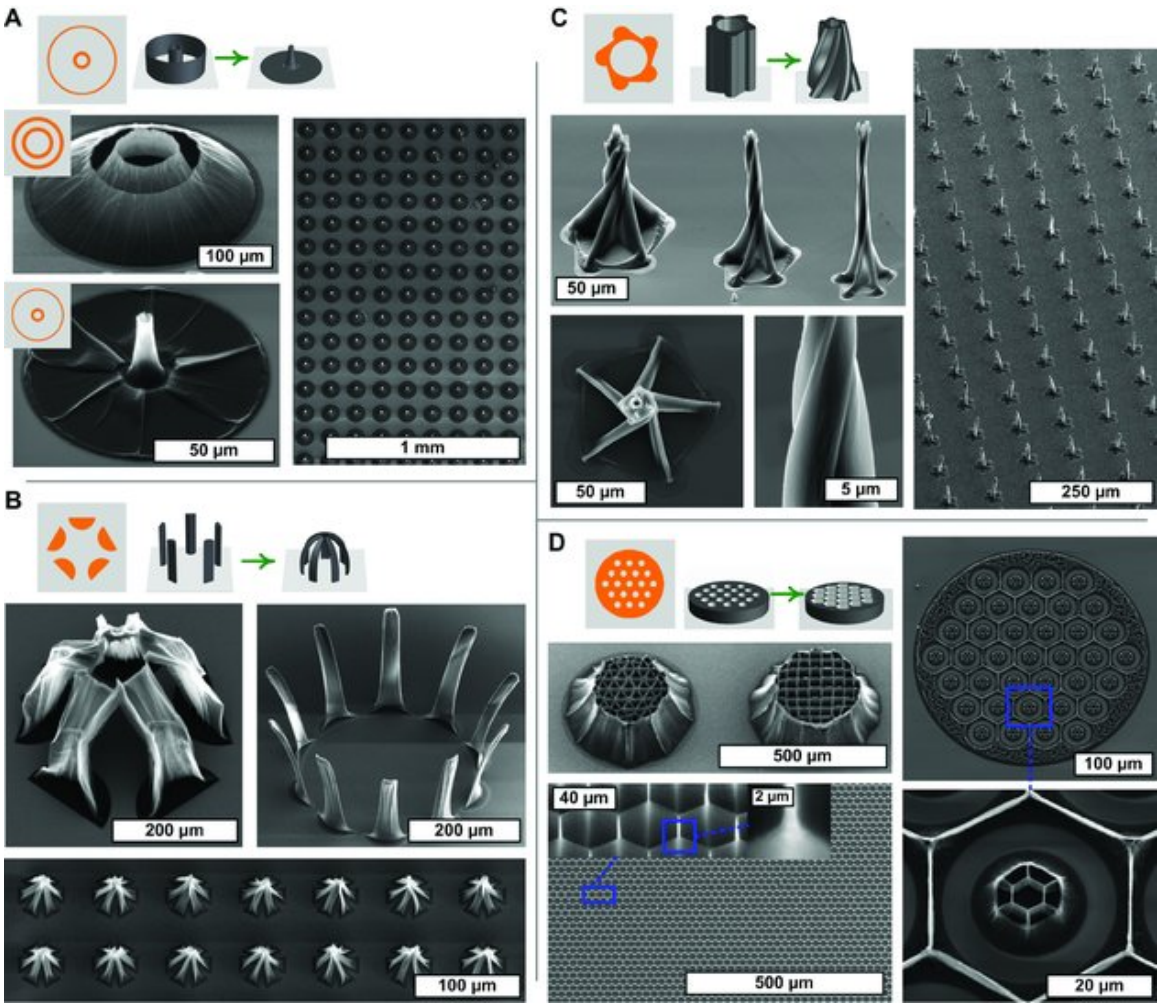

Figure 4.2 Complex CNT microarchitectures and multi-directional patterns created by coupling elementary catalyst shape building blocks. [12] (experiments conducted by Prof. John Hart's group)

4.2 Capillary forces in filamentary porous materials

Capillary force is commonly used as an alternative term to surface tension in many contexts. It has two forms - contact line surface tension and meniscus induced capillary pressure. In this section, the capillary forces that are present in the filamentary porous materials are discussed in terms of two liquid boundary conditions, which could possibly represent the experiment conditions before and after the evaporation.

Experiment evidence shows that densification occurs during both condensation and evaporation. Similarly, other researchers also reported similar experiments showing that the densification occurs at the both stages. Zhao et al. [13] showed that the densification occurs before evaporation by freezing the liquid. Chakrapani et al. [14] demonstrated that the densification mainly occurs during the drying (evaporation) process. Although the surface tension induced capillary force are generally considered as the driving forces responsible for the overall densification, it is likely that the forms and the magnitudes of the capillary forces are different before and after evaporation.

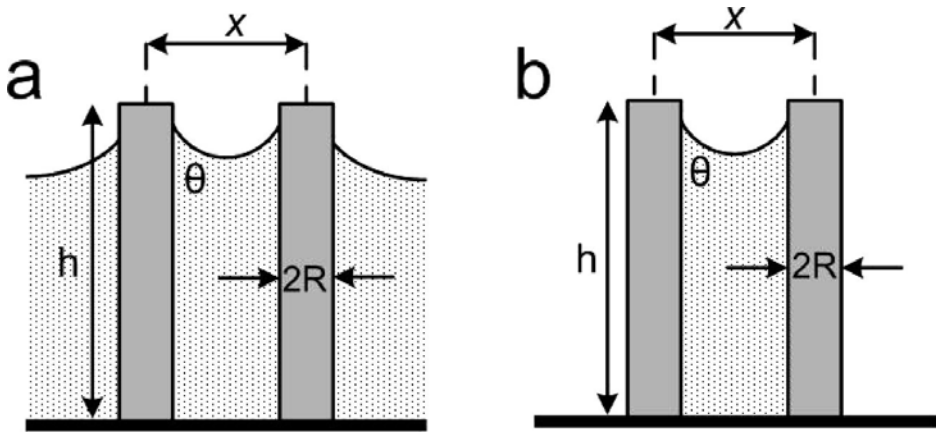

Continuous body of liquid (or infinite boundary condition)

Liquid bridge: Liquid is trapped inside the structure.

Figure 4.3 Schematic of two boundaries conditions in capillarity

First, two cases of the liquid boundary conditions are presented in the Figure 2.1. The boundary condition in Figure 3 (a) is that the liquid-vapor interface is flat at the infinity, which means the hydrostatic pressure $p_\infty = p_{atm}$ in the liquid phase at the infinity. This condition possibly represents the case when the nanotubes are immersed in the liquid. The second boundary condition in Figure 3(b) is that the liquid is trapped inside the structure and we call it liquid bridge, which indicates that the volume of the liquid is constant. This condition possibly represents the case when it is at the late stage of the evaporation in large scale immersion of CNT forests or the individual pre-patterned CNT structure is infiltrated with liquid separately.

Second, the forces exerted on the individual CNT are identified, as shown in the Figure 4.1. Surface tension γ is exerted on the three-phase contact line, and the corresponding contact angle is θ. Hydrostatic pressure *p* is exerted on the liquid-solid

interface on the CNT wall. The total force suffered by the individual CNT would be the integration of surface tension along the contact line plus the pressure p integrated over the CNT wall that is in contact with liquid, namely $\int_{L_{contact}} \vec{\gamma} dl + \iint_{S_{contact}} \vec{p} ds$.

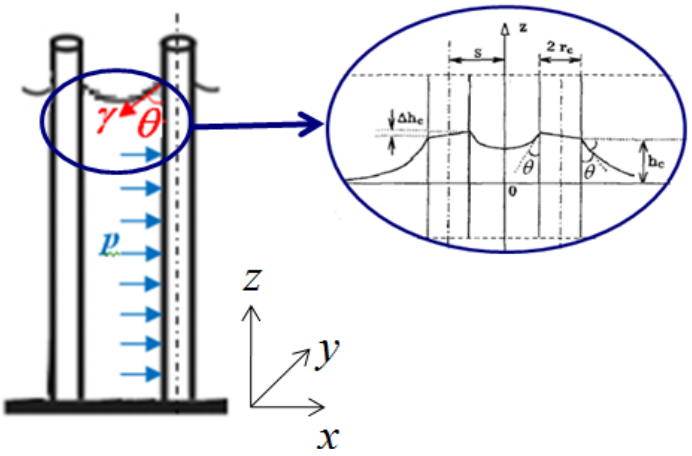

Figure 4.4 Capillary interaction and meniscus around neighboring micropillars

As shown in the magnified view in Figure 4.4, the meniscus profile can be fairly complicated even just for two cylinders. To be precisely, the meniscus profile can be calculated from the nonlinear Laplace equation of capillarity, namely,

$$(1+z_y^2)z_{xx} - 2z_x z_y z_{xy} + (1+z_x^2)z_{yy} = q^2 z(x,y)(1+z_x^2+z_y^2)^{3/2}$$

where $q^2 = \gamma / \rho g$.

Alternatively, we can also derive the driving forces from the derivative of the free energy of the system. P. Kralchevsky et al. [15] have derived the free energy for the capillary interaction between two cylinders for the case shown in Figure 4.3 (a) where

liquid is continuous. The expression of the capillary interaction can be expressed as following,

$$E_c = 2\pi r_c^2 \cdot \gamma \cos^2 \theta \ln(Kqs)$$

where r_c is the radius of the cylinder, γ is the surface tension of the liquid, θ is the contact angle of the liquid, K is a constant not related to the system, s is the half distance between the centers of the two cylinders. Therefore, the driving force for the capillary interaction can be easily obtained, namely,

$$F_c = \frac{dE_c}{ds} = 2\pi r_c^2 \cdot \gamma \cos^2 \theta \cdot \frac{1}{s}.$$

We can get three important implications from this expression: (1) The capillary interaction is attractive for the two cylinders with the same materials; (2) the capillary force is long range as it scales with s^{-1}; (3) when contact angle $\theta = 0$, the capillary interaction is still attractive, which indicates that the surface tension on the contact line is not necessarily responsible for the attracting driving force ($\gamma \sin\theta = 0$).

Next, we consider the case shown in Figure 4.5 (b) where an isolated liquid bridge is present. In this case, the Laplace pressure becomes dominant, i.e.

$\Delta p = p_{liquid} - p_{atm} = \gamma / R_{meniscus} = 2\gamma \cos\theta / x$ for the case of two parallel solid walls. For the case of liquid bridge between cylinders, the Laplace pressure scales similarly $\Delta p = \gamma \cos\theta / x$.

The difference of torques generated by the surface tension on contact line and by the Laplace pressure on CNT walls can be estimated as following,

$\tau_{Surface\ tension} = \gamma \cos\theta wH$ and $\tau_{Laplace\ \text{pressure}} = \gamma \cos(\theta) wH^2 / 2x$. The ratio of two gives

$\tau_{Surface\ tension} / \tau_{Laplace\ \text{pressure}} = 2x / H$. When the spacing *x* is much less than the height of the structure H, Laplace pressure induced torque is much stronger than the surface tension's. This ratio will also decrease as the spacing *x* decreases

In summary, under the condition of continuous body of liquid, the attractive capillary interaction will be responsible for the densification. Under the condition of liquid bridge, the Laplace pressure will be dominant and responsible for the further densification and the causes the collapse of some CNTs.

4.3 Controlled bending of CNT forests by elastocapillary densification

4.3.1 Motivation

Asymmetric assemblies of nanostructures are sought to mimic the function of biological structures such as cilia, and to create complex textures for uses including dry adhesives and directionally-wetting surfaces. Importantly, such assemblies are difficult to fabricate by traditional methods such as photolithography and etching [16]. We report a mechanism whereby ensembles of nanoscale filaments self-assemble into asymmetric (bent) aggregates by infiltration and subsequent evaporation of a liquid. Quantitatively, we show that the lateral deflection of the filaments can be controlled precisely by the pattern shape and the coupling strength among the filaments. The finding provides insight into analogous behaviors in nature where biological filaments interact with liquids. In particular, bending filament assemblies are critical to mimic structures such as micro-hairs of insects [17]. More importantly, bending filaments can be combined to form dome shapes which are abundant in nature. The mechanism we discuss may present an enabling technique for scalable fabrication of asymmetric filament assemblies at a wide range of length scales.

For an ensemble of vertically aligned filaments, a critical cluster size is determined by a balance between elastic and capillary forces during densification. Any cluster having a larger size becomes unstable and forms internal voids. This critical size has been derived for various filament assemblies, like polymer micropillars and CNTs [13, 14, 18]. We consider filament assemblies smaller than the critical cluster size, which

do not form internal voids during densification. Uniquely, while previous studies investigated the densification of non-patterned CNT forests, or CNT forests patterned into shapes having rectangular or circular (azimuthally symmetric) cross-sections, we study the behavior of bilaterally symmetric shapes. A shape with bilateral symmetry, such as a semicircle, has only one axis of symmetry. As discussed later, coupling between the local capillary forces and the geometry of these shapes causes a lateral deflection during the densification process.

The process for creating bent CNT microstructures is as follows (Fig. 4.5) [19]. First, a film of iron (1 nm thickness) is deposited by e-beam evaporation on a silicon wafer coated with photoresist patterns having semicircular holes. After lift-off, the iron forms isolated islands each of which is designed to have an area smaller than the critical cluster size for a given forest height, thus forming a single aggregate upon densification. Then, the iron catalyst is annealed in a mixture of He and H_2 at 775°C followed by the CNT growth step where C_2H_4 is added to the gas mixture at the same temperature [11]. The process results in CNT forests with heights ranging from ten to hundreds of micrometers depending on the growth step duration (Fig. 4.5b). Finally, the substrate with the CNT forests is placed upside down on a metal mesh covering a beaker containing a boiling organic solvent such as acetone. The condensed liquid wets the CNTs by rising independently within each CNT microstructure due to capillary pressure, and then the solvent evaporates when the substrate is removed from the vapor stream. After the structure is dried, the deflections are held by van der Waals force or mechanical interlocking. In particular, CNT forests grown from semicircular patterns deflect laterally, creating bent micropillars (Fig. 4.5c). Unlike immersion, the condensation

process is able to form small closely packed individual microstructures because the condensed liquid volume does not bridge neighboring structures.

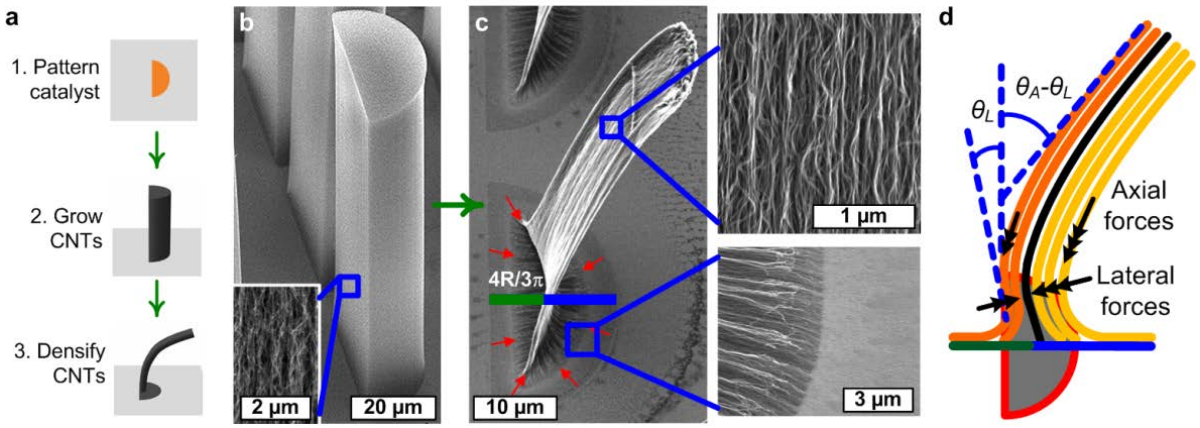

Figure 4.5 Fabrication of asymmetric microstructures by elastocapillary densification of semicylindrical CNT forests: (a) process steps; (b) SEM image before densification, with inset showing low-density vertically aligned morphology; (c) SEM image after densification, with insets showing laterally aligned CNTs facing centroid of the base and high density vertical CNTs in the upper portion; (d) densification induced lateral and axial forces [19] (experiments conducted by Prof. John Hart's group)

4.3.2 Modeling

The bending behavior of the assemblies poses interesting questions. What is the mechanism? How to control the bending angle? Since the collective properties of densely packed filament assemblies strongly depend on their morphology [20, 21], the ability to predict and control the shape of the structures is critical. Imaging of the bent structures gives initial insights. First, we find that the filaments at the base are flattened onto the substrate (Fig. 4.5c) due to capillary pressure [18] on the perimeter of the microstructure. The lengths of flattened filaments are different, and the densified structure is located in

close proximity to the centroid of the original cross section of the growth pattern. Further, the structure near the base is prone to bend toward the straight edge of the semicircle. In contrast, the upper portion of the structure, however, bends toward the opposite (curved) edge.

Based on these observations, we identified two major effects contributing to the bending behavior (Fig. 4.5d). First, the filaments push against each other, introducing a distribution of lateral forces. The difference in population of filaments on both sides of the centroid results in the structure bending toward the straight edge. Second, the contraction of filaments creates a distribution of axial pulling forces that act asymmetrically on the upper portion of the forest. Based on the slip characteristics of filaments within the forest, this effect can lead to bending toward the curved or straight edge of the semicircle. The collective actions of the two effects determine the final bending angle of the densified structure.

Now consider the first effect. Figure 4.6a shows the cross-section of a semi-cylindrical filament microstructure with radius *R*. After densification, the radius reduces to $a = R/\sqrt{D}$, where D is the densification factor. We have assumed uniform densification, so that the cross-section maintains the same shape after densification. The *x* coordinate coincides with the symmetry line. The z axis passes through the centroid, which does not move during the densification process. The whole structure bends within the *x*-*z* plane by θ_L, or $\beta = \pi/2 - \theta_L$. Consider the bending of an arbitrary filament, ABC, in Fig. 4.6a. A magnified view is given in Fig. 4.6b. To accommodate the bending of the whole structure, the filament bends by an angle γ in plane ABC such that the portion BC is parallel to the x-z plane and the angle between BC and the substrate equals

β. To help visualize the relation, a line CD perpendicular to the substrate is shown. Denote the angle between the flattened portion AB and the *x* axis by φ. The geometric relation gives $\cos\gamma = \cos\beta\cos\varphi$.

Lateral forces

In this first effect filaments are allowed to slide freely to each other, and we focus on forces locally perpendicular to the filaments, i.e., the lateral forces. For example, the filaments in Fig. 4.6a are bent after densification. The elastic restoring forces serves as the lateral forces that push the filaments against each other. Furthermore, we assume that all the filaments are parallel to each other above a certain plane to simplify the problem. Above this plane van der Waals force is responsible for holding together all the filaments, however it does not contribute to bending given all filaments are equally spaced (except for the few filaments on the perimeter of the semi-cylinder). Below this plane, the van der Waals force is neglected. Then all the lateral forces should be balanced on this plane. An initially vertical structure will bend until the total lateral force equals zero to reach equilibrium. For each filament the lateral force is determined by its location and bending angle. We treat each filament as a beam. Consider beam bending under two perpendicular forces, P_1 and P_2, as shown in Fig. 4.6b. Denote the deflection angles by γ_1 and γ_2. The analysis of large beam deflection givers $P_1 / P_2 = \lambda(\gamma_1) / \lambda(\gamma_2)$, where $\lambda(\gamma)$ is a positive dimensionless monotonic function [22]. Note that the effect of force location and beam stiffness cancels out in the ratio. Each bent filament exerts an elastic force, $P(\gamma)$, to the

microstructure. The integration of $\mathbf{P} = \lambda(\gamma)\mathbf{u}_p(\varphi,\beta)$ over all filaments gives the total lateral force, where $\mathbf{u}_p(\varphi,\beta)$ is a unit vector in the force direction.

Due to the bilateral symmetry of the semi-cylindrical shape, the total lateral force component in the *y* direction cancels out. For each filament, the projection of the lateral force in the *x*–*z* plane is given by $P_t = \lambda(\gamma)(\mathbf{u}_p - \mathbf{u}_p \cdot \mathbf{j})$ with **j** being the unit vector in the *y* direction, or

$$P_t(\varphi,\beta) = \lambda(\gamma)\frac{\cos\varphi\sin\beta}{\sqrt{1-\cos^2\varphi\cos^2\beta}}. \tag{4.1}$$

$P_t(\varphi,\beta)$ is positive for filaments to the right of the *y* axis ($\cos\varphi > 0$), meaning they push left. Those filaments to the left of the *y* axis push right. We use the shooting method to find the critical β_c which satisfies $\iint P_t(\varphi,\beta_c)dA = 0$. Note that a multiplier, i.e. the number of filaments per unit area in the as-grown forest has been dropped since it is uniform. The integration extends over the semi-circular cross-section of radius *R*. Our calculation shows $\beta_c < \pi/2$, or the whole structure bends toward the straight edge. Note that $\theta_L = \pi/2 - \beta_c$.

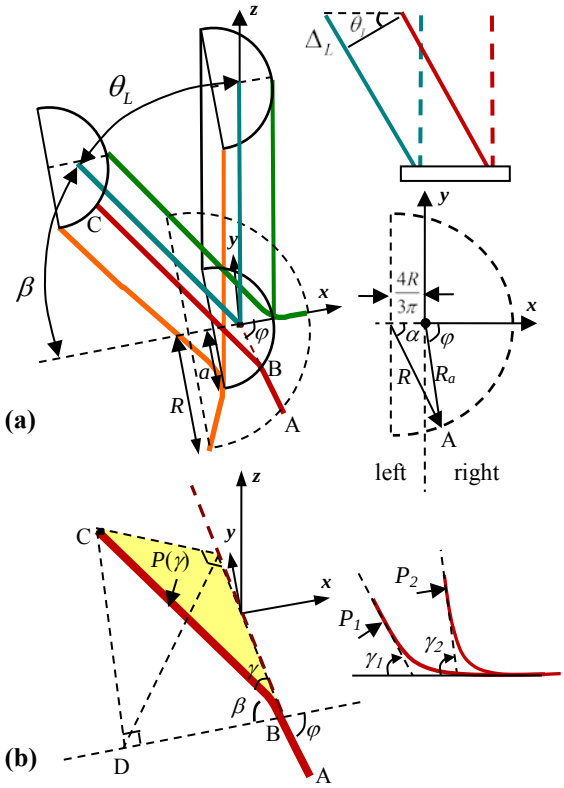

Figure 4.6 Contribution of lateral forces to the elastocapillary bending of a semi-cylindrical filament forest. (a) Schematic of the as-grown shape of the filament forest and the shape after densification. (b) The bending state of an arbitrary filament within the deformed structure.

It is instructive to examine the resultant lateral force when the structure is vertical ($\beta = \pi/2$). In this situation, $P_t(\varphi, \beta) \sim \cos\varphi$ since all filaments have the same $\lambda(\pi/2)$ coefficient. The total lateral force is proportional to $\int_{-\pi/2}^{\pi/2}\int_0^R \cos\varphi r dr d\alpha$ or $-R^2/3$. This net negative force pushes the whole structure to bend toward the straight edge until equilibrium is reached.

Axial forces

To understand the second effect which is due to axial forces, we begin with an introduction of the concept of differential length. Figure 4.7b shows two semi-circles illustrating the cross-section before and after densification. The origin of the *x*-*y* coordinate coincides with the centroid. Consider a filament attached to the substrate at location (r, φ) before densification, where *r* is the distance to the centroid and φ is the angle relative to the *x* axis. After densification, the lower portion of the filament flattens on the substrate toward the centroid and the remaining portion bends upward to form the densified structure, as seen in Fig. 4.5. The flattened length, $\Delta_d(r,\varphi) = (1-1/\sqrt{D})r$, is shown by the blue segment in Fig. 4.7b. The differential length is defined as the height reduction of each filament, $\Delta_d(r,\varphi)$.

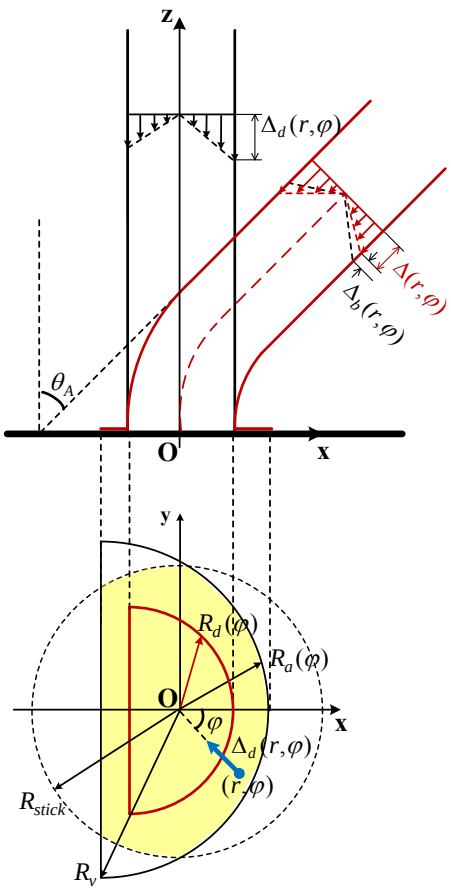

Figure 4.7 Contribution of axial forces to the elastocapillary bending of a semi-cylindrical filament forest. (a) side view (b) cross-section on the substrate. The blue dot shows a filament originally vertical at location (r,φ). After densification, its lower portion (blue segment) flattens on the substrate orienting toward the centroid, while its upper portion bends upward to form the densified structure.

In actuality, the slip between filaments such as CNTs is constrained by a top "crust" consisting of entangled filaments due to the self-organization mechanism of the initial stage of growth [23, 24]. We define a sticking plane above which all filaments are connected. As is evident later, the location of the sticking plane does not affect the determination of the bending angle. Below this plane, filaments can slide to each other freely when they bend to compensate for the differential length. Above this plane, the

structure does not bend since the differential length has been compensated by the bending below.

We use energy minimization to obtain the bending angle θ_A due to the axial forces, which pull down the structure and generate stretching energy in each filament. This energy is partially relaxed when the sticking plane moves down by Δ_0 and rotates by θ_A. The bending of the whole structure changes the differential length by $\Delta_b(r,\varphi) = \theta_A r\cos\varphi$, as shown in Fig. 4.7. The distribution of differential length is then given by $\Delta(r,\varphi) = \Delta_d(r,\varphi) - \Delta_b(r,\varphi) - \Delta_0$. The stretching energy is $G = (SN/2)\int_0^{2\pi}\int_0^{R_a(\varphi)} \Delta^2 r dr d\varphi$, where S is the axial elastic stiffness of an individual filament, *N* the number of filaments per unit initial cross-section area, and $R_a(\varphi)$ the boundary of the initial cross-section before densification. The values of *S* and *N* are insignificant as they drop out later. The high aspect ratio makes a filament very flexible, thus its bending energy can be neglected. Calculation shows that $R_a(\varphi) = (4R/3\pi)(\sqrt{\cos^2\varphi + (3\pi/4)^2 - 1} - \cos\varphi)$ on the curved edge and $R_a(\varphi) = -(4R/3\pi)/\cos\varphi$ on the straight edge. Substituting the expressions of Δ_d, Δ_b into *G* and take $\partial G/\partial\Delta_0 = 0$, $\partial G/\partial\theta_A = 0$, we have

$$\theta_A = (1-1/\sqrt{D})\frac{8\left(\int_0^{2\pi} R_a^3 d\varphi\right)\left(\int_0^{2\pi} R_a^3\cos\varphi d\varphi\right) - 9\left(\int_0^{2\pi} R_a^2 d\varphi\right)\left(\int_0^{2\pi} R_a^4\cos\varphi d\varphi\right)}{8\left(\int_0^{2\pi} R_a^3\cos\varphi d\varphi\right)^2 - 9\left(\int_0^{2\pi} R_a^2 d\varphi\right)\left(\int_0^{2\pi} R_a^4\cos^2\varphi d\varphi\right)}. \quad (4.2)$$

The expression suggests that θ_A increases with the densification factor, and vanishes when $D = 1$. Evaluation of Eq. (4.2) gives $\theta_A = -9.5(1 - 1/\sqrt{D})$ degrees, with negative sign for bending toward the straight edge.

Effect of slip

Now we consider slip of filaments from the sticking plane, which is likely to occur at the perimeter of microstructures where the axial forces are larger. We define a cut-off contour, R_{stick}, beyond which filaments can slip relative to one another and therefore do not contribute to the total axial forces. The contour is a circle centered at the centroid, since the flattened length, $(1 - 1/\sqrt{D})r$, is independent of φ. To calculate the stretching energy, the integral domain now reduces to the yellow intersection area of the circle with radius R_{stick} and the original semicircle. We find a critical radius, $R^c_{stick} = 0.86R_v$, where R_v is the maximum distance from the centroid to a point on the semi-circle. When $R_{stick} > R^c_{stick}$, i.e., the main aggregate (where slip is prohibited) equals the whole structure, the structure bends toward the straight edge. In contrast, when $R_{stick} < R^c_{stick}$, i.e., the main aggregate is smaller than the whole structure and slip occurs at the corners, the structure bends toward the curved edge. R_{stick} can be treated as a measure of the interfacial strength between filaments, as will be shown experimentally for CNTs later. The net deflection combines the two effects. As shown in Fig. 4.6, θ_L will induce an additional differential length, $\Delta_L(r, \varphi) = r\cos\phi\tan\theta_L$. Under the constraint of sticking

plane this length causes bending similar to that descried in the second effect. The net deflection angle is $\theta = \theta_A - \theta_L + \tan\theta_L$, positive for bending toward the curved edge.

4.3.3 Results and discussions

The model can be readily extended to other cross-section shapes, and is verified by experiments. Specifically, we have considered the elastocapillary densification of solid and hollow semi-cylindrical filament assemblies parameterized by $r = R_i / R_o$, with inner radius R_i and outer radius R_o. Figure 4 gives representative results, showing that the total deflection is highly sensitive to *r* and to the parameter $k = 1 - R_{stick} / R_v$, which describes the amount of slip.

Figure 4.8a shows that when slip is absent ($k = 0$), the densified structure always bends toward the straight edge ($\theta < 0$). With increasing *r*, the microstructure becomes a thin "C" shape and bends more. With slip among the filaments, the structure can bend toward the curved edge ($\theta > 0$). Take $k = 0.4$ as an example. At *r* = 0, i.e., a semi-circular shape, the bending angle is 13^o. While the angle is -7^o when $k = 0$. This interesting transition can be understood as follows. As shown in Fig. 4.7, when there is slip, those filaments whose base is outside the R_v circle lose grip on the sticking plane and do not contribute to creating a differential length. As *k* increases, more filaments in the corners to the left side of the centroid lose grip. As a result, those filaments to the right of the centroid win, and the resultant axial pulling force bends the structure toward the curved edge. This explains the possible reversal of the bending direction as *r* increases, and the further increase of the bending angle when *k* changes from 0 to 0.4.

This effect becomes more important as r increases, because a greater proportion of the filaments are near the corner of the shape. Consequently, the net bending angle toward the curved edge is larger. The $k = 0.1$ curve shows that when the interfacial strength of slip is fixed, changing the shape factor r can tune the bending from toward the straight edge to the curved edge. This intriguing behavior is captured by the experimental data.

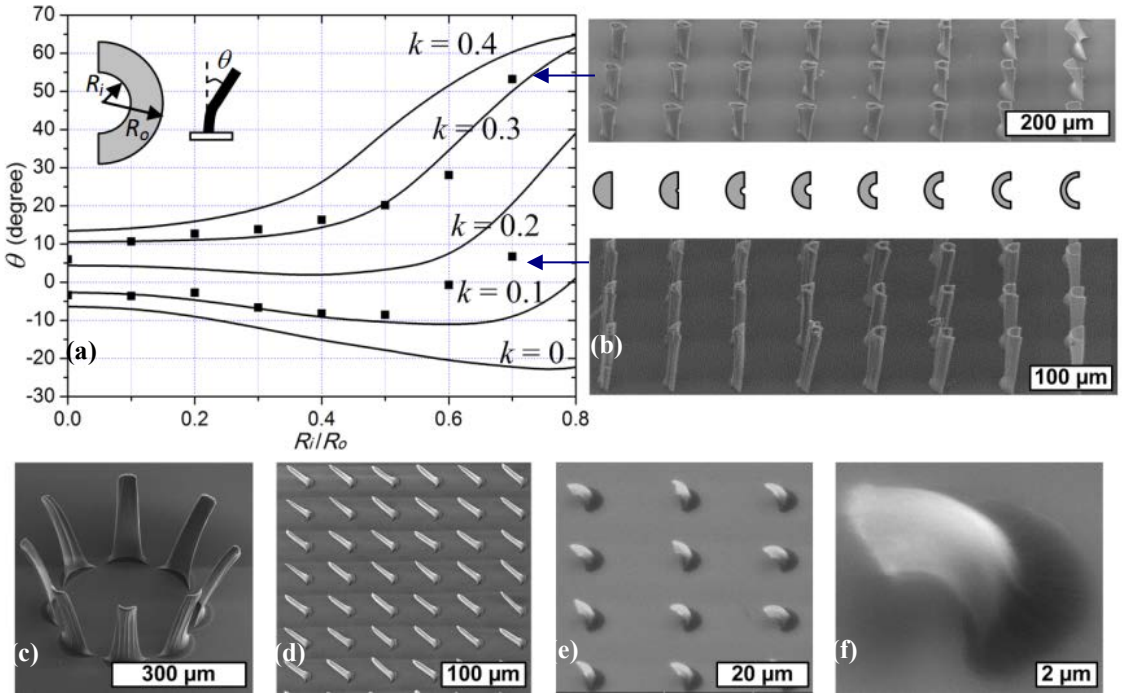

Figure 4.8 Validation of model prediction and demonstration of asymmetric filament assemblies. (a) Bending angle changes as a function of R_i / R_o with different amount of slip. Solid squares for experimetnal data. (b) Precise control of bending angle by variation of R_i / R_o. The two sets represent different amount of slip by varying the growth condition of CNTs. Each image shows three identical rows to verify repeatibility. (c) "Blooming flowers" of radially-oriented CNT structures bending toward the curved edge of the semicircle. (d) Large arrays of bending CNT structures. (e) Short bending CNT structures, magnified view in (f). [19] (experiments conducted by Prof. John Hart's group)

We have validated these trends in experiments with CNT microstructures. Figure 4.8b shows two sets of CNT structures, confirming the capability to tune the bending

angle based on the initial pattern of filaments prior to elastocapillary densification. Each row shows a series of shapes with different r, and the measured bending angles are representated by the solid squares in Fig. 4.8a. The different trends are created by varying the intensity of plasma etching of the CNTs in O_2/Ar prior to densification. We find that plasma etching efficiently reduces the main aggregate size by reducing the CNT density at the top and outer surface of each structure. Therefore, plasma etching enables more slip around the edges of the CNT structure, and causes more bending toward the curved edge which agrees precisely with the model. The upper image matches the $k = 0.3$ curve while the lower one is close to the $k = 0.1$ curve. Non-uniformity in densification changes the cross-section shape, which may partially account for the discrepancy between prediction and experiments.

Understanding of the bending mechanism also allowed us to create complex arrangements of CNT structures as shown in Fig. 4.8c-f. These include flower-like architectures made from circular arrangements of structures that bend toward a common point; and large arrays of bending structures that resemble micro-hairs on the skin of insects. Notably, these structures range in size over two orders of magnitude, from a few microns to hundreds of microns in height. These special geometries, coupled with the attractive mechanical, electrical, and chemical properties of CNTs provide a promising foundation for future work.

4.4 Understanding cross-section shape change of CNT microstructure during densification

4.4.1 Motivation

Subjected to drying or temperature change, many low-density cellular materials, such as wood[25], soil[26], gels[27, 28] and foams[29], undergo considerable volume shrinkage. The so called densification process often accompanies significant structural change in both micro and macro scales, leading to the modification of the materials' mechanical and electronic properties[20, 30]. In particular, a thin film on solid substrate will demonstrate unique stress development[31] upon densification. Here the substrate provides a mechanical constraint and prevents stress relaxation in the thin film. The stress accumulation thus inversely acts on the thin film and cause various morphology changes such as cracks[32], wrinkling[33] in sol-gel thin films and micro-cracks[34] in carbon nanotube (CNT) thin film.

Most previous work has focused on determining the critical size of the filament assembly by the balance of capillary and elastic forces [35] or the equivalent energy minimization[13]. Both methods inexplicitly assumed that the densification process is uniform, which means that the cross-section shape of the filament assembly does not change during the densification process. Specifically, the force equilibrium was considered under the assumption of uniform shape change. However in recent experiments, non-uniform shape change is observed for polygonal CNT forests as shown in Fig. 4.9 [36].

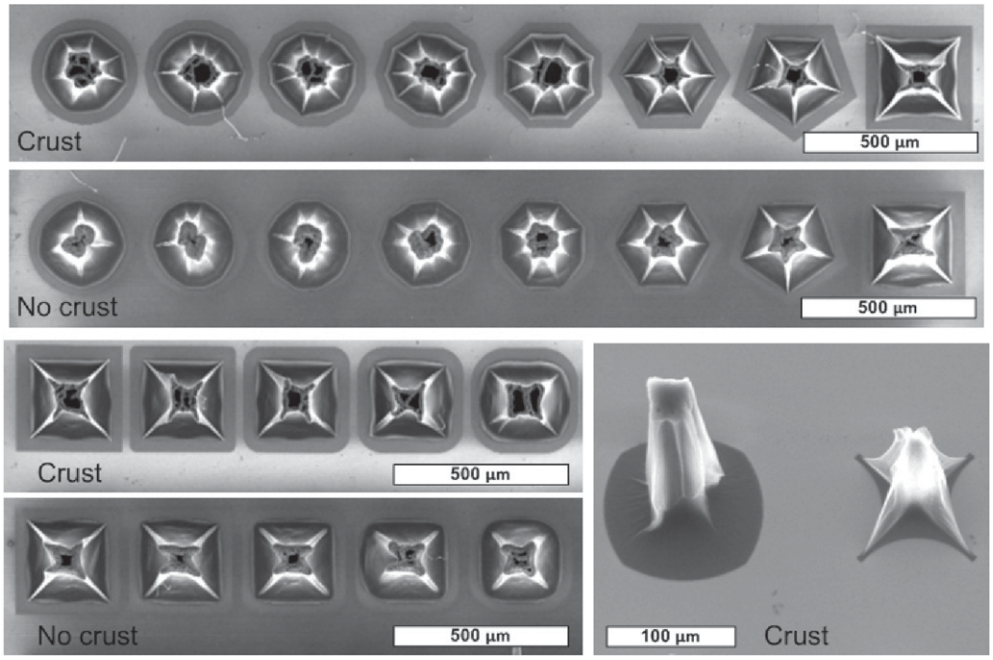

Figure 4.9 Effect of the catalyst pattern shape and the top crust on the cross-section after densification [36]

4.4.2 Modeling: substrate effect

Nonlinearities in both lateral stiffness and load are considered in the model. If we only include the nonlinearity in stiffness, no shape change will be observed because the stress is always uniformly distributed in the body. The nonlinearity in load is induced by the substrate constraint, which is key to this model.

We first model the lateral stiffness of the CNT forest as a continuum material. Due to the highly porous nature of the as-grown CNT forest with volume fraction as low as 0.1%, its mechanical response in the transverse direction (opposed to the axial direction along the nanotubes) is very similar to foam structures. Following Gibson and Ashby's work[37], compressive response of foams typically consists of three regimes:

linear elasticity at low strain; followed by a "yielding" plateau at intermediate deformations; finally truncated by a regime of densification where a dramatic hardening occurs. The waviness of the CNTs together with the entanglement provides the initial resistance to compression which functions similarly to the interconnected networks in the foam. The mechanical properties in the axial direction are less concerned in this paper, because densification occurs only in the transverse direction. Therefore, we treat the densification as a 2D problem to track the evolution of the cross-section shape. Note that the cross-section we considered is fully developed which means there is no shape variation above the selected cross-section.

The densification of CNTs we are interested is usually a large deformation, therefore any geometry related nonlinearity should be considered, especially for loading. As mentioned earlier, the elastocapillary densification is driven by capillary force coupled with elastic restoring force due to bending of the CNTs. Consider a CNT forest with square cross-section as shown in Fig. 4.9. In our 2D continuum model, the capillary pressure which exerted on the side wall of CNT forest simply reduces to biaxial compression. The elastic restoring force is proportional to deflection of each CNT, which gives $\mathbf{f}_n = -3\mathbf{d}_n EI / L^3$. $\mathbf{d}_n$ is the deflection vector of the nth CNT, E and I are the Young's modulus and the area moment of inertia respectively, which are same for all individual CNTs, and L is the height of the cross-section we considered. Note that the negative sign account for the opposite direction between the displacement and elastic restoring force. Usually the total number of CNTs is substaintial, and we transform the relation into continuum argument, namely $\mathbf{f}_n \rho dA = -3\mathbf{d}_n EI / L^3 \rho dA$ and define

$\mathbf{b}_n = \mathbf{f}_n \rho = -3\mathbf{d}_n \rho EI / L^3$ as the equivalent body force which is dependent on displacement. Density ρ is the number of the CNTs per unit area. Consider an arbitrary infinitesimal unit in the solid, the magnitude of the body force is thus proportional to its displacement. Assuming the square deforms uniformly, the body force exerted on the diagonal is greater than the one off the diagonal, which triggers the star effect near the corner. Because the capillary pressure is always perpendicular to the walls of the CNT forest, the directions of the equivalent biaxial forces also changes with the onset of the star effect. Upon large deformation, the diagonal component of the resultant force from capillary pressure on the two sides continually decreases, whereas the component perpendicular to the diagonal increases and further sharpens the corner. Therefore the star effect is the consequence of both the displacement dependent body force and large deformation.

4.4.3 Finite Element Analysis

The finite element (FE) analysis was performed using ABAQUS/standard (ABAQUS, Inc., Providence, RI). In the FE model, the cross-section was assumed to be a deformable shell with homogeneous material properties. The material properties were described by a nonlinear hyperfoam model, which can deform elastically to large strains, up to 90% strain in compression. The elastic behavior is based on the Odgen strain energy function for hyperelastic materials:

$U = \sum_{i=1}^{N} 2\mu_i (\lambda_1^{\alpha_i} + \lambda_2^{\alpha_i} - 2 + (J^{-\alpha_i \beta_i} - 1)/\beta_i)/\alpha_i^2$ for 2D problem, where μ_i and α_i

are material parameters to be determined from test data, $\beta_i = \nu_i / (1-2\nu_i)$ in which ν_i is the Poisson's ratio, λ_1 and λ_2 are the two principle stretches, and N is up to 6 to improve the fitting accuracy. We chose N=2, which proved to be stable in our simulation. Note that $\lambda_i = 1+\varepsilon_i$. By fitting function

$\sigma_1 = \partial U / \partial \varepsilon_1 = \sum_{i=1}^{2} 2\mu_i[(1+\varepsilon_1)^{\alpha_i} - 1] / [\alpha_i(1+\varepsilon_1)]$ to the stress-strain relation obtained from uniaxial transverse compression test data on the CNT forest, we can get four material parameters μ_i and α_i (i=1, 2). For example, $\mu_1 = 2$, $\alpha_1 = 20$, $\mu_2 = 0.0002$, $\alpha_2 = -5$ give a typical stress-strain curve as shown in Fig. 4.10.

Take the square cross-sectional CNT forest as example (See Fig. 4.11a), the FE analysis was conducted on the quarter of the square due to symmetry. The corresponding symmetry boundary conditions are applied on the two sides. Loading of biaxial compression is straight forward, which essentially reduces to a line pressure in the quarter part. The displacement/time dependent body force is not supported in ABAQUS GUI loading modules. Alternatively we specified the distributed body force by using DLOAD subroutine in Fortran.

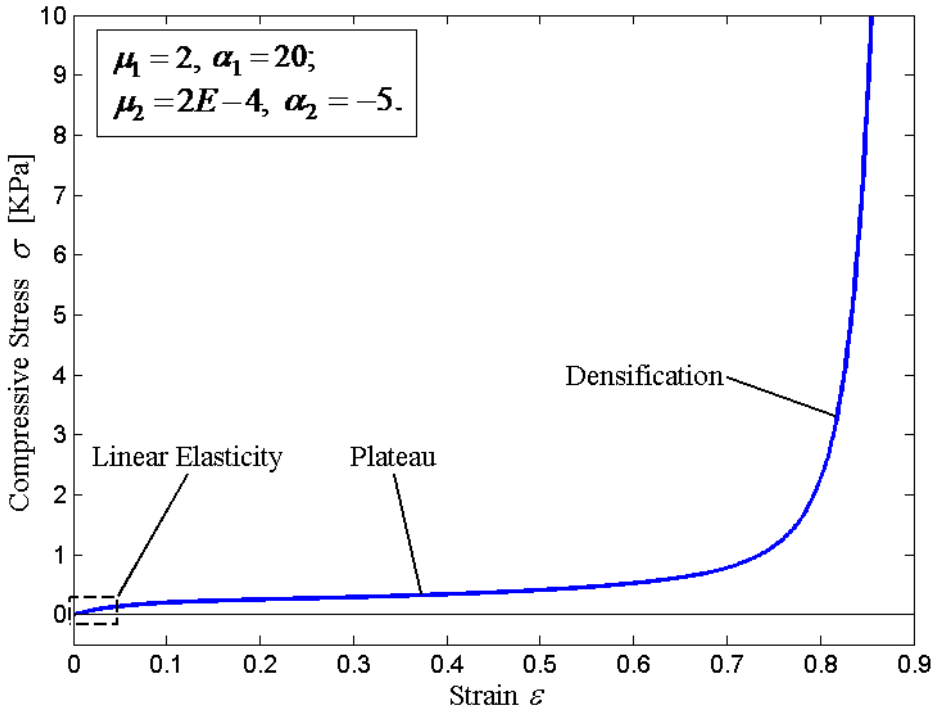

Figure 4.10 Compressive stress-strain curve for a typical CNT forest, fitted based on the Odgen strain energy function for hyperelastic materials. (Experiment data courtesy of Dr. Eric Meshot)

In experiment, the densification factor D is controlled by densification time (or solvents with different surface tension).With the increase of the densification factor, the star effect is normally strengthened as shown in Fig 4.11. We considered the densification as a quasi-static process so that in simulation the amount of densification can be controlled by the magnitude of biaxial pressure. Selected simulation results and the comparisons with experiment results are shown in Fig. 4.11 and 4.13.

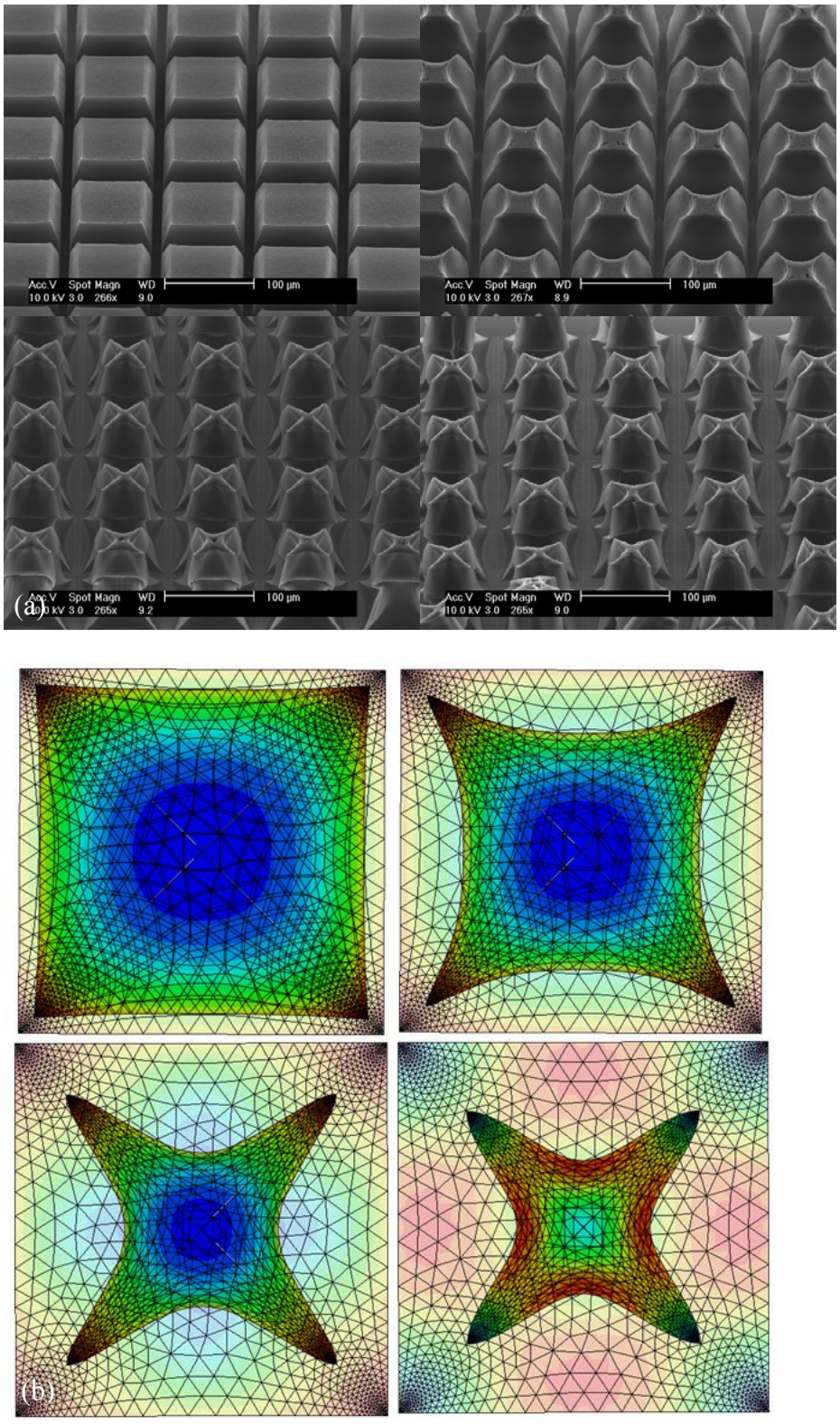

Figure 4.11 Cross-section shape change of square CNT forest at different time stages of densification (a) experiment results (b) simulation results (Experiment results courtesy of Dr. Sameh Tawfick)

Fig. 4.11 displays the star shapes generated during the different stages of the densification process. To quantify the relation between densification and the star shapes, the shape evolution was plotted for the square CNT forest as a function of densification factor S(D), where $S=R_a/R_b$ (Fig. 4.12). The initial value of S (0)=1.414 near the onset of the densification, no obvious star shape is observed due to the small deformation and the position dependent body force $\mathbf{b}_n$ being proportional to the displacement. With the increase of densification, the large deformation takes effect and the star shape starts to build up. Meanwhile the nonlinearity in lateral stiffness also starts to contribute to the star formation the when the maximum in-plain strain reaches around 0.7-0.8 at the four corners. Therefore the densification slows down at those corners first. As the densification goes on, the densified or hardened regions propagate inwardly. And the star effect slows down and reaches the maximum when the densified regions meet at the middle of the each side.

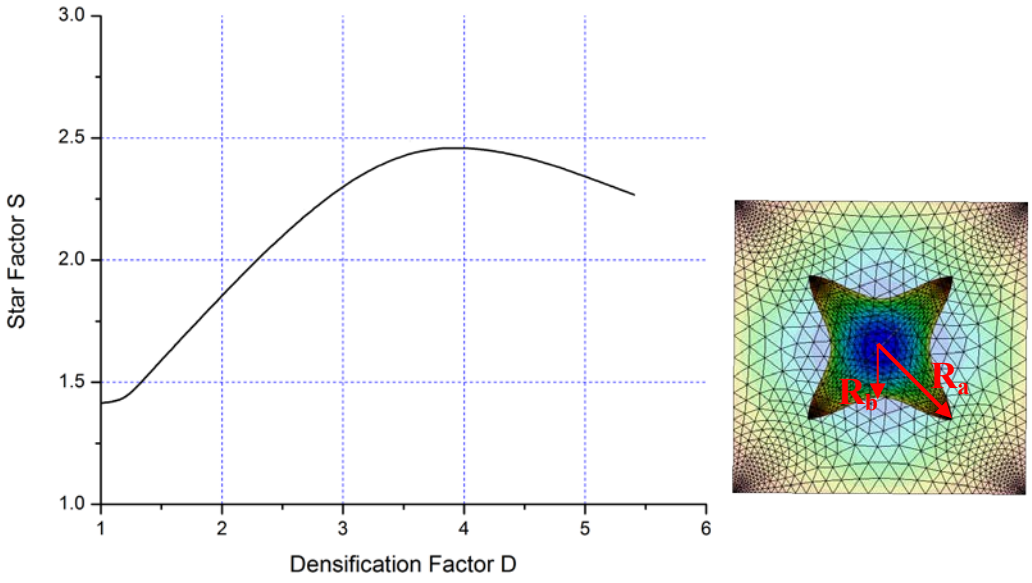

Figure 4.12 Star-shape factor versus densification factor showing the shape evolution of the cross-section

Simulations are also carried out for other polygons such as hexagons and pentagon. The more sides of the polygon are, the less the star effect is observed. Eventually, when the polygon reduces to a circle, the star effect disappears.

(a)  (b) 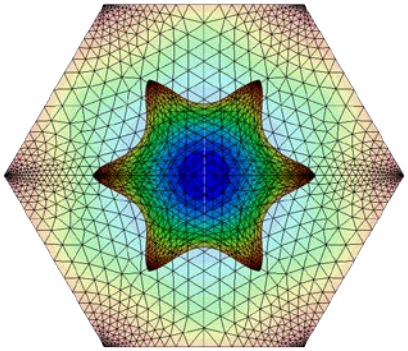

Figure 4.13 Experiment and simulation results for hexagonal shaped cross-section. (Experiment result courtesy of Dr. Sameh Tawfick)

In summary, by considering the non-uniformly distributed position-dependent elastic forces coupled with cross-section geometry, we find that the cross-section of the filament assemblies would undergo significant shape changes due to densification. The predictions by finite element analysis are consistent with the experiment results of CNT densification. With the stress development in the CNT structure, the material hardening also plays an important role in the shape evolutions when local densification goes into hardening regime. However, the model also has its limitation for predicting shape change in high aspect ratio structures.

4.5 Nonlinear lateral mechanical behavior of CNT forests

4.5.1 Motivation

In the last section, it is shown that the nonlinearity of the CNT forests' lateral stiffness may be captured by a hyperfoam model. Although CNT forests share some of the mechanical characteristics with isotropic networked foams, the orthotropic nature of vertically aligned CNT microstructure makes the mechanisms different from classical foams. In a classical model of foam [38], the initial elasticity comes from uniform small deformation within the entire network. In the second collapse stage, the "stress plateau" is due to localized bending occurs at weak points in the network. In the third densification stage, the hard contacts between neighboring structures result in the stiffening the material. In as-grown vertically aligned CNT microstructure, the slightly wavy nanotubes are connected by weak VDW bonding and the bending or buckling can only occur along the axial direction of nanotube. In the elastocapillary densification process, the surface tension coupled with lateral stiffness determines final densification factor and shape of the structure. Therefore it is crucial to understand the nonlinearity in the lateral mechanical behavior of CNT forests.

Recent experiments conducted by Prof. John Hart's group [39] tested the lateral stiffness of vertically aligned CNT structures by nano-indentation. It is also shown that the overall stiffness can be reinforced by coatings (Figure 4.14). Specifically, the amount of shrinkage during evaporation can be manipulated by thin Al_2O_3 coatings deposited conformally on the CNTs by Atomic Layer Deposition (ALD). The deposited coatings tune the ability of the CNTs to slip against one another. This insight is confirmed by

finite element modeling of individual CNT-CNT contacts as curved beams described in the following section.

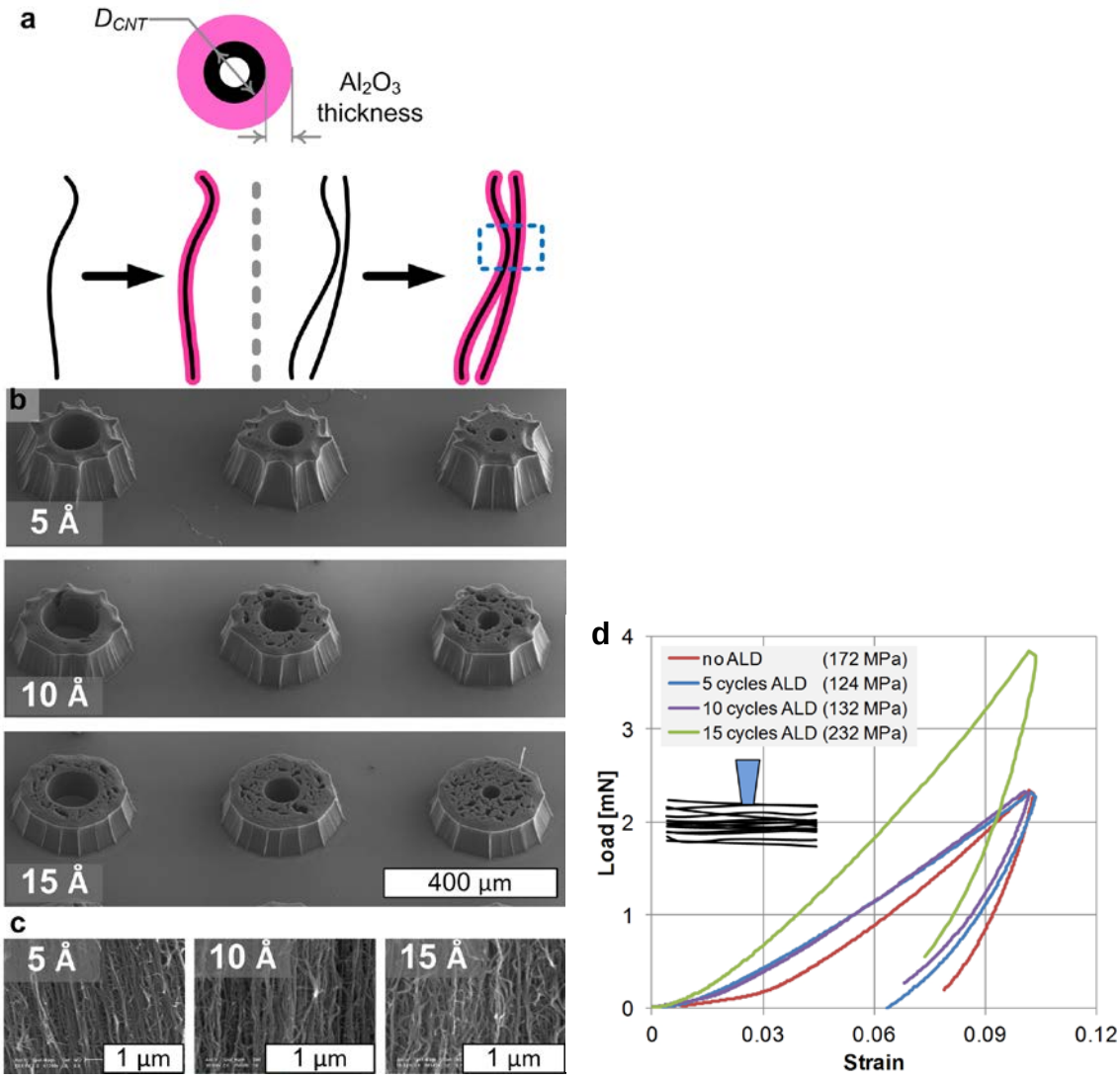

Figure 4.14 Coating of CNT with Al_2O_3 by Atomic Layer Deposition (ALD). (a) Schematics showing the thin conformal coating films, and their effects in locally "bonding" CNTs. (b) Effect of coating with 5, 10, 15 Å on capillary forming. (c) Changes in the nanoscale structure as a result of thin ALD coating. (d) Effect of Al_2O_3 coating on the lateral stiffness. [39]

4.5.2 Finite element model

We tried to capture the above obervations by building a Finite Element (FE) model. The basic idea is to impose external lateral displacement to an individual CNT and probe the induced lateral stresses. Besides, we consider the effect of coating by considering increase both in the stiffness of individual CNTs and the coefficient of friction between them. A simple core-shell model can estimate the new effective stiffness in individual CNTs[40]. The increase of coefficient of friction captures the effect of local bonding of intersecting CNTs due to thin Al_2O_3 coating.

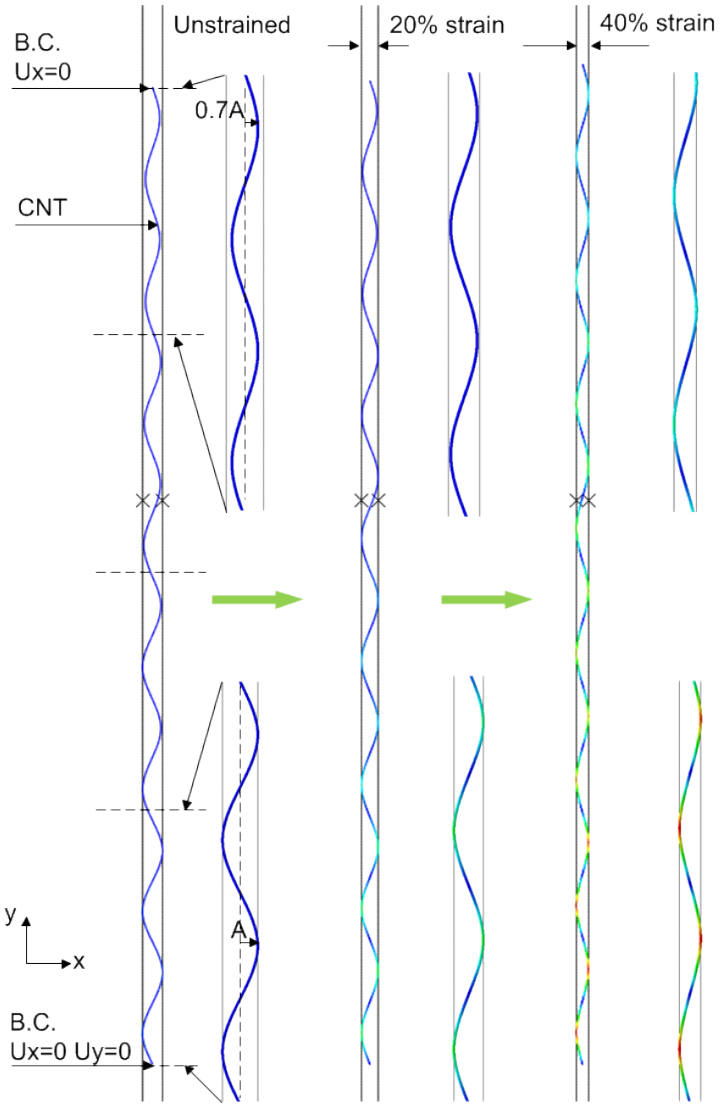

Figure 4.15 Illustration of the finite element model

4.5.3 Results and discussions

The FEA simulation was performed using ABAQUS/explicit module. The geometry of the CNTs is guided by our high resolution SEM measurements as shown in Figure 4.15. The wavy CNT contains multiple amplitudes ranging from 0.7A to A, with a fixed wavelength 15A. A beam element with circular cross-section is employed to allow large deformations of CNTs. Due to the symmetry, we constrain the displacement of the bottom of the CNT in both x and y directions, and the top only in x direction. Note that both points lie on the center line of the wave. By setting the lateral displacements of the both rigid walls to be 0.4A inwardly, the ABAQUS/explicit module tracks the lateral deformation of CNT up to 40% strain. Beginning with a frictionless condition (μ=0) between CNTs, the result shows a non-linear hardening effect as the CNT being compressed (the bottom curve in Figure 4.16). The hardening effect can be understood by the increase of contact pairs during CNT compression as shown in the schematics of Figure 4.15. Next we study the effect of Al_2O_3 coating by adding frictions (μ=0.25 and μ=0.5) between the CNTs. The top two curves in Figure 4.16 show that hardening effect further increases with the frictions. From energy point view, comparing the frictionless to the frictional situations, the area between the corresponding curves is equal to the extra work that the external force has to do. Specifically, the extra work comprises of the frictional dissipation energy and the extra strain energy in the CNT due to the frictional constraint in axial direction. We also show that for 20% increase in stiffness of CNT, the lateral stress scales linearly by 20% increase with the same deformation. As a result, the model confirms that the existence of Al_2O_3 coating can cause a significant hardening

effect in lateral compression of CNT microstructures, based on the additional frictions between CNTs and the reinforced stiffness of CNTs.

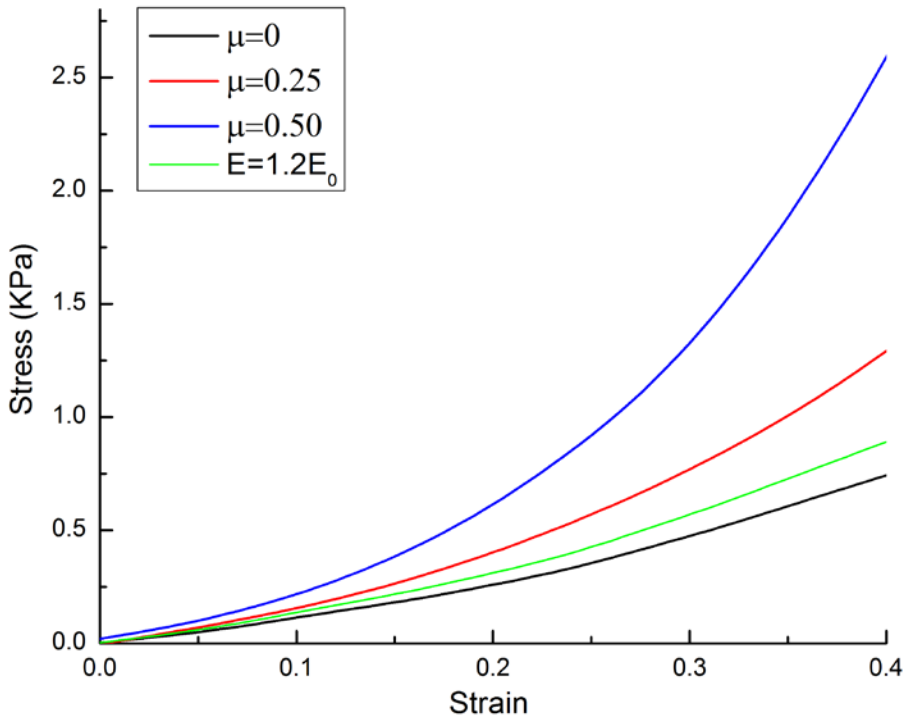

Figure 4.16 Effect of friction and modulus on stress-strain curve

4.6 References

1. Chaudhuri, O., S.H. Parekh, and D.A. Fletcher, *Reversible stress softening of actin networks.* Nature, 2007. **445**(7125): p. 295-298.

2. Liu, A.P., et al., *Membrane-induced bundling of actin filaments.* Nature Physics, 2008. **4**(10): p. 789-793.

3. Correa-Duarte, M.A., et al., *Fabrication and Biocompatibility of Carbon Nanotube-Based 3D Networks as Scaffolds for Cell Seeding and Growth.* Nano Letters, 2004. **4**(11): p. 2233-2236.

4. Lee, S.H., et al., *Highly entangled carbon nanotube scaffolds by self-organized aqueous droplets.* Soft Matter, 2009. **5**(12): p. 2343-2346.

5. Denkov, N., et al., *Mechanism of formation of two-dimensional crystals from latex particles on substrates.* Langmuir, 1992. **8**(12): p. 3183-3190.

6. Fan, J.G., et al., *Nanocarpet Effect: Pattern Formation during the Wetting of Vertically Aligned Nanorod Arrays.* Nano Letters, 2004. **4**(11): p. 2133-2138.

7. Chandra, D., et al., *Biomimetic Ultrathin Whitening by Capillary-Force-Induced Random Clustering of Hydrogel Micropillar Arrays.* ACS Applied Materials & Interfaces, 2009. **1**(8): p. 1698-1704.

8. Bico, J., et al., *Adhesion: Elastocapillary coalescence in wet hair.* Nature, 2004. **432**(7018): p. 690-690.

9. Harris, P.J.F., *Carbon Nanotube Science - Synthesis, Properties, and Applications*. 2009, Cambridge UK: Cambridge University Press.

10. Fan, S.S., et al., *Self-oriented regular arrays of carbon nanotubes and their field emission properties.* Science, 1999. **283**(5401): p. 512-514.

11. Hart, A.J. and A.H. Slocum, *Rapid Growth and Flow-Mediated Nucleation of Millimeter-Scale Aligned Carbon Nanotube Structures from a Thin-Film Catalyst.* The Journal of Physical Chemistry B, 2006. **110**(16): p. 8250-8257.

12. De Volder, M., et al., *Diverse 3D Microarchitectures Made by Capillary Forming of Carbon Nanotubes.* Advanced Materials, 2010. **22**(39): p. 4384-4389.

13. Zhao, Y.P. and J.G. Fan, *Clusters of bundled nanorods in nanocarpet effect.* Applied Physics Letters, 2006. **88**(10): p. 103123-3.

14. Chakrapani, N., et al., *Capillarity-driven assembly of two-dimensional cellular carbon nanotube foams.* Proceedings of the National Academy of Sciences of the United States of America, 2004. **101**(12): p. 4009-4012.

15. Kralchevsky, P.A., et al., *Capillary meniscus interaction between colloidal particles attached to a liquid--fluid interface.* Journal of Colloid and Interface Science, 1992. **151**(1): p. 79-94.

16. Huber, G., et al., *Evidence for capillarity contributions to gecko adhesion from single spatula nanomechanical measurements.* Proceedings of the National Academy of Sciences of the United States of America, 2005. **102**(45): p. 16293-16296.

17. Albert, J.T., et al., *Arthropod touch reception: spider hair sensilla as rapid touch detectors.* Journal of Comparative Physiology a-Sensory Neural and Behavioral Physiology, 2001. **187**(4): p. 303-312.

18. Chandra, D. and S. Yang, *Capillary-Force-Induced Clustering of Micropillar Arrays: Is It Caused by Isolated Capillary Bridges or by the Lateral Capillary Meniscus Interaction Force?* Langmuir, 2009. **25**(18): p. 10430-10434.

19. M. De Volder, S.T., S. Park, D. Copic, Z. Zhao, W. Lu, A.J. Hart, *Directed assembly of complex and robust carbon nanotube architectures by capillary forming.* in Press, 2010.

20. Futaba, D.N., et al., *Shape-engineerable and highly densely packed single-walled carbon nanotubes and their application as super-capacitor electrodes.* Nat Mater, 2006. **5**(12): p. 987-994.

21. Hayamizu, Y., et al., *Integrated three-dimensional microelectromechanical devices from processable carbon nanotube wafers.* Nat Nano, 2008. **3**(5): p. 289-294.

22. Rao, B.N. and G.V. Rao, *On the Large Deflection of Cantilever Beams with End Rotational Load.* ZAMM - Journal of Applied Mathematics and Mechanics, 1986. **66**(10): p. 507-509.

23. Zhang, L., et al., *Influence of a Top Crust of Entangled Nanotubes on the Structure of Vertically Aligned Forests of Single-Walled Carbon Nanotubes.* Chemistry of Materials, 2006. **18**(23): p. 5624-5629.

24. De Volder, M.F.L., et al., *Self-similar organization of arrays of individual carbon nanotubes and carbon nanotube micropillars.* Microelectronic Engineering, 2010. **87**(5-8): p. 1233-1238.

25. Navi, P. and F. Heger, *Combined densification and thermo-hydro-mechanical processing of wood.* Mrs Bulletin, 2004. **29**(5): p. 332-336.

26. Ling, H.I. and H. Liu, *Pressure-Level Dependency and Densification Behavior of Sand Through Generalized Plasticity Model.* Journal of Engineering Mechanics, 2003. **129**(8): p. 851-860.

27. Almeida, R.M. and C.G. Pantano, *STRUCTURAL INVESTIGATION OF SILICA-GEL FILMS BY INFRARED-SPECTROSCOPY.* Journal of Applied Physics, 1990. **68**(8): p. 4225-4232.

28. Hong, W., X. Zhao, and Z. Suo, *Drying-induced bifurcation in a hydrogel-actuated nanostructure.* Journal of Applied Physics, 2008. **104**(8): p. 084905-4.

29. Brydon, A.D., et al., *Simulation of the densification of real open-celled foam microstructures.* Journal of the Mechanics and Physics of Solids, 2005. **53**(12): p. 2638-2660.

30. Sriamornsak, P. and R.A. Kennedy, *A novel gel formation method, microstructure and mechanical properties of calcium polysaccharide gel films.* International Journal of Pharmaceutics, 2006. **323**(1-2): p. 72-80.

31. Sengupta, S.S., et al., *Origins and evolution of stress development in sol-gel derived thin layers and multideposited coatings of lead titanate.* Journal of Applied Physics, 1998. **83**(4): p. 2291-2296.

32. Kozuka, H., *On Ceramic Thin Film Formation from Gels: Evolution of Stress, Cracks and Radiative Striations.* Journal of the Ceramic Society of Japan, 2003. **111**(1297): p. 624-632.

33. Kwon, S.J., J.-H. Park, and J.-G. Park, *Wrinkling of a sol-gel-derived thin film.* Physical Review E, 2005. **71**(1): p. 011604.

34. Kaur, S., et al., *Capillarity-Driven Assembly of Carbon Nanotubes on Substrates into Dense Vertically Aligned Arrays.* Advanced Materials, 2007. **19**(19): p. 2984-2987.

35. Chakrapani, N., et al., *Capillarity-driven assembly of two-dimensional cellular carbon nanotube foams.* Proceedings of the National Academy of Sciences, 2004. **101**(12): p. 4009-4012.

36. Michaël, F.L.D.V., et al., *Fabrication and electrical integration of robust carbon nanotube micropillars by self-directed elastocapillary densification.* Journal of Micromechanics and Microengineering, 2011. **21**(4): p. 045033.

37. Ashby, L.J.G.a.M.F., *Cellular Solids: Structure & Properties (second ed)*, 1997, Cambridge University Press: Cambridge, MA.

38. Bardenhagen, S.G., A.D. Brydon, and J.E. Guilkey, *Insight into the physics of foam densification via numerical simulation.* Journal of the Mechanics and Physics of Solids, 2005. **53**(3): p. 597-617.

39. Sameh, H.T., Z.Z. Zhao et al., *Mechanics of capillary forming of carbon nanotube microstructures.* 2012.

40. Plantema, F.J., *Sandwich Construction: The Bending and Buckling of Sandwich Beams, Plates, and Shells.* 1966.

Chapter 5 Concluding Remarks

This dissertation studied self-assembled surface features in thin films. By understanding the coupling between surface tension, elasticity and other nanoscale forces, I have developed models to simulate the dynamic evolutions and reveal the key mechanisms of the self-assembly processes. Based on the simulation results, critical factors, parameters and mechanisms are elucidated in order to improve the control over defects, order and morphology of assembled structures in existing and potential experiments. The detailed contributions are listed by topics as follows.

5.1 Achievement and contributions

Superlattice:

An approach of sequentially activated self-assembly is shown to grow large-area superlattices from a continuum medium. In this approach, the self-assembly was initiated in a small mobile region to form a seed pattern, and then the mobile region was shifted gradually. The elastic field induced by the seed pattern and its guidance to the growth front are revealed. Also it is demonstrated that the approach has great flexibility and

defect tolerance. Several examples are shown to promote the growth rate of superlattice, which increase the efficiency of the approach.

Further investigation led to another mechanism that self-assembly can propagate spontaneously and deliver ordering information to distance. This mechanism utilizes the ordered pattern in the growth front to trigger self-assembly in the affected zone. Under certain bistable state, the elastic field helps to overcome the energy barrier for self-assembly to propagate. Two propagation scenarios, diffusion-limited and activation-limited propagations, are identified. The approach can produce extremely long-range ordered superlattice without any external guidance.

Templated dewetting:

Recent experiments showed that anodic aluminum oxide (AAO) membranes, which have uniform nanoscale pore size and spacing, can influence the dewetting of iron thin films into organized arrays of nanoparticles. The model adopted captured competition between surface tension and van de Waal interactions in the thin film. The numerical simulations simulated the dynamic dewetting processes from pore expanding, rupture of liquid networks to formation of discrete nanoparticles. It is shown that the AAO pore position variations and the initial film thicknesses have strong influence on the order of nanoparticles, while AAO pore size variations have little effect on the order. The size uniformity of the nanoparticles shows similar degrading tendency as order parameter does.

CNT densification:

Recent experiments showed controllable bent, twisted, re-entrant and other complex 3D microstructures can be fabricated via the elastocapillary densification method. The mechanisms of densification of pre-patterned vertically aligned CNT forests were revealed by understanding the coupling between capillary forces and elasticity in the CNTs. An analytical model was developed to predict the bending angles by considering two competing actions of lateral and axial forces. Time and position dependent loadings were considered in a finite element model to explain the shape change of cross-section of CNT microstructures near the substrate. In addition, a finite element model was developed to capture the nonlinear lateral mechanical behavior of CNT forests, which is confirmed by the experiment.

5.2 Future work

5.2.1 Superlattice: potential systems and experiments

The $1/r^3$ long range elastic interaction considered in this work is similar to many other magnetic[1, 2] or electrostatic dipole interactions[3]. There are representative a range of systems such as Langmuir films, ferromagnetic films, and self-assembled monolayers that should work with these two proposed mechanisms. Detailed simulations and verification can be conducted for different systems. For the spontaneous propagation of self-assembly, the concept may also motivate studies in other physics, bio-systems areas in addition to the material systems we discussed here.

From an experimental point of view, there are several ways to achieve the sequential activation of self-assembly in addition to laser scanning or thermal activation. For instance, one may translate a substrate or nozzle during local deposition, or use other fields such as light or electric field to activate self-assembly at different locations sequentially. In order to achieve the spontaneous propagation of self-assembly in experiment, one needs to first identify the working window of concentration fraction or its equivalency. For example, the bistable state concentration we are interested in this work is from 0.36 to 0.38. We need to either find a preparation technique with this precision or to find a similar system with a wider working window.

5.2.2 Templated dewetting: substrate topology and material parameters

In this dissertation, we considered a pre-templated thin film sitting on a flat solid substrate. However, the real AAO surface may have certain roughness that can trap the

liquid from moving or coarsening. Therefore the future work can consider the effect of substrate topology on the nanoparticle order parameters. For example, the roughness profile can be extracted from AFM images of AAO sample. The model and the initial condition of the film need to be modified to match the rough substrate and position dependent initial film thickness. The additional coarsening barriers due to the surface roughness can be investigated.

The material parameters should be verified for actual material systems. Specially, the surface energy of each interface and the viscosity of the liquid at the operating temperature need to be obtained. Then the Hamaker constant and the equilibrium thickness can be derived from the measured typical wavelength due to spinodal dewetting.

In addition, this work considered a fluid flow model based on lubrication approximation. When the thin film material is below melting point, a diffusion model needs to be considered instead. The governing equation will change from Navier-Stokes equation to diffusion equation.

5.2.3 Densifiction: solidification and buckling models

The cross-shape change of CNT forests during densification can be partially explained as an effect of substrate constraint. However, it cannot explain the situations when high aspect ratio or stand-alone CNT structures are considered. Two preliminary models are proposed to explain the phenomenon.

Solidification model:

Solidification is a phase transition process when liquid transforms into solid as shown in Figure 5.1. In CNT densification process, we may consider the densified CNT structure as a solid phase, while the undensified region as a "liquid phase". Although the undensified region contains solid CNTs, the as-grown CNT forests are highly porous and typically occupy about 1% or less of the total volume.

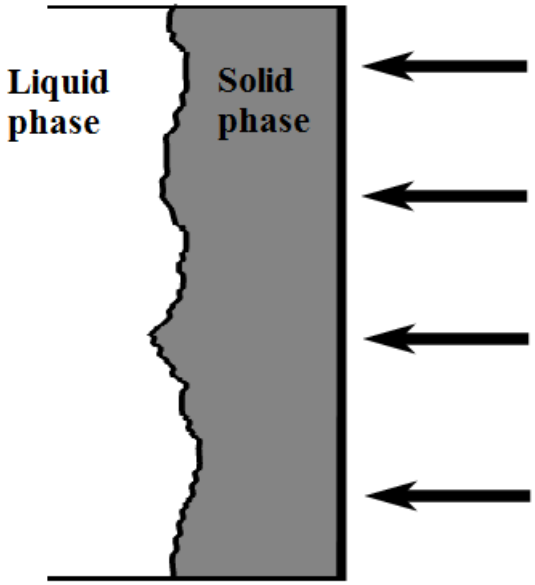

Figure 5.1 Solidification process

Motivated by this idea, we assume that the densification proceeds in the following way.

(1) Begin with a thin layer of solid phase CNTs.

(At this moment the pressure difference between atmosphere and liquid phase is zero, therefore no shape change is observed)

(2) Deposit a thin layer of solid phase CNTs of volume dV.

(This deposition mimics the densification, when the "liquid phase" turns into solid phase. During this process, 0.99dV of liquid is evaporated, left with 0.01dV of solid CNTs.)

(3) Calculate the new pressure inside the liquid phase.

(The pressure inside the current liquid phase decreases due to the evaporation of 0.99dV liquid.)

(4) Based on the new pressure difference (non-zero), the structure deforms.

(5) Repeat (2)-(4) iteratively

(6) The entire process ends when all liquid is evaporated.

In order to implement this process, I utilized the Python scripts of Abaqus instead of the Abaqus/standard graphic user interface to deposit layers of solids and update meshes in each iteration automatically. Additional Fortran subroutines were used to track real-time interfaces and apply time-dependent loadings. Selected simulation results are shown in Figure 5.2. The first four images capture the early stage of "deposition-deformation" processes and the last four images capture the late stage. The current limitation of the method includes material hardening at the corner which in turn stops the sharpening of corner and further densification.

Figure 5.2 Simulation results from solidification finite element model.

Buckling model:

Experiments also showed that CNT forests with circular shaped cross-section deform into “gear” shapes after densification (Figure 5.3 and 5.4).

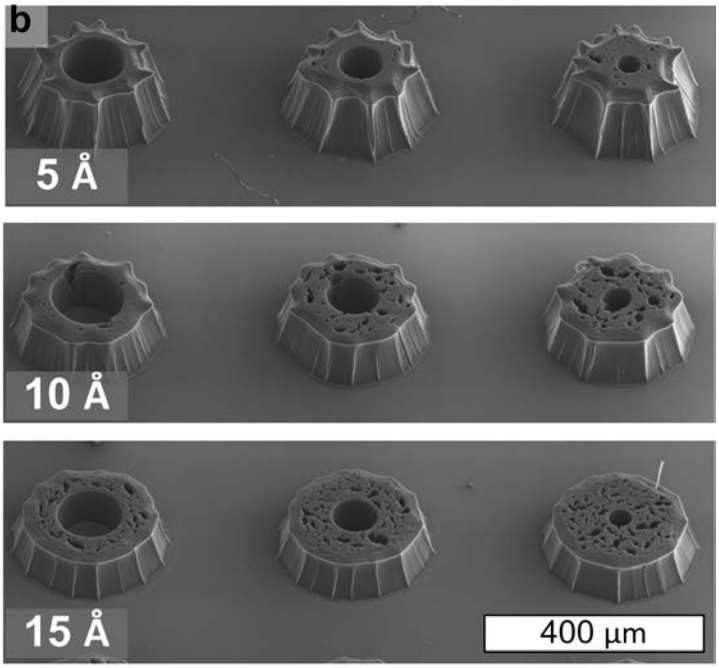

Figure 5.3 Densification of circular shaped cross-section CNT microstructures [4]

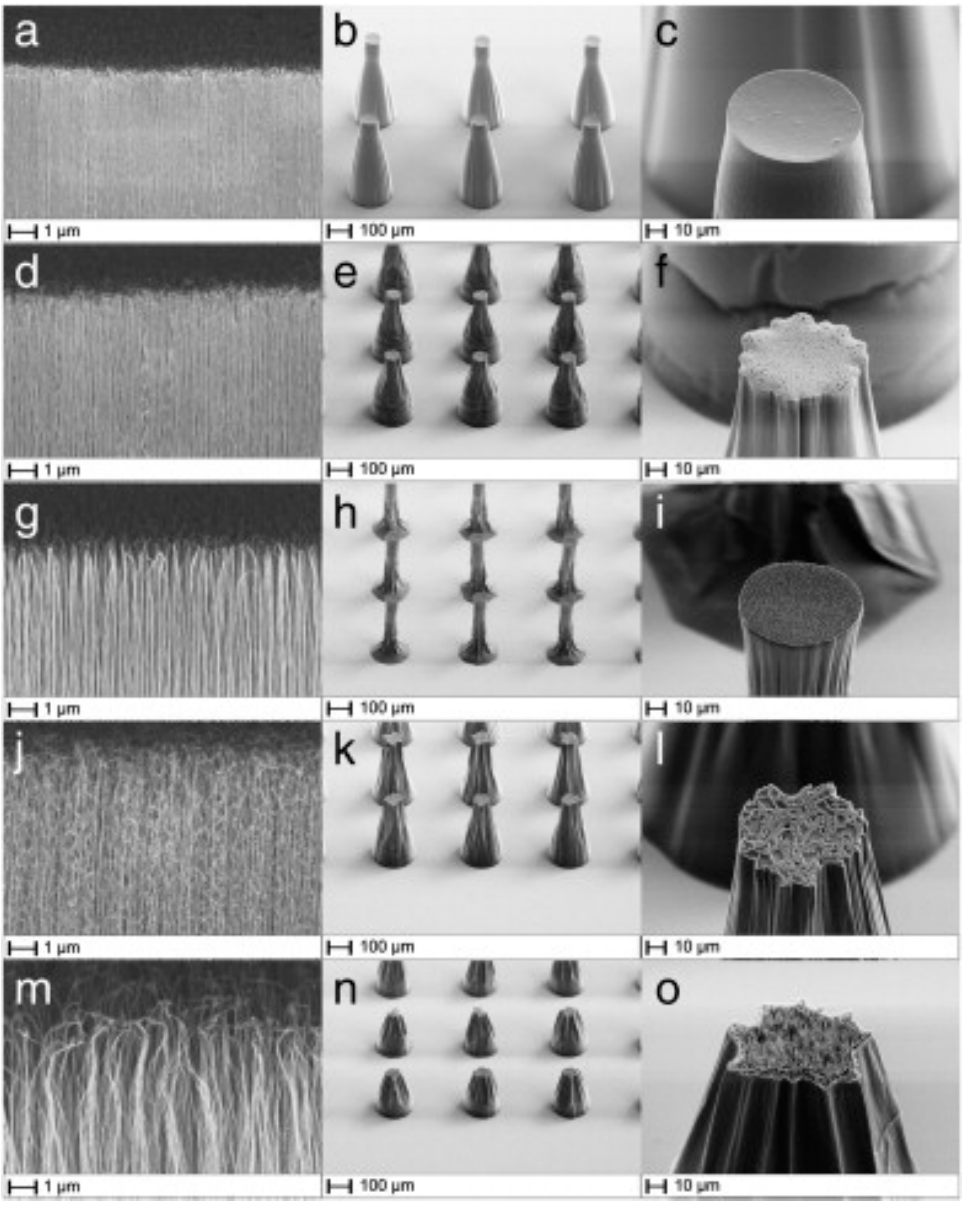

Figure 5.4 Densification results of CNT forests with different volume fractions. (a–c) CNT forests grown at 500 °C. (d–f) CNT forests grown at 600 °C. (g–i) The same as in (d–f), but treated with O_2 plasma. (j – l) CNT forests grown at of 700 °C. (m–o) The same as in (j–l), but treated with O_2 plasma. [5]

It is well known that a thin film will buckle when the underlying substrate shrinks (Figure 5.4). The compression force in the thin film is responsible for the buckling. When the substrate is compliant, the substrate surface will bond to the thin film and follows the buckling pattern. If the substrate is not compliant, the thin film will overcome the adhesion and detach from the substrate.

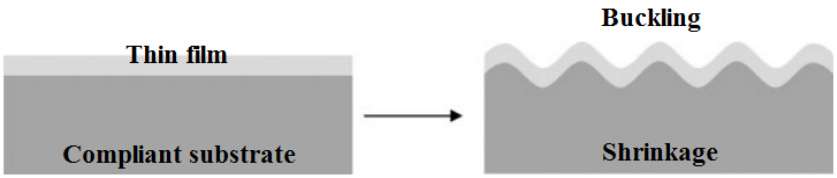

Figure 5.5 Buckling of a thin film due to the shrinkage of a compliant substrate

Motivated by the phenomenon on a flat substrate, we may consider the undensified CNT substrate as a curved compliant substrate, wrapped around by a densified thin film of CNT solid. The densified CNT solid have a much higher elastic modulus than the undensified "substrate". As the densification proceeds, only the undensified CNTs can shrink, which induces compression forces accumulated in the solid thin film layer. The wavelength or number of the wrinkles depends on the thickness and the modulus of the thin film.

Selective preliminary finite element results are shown in the Figure 5.5. In the model, the outer thin film layer is simplified as a beam loop. A negative pressure is applied on the inner surface of the film. Further investigations can to be done in terms of thickness of the solid thin film, modulus of the thin film and the "substrate". A complete study should also include the non-linear lateral stiffness of CNT forests.

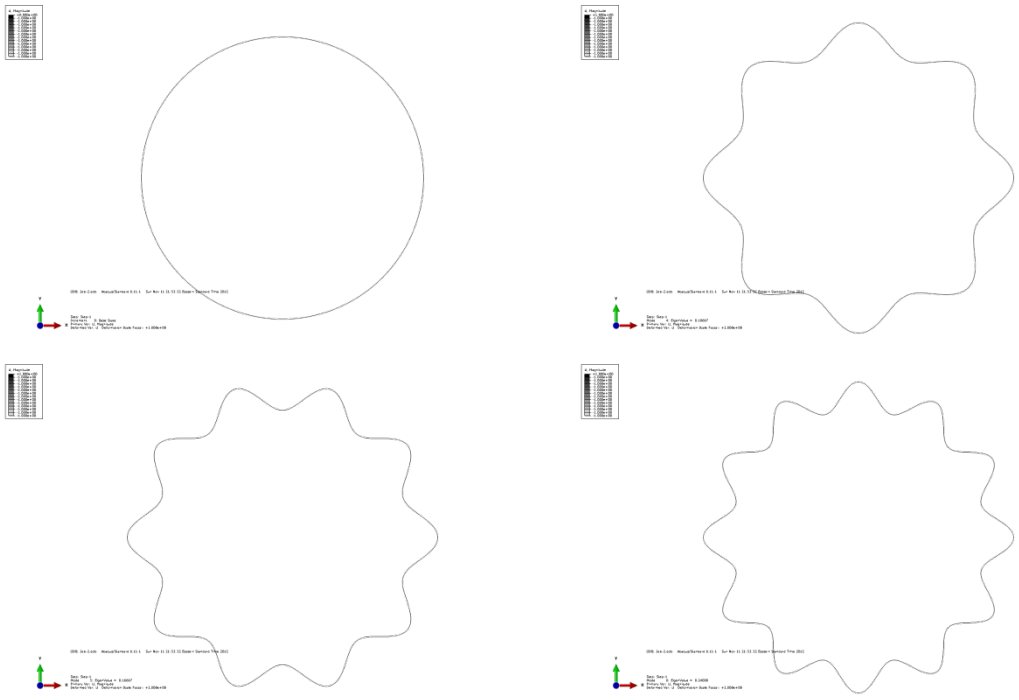

Figure 5.6 Buckling modes for CNT microstructures with circular shaped cross-section.

5.3 References

1. Kim, B.Y., et al., *Magnetic self-assembly of gold nanoparticle chains using dipolar core-shell colloids.* Chemical Communications, 2011. **47**(3): p. 890-892.

2. Chen, J., et al., *Collective Dipolar Interactions in Self-Assembled Magnetic Binary Nanocrystal Superlattice Membranes.* Nano Letters, 2010. **10**(12): p. 5103-5108.

3. Park, J. and W. Lu, *Self-assembly of functionally gradient nanoparticle structures.* Applied Physics Letters, 2008. **93**(24): p. 243109.

4. Sameh, H.T., Z.Z. Zhao et al., *Mechanics of capillary forming of carbon nanotube microstructures.* 2012.

5. Wang, T., et al., *Formation of three-dimensional carbon nanotube structures by controllable vapor densification.* Materials Letters, 2012. **78**(0): p. 184-187.